# A Numerical Investigation of Florida's Sea Breeze-Cumulonimbus Interactions

By
Junn-Luen Song

Department of Atmospheric Science
Colorado State University
Fort Collins, Colorado

Colorado State University

Department of Atmospheric Science

Paper No. 413

# A NUMERICAL INVESTIGATION OF FLORIDA'S SEA BREEZE - CUMULONIMBUS INTERACTIONS

by

Jenn-Luen Song

Research supported by the
National Aeronautics and Space Administration
under Grant NAG5-359
and
the National Science Foundation
under Grant ATM-8414181

Department of Atmospheric Science
Colorado State University
Fort Collins, Colorado

Atmospheric Science Paper No. 413

A NUMERICAL INVESTIGATION OF FLORIDA'S
SEA BREEZE - CUMULONIMBUS INTERACTIONS

Florida's deep cumulus convective effects upon the mesoscale sea breeze environment are investigated using a numerical approach with supportive observational analyses. The mesoscale hydrostatic primitive equation model of Pielke (1974) is coupled with a modified convective parameterization from Fritsch and Chappell (1980), for investigating Florida's deep convective-environmental interactions.

Based on the three-dimensional simulations performed in this study, it is found that the convective-generated downdraft plays a crucial role in modulating the sea breeze environment as well as on subsequent convective developments. Three stages can be identified for the sea breeze-convective interrelationships. Stage 1 (sea breeze convergence stage) is associated with the establishment of coastal sea breeze convergence zones and embedded deep convection which vertically stretches the shallow solenoidal circulation (generated by dry sea breeze) to much deeper depths, thereby further enhancing the sea breeze convergence. Stage 2 (convective downdraft cooling stage) follows the onset of the relatively significant downdraft effects upon the penninsula-scale environment. The downdraft-induced surface cooling generates mesoscale pressure gradient forces near the surface surrounding the convective area. Together with the sea breeze surface flow, low-level convergence is generated on the upwind side which

provides new favorable environments for initiating deep convection. A "four-cell" vertical circulation pattern is formed as a result of the upper tropospheric divergence, mid-tropospheric convergence and the surface divergence due to the downdraft cooling. Finally, Stage 3 (decaying stage) is associated with only mesoscale weaker upward and downward motions without new deep cumulus convective developments.

The model does not simulate properly the effect of Lake Okeechobee due to the use of 22 km as the horizontal grid spacing. On the other hand, the Florida deep convective-environmental interrelationship described above is found to be consistent with the observed behavior of deep convection along the west coast which is adequately resolved using the existing grid.

Jenn-Luen Song
Atmospheric Science Department
Colorado State University
Fort Collins, CO 80523
Fall 1986

ACKNOWLEDGEMENTS

I would like to express my deepest appreciation to Dr. Roger Pielke, my dissertation advisor. Without his continuous encouragement and valuable guidance, this dissertation work could not have been completed. I am grateful to my committee members, Dr. William Cotton and Dr. Richard Johnson for their valuable comments. These comments not only contributed significantly to the text, but also helped me to become enthusiastic about going further on the research.

I extend special thanks to Dr. William Frank and Mr. Charlie Cohen for their kind help regarding the development of a cumulus parameterization which is an important part of my research. I am also grateful to Dr. Greg Tripoli and Mr. Craig Tremback for many helpful discussions and valuable comments on the text. I also thank Dr. Raymond Arritt, Dr. Chaing Chen, Miss Jennifer Cram, Mr. HungChi Kuo, Mr. Jeff McQueen and Mr. Moti Segal for their continuous support.

I would like to thank the technical support from Mrs. Dallas McDonald and Mrs. Sandy Wittler who helped type, organize and edit the manuscript and Judy Sorbie for drafting the figures.

This work has been supported by the National Aeronautics and Space Administration under Grant NAG5-359 and by the National Science Foundation under Grant ATM-8414181. Computations were performed on both the CYBER 205 computer of Colorado State University and on the CRAY-1 computer of the National Center for Atmospheric Research (NCAR) which

is funded by the National Science Foundation. The computer resources on CYBER 205 have been supported by the Institute of Computational Studies and the Department of Computer Science, Colorado State University.

TABLE OF CONTENTS

LIST OF TABLES

LIST OF FIGURES

# Chapter 1

# INTRODUCTION

## 1-1. Background

The summer Florida peninsula has long been recognized as an excellent natural laboratory which provides opportunities for studying mesoscale-convective interactions. One reason for this is that the Florida environment is often associated with undisturbed large scale condition. That is, the convective-environmental interactions over the Florida area is often more detectable than those over, for instance, mid-latitude regions in which large-scale frontal forcing and/or orographic forcing are present. Therefore, the summer Florida convection has long been subject to rather intensive investigations for the purpose of understanding atmospheric scale-interactions in which deep convection is vitally involved. For example, Byers and Braham (1949) made the first thorough observational investigation of the Florida thunderstorm. The major findings of that study have provided valuable insights on the deep convective effects upon the larger scale environment. In particular (in their Chapter 3), they indicated that over the thunderstorm spatial and time scales, the thunderstorm downdraft produces rather significant surface gradients of temperature, pressure, and divergence field. Also, they pointed out that new thunderstorm cell growth has a rather significant tendency to form "clusters" (that is, new cells tend to grow in the adjacent area of existing cells, rather than to grow independently). This tendency of forming clusters,

as suggested by them, is due primarily to the effect associated with downdraft outflow (or, the surface micro-cold front produced by the thunderstorm downdraft).

An important advantage provided by the summer Florida peninsula for investigating convective-environmental interaction is that there is a typically well established mesoscale sea breeze circulation during the undisturbed days. Numerous studies have indicated that the Florida deep convective activities are significantly modulated by the diurnally-varying sea breeze circulation (Pielke, 1974; Atkinson, 1980; among others). For example, Frank, Moore and Fisher (1967) showed that the Florida daytime convection (as obtained by radar analysis) are basically subject to a "forced propagation" driven by the sea breeze convergence, and the latter is a function of the speed and direction of the large-scale prevailing wind. By summarizing their radar analyses, they pointed out that Florida's convection over the southern half of the peninsula (south of Lake Okeechobee) basically propagates together with the sea breeze convergence zone (that is, typically from the windward coast to the lee coast, during the afternoon period), while to the north of the lake the convective pattern is somewhat different and is found to be often the result from a combination of a westerly regime and a light-wind regime. The relationship between radar echo patterns and the prevailing wind was further analyzed by Pielke (1973), in which three categories of echo's development/movement were identified which correspond to southwesterly, southeasterly, and southerly prevailing wind.

During the past decade, more detailed observational analyses have been performed on the Florida convective activities. The predominant

mechanisms, through which Florida convection initiates, enhances and maintains itself, have been revealed/confirmed by these studies. For example, Simpson et al. (1980) stated that one of the most important mechanisms for Florida deep convection to grow is through the surface convergence associated with storm-generated outflow at surface. The new cell growth induced by such surface convergence (or, the "bridging" between two old cells due to the outflow) was regarded by them as storm merging. This merging process has been considered as the fundamental mechanism that the Florida mesoscale convective systems (or clusters) can be formed. Ulanski and Garstang (1978) observed that a mesoscale surface convergence typically precedes a storm development (by an amount of time of about one hour, but could be as large as 90 min). Using a thorough statistical analysis, Lopez et al. (1984a,b) confirmed that the majority of the Florida mesoscale convective systems are the merged systems.

The observed tendency that Florida's convection tends to form clusters also indicates the fact that the existing storm cells provide thermodynamically favorable environment for the new cells to grow. That is, the mid-tropospheric moistening due to both shallow nonprecipitating convection (which produces net moistening) and deep precipitating convection (which produces net moistening and cooling) is found to be important for new cells to grow (Byers and Braham, 1949; Johnson, 1978; Burpee, 1979; Burpee and Lahiff, 1984). Burpee (1979) related the sea breeze convection with the peninsular-scale convergence, while Cooper et al. (1982) considered peninsular-scale and mesoscale convergences, and found that convective downdraft is able to modify the latter such that the subsequent storm development is not totally controlled by the original large-scale forcing.

The Florida deep convective development is also dependent on other physical factors or mechanisms, such as the surface pressure gradient in the immediate storm environment (Cunning and DeMaria, 1986); surface response due to anvil cover (Pielke and Cotton, 1977); surface properties (Gannon, 1978); etc.

Recently, Van De Berg and Oerlemans (1985) simulated the dependence of sea breeze front propagation upon non-precipitating cloud formation, using a non-hydrostatic 2-D model. They hypothesized that the coupling of the convective heating over land and the evaporative cooling over sea produces an additional horizontal thermal gradient, thereby enhancing the intensity and inland propagation of the sea breeze front. In a similar sea breeze front simulation performed by Gross (1985), however, the above described cloud effect was not found. Rather, cloud formation appeared to affect only the intensity of sea breeze circulation and not the sea breeze front propagation. Briere (1986) studied the 2-D energetics of dry sea breeze circulations using a third-order turbulence closure model. This study differs from the previous sea breeze energetic studies of Dalu and Green (1980), Green and Dalu (1980), and Richiardone and Pearson (1983), in that it incorporates the interactions between sea breeze and boundary layer turbulence. He concluded that the sea breeze circulation is very sensitive to turbulence and that the turbulence intensity depends essentially on the boundary layer dry convection and its interaction with the mean shear.

In summary, the deep convective activities over the summer Florida, during large-scale undisturbed days, have been studied rather intensively during the last decade. The deep convective activities

appear to be closely related to both the sea breeze circulation and the convective-generated downdraft. The majority of the organized convection is found to be produced by the merging process, which is associated with the diurnally-varying sea breeze convergence zone and the locally enhanced downdraft effect on surface.

1-2. Motivation of the Study

Although the aforementioned investigations on Florida convection have revealed some of the most important mechanisms concerning the deep convective development, a four-dimensional illustration of Florida's mesoscale-convective interaction has actually never been documented thus far in the literature.

Pielke (1974) and Pielke and Mahrer (1978) have performed successful three-dimensional simulations of the Florida sea breeze circulation. They showed that the model predicted sea breeze convergence zones match well with the radar observed shower activity areas (in both location and timing). However, a "dry" model (that is, no latent heating included) was used in those simulations, and therefore no convective feedback effects were discussed. On the smaller scales, Tripoli and Cotton (1980) and Tao and Simpson (1984) have simulated the Florida thunderstorm and the merging process, respectively, on the storm scales (that is, horizontal scales of about 30 km x 30 km, and time scales on the order of one hour).

The fact that the Florida deep convection is strongly modulated by the dirunally-varying sea breeze circulation has imposed a difficulty on numerically simulating the deep convection, especially when the latter is viewed on the mesoscale. That is, it seems that a meaningful simulation of the Florida sea breeze-convective interaction must at

least cover spatial scales of about 300 km x 300 km and time scale about 10 hours. Such domain sizes are currently impossible to be considered for the explicit convective simulations (such as that performed by Tripoli and Cotton, 1980).

To circumvent the difficulty associated with computational resource limitations, it is felt in this study that a cumulus parameterization approach must be utilized. That is, it is felt that the aforementioned observational analyses have provided the necessary background for a numerical simulation on the sea breeze-convective interactions, using a numerical technique which includes both a successful sea breeze model and a newly derived cumulus parameterization (which is particularly designed for this study).

1-3. Objective of the Study

Summarizing the Florida sea breeze and convective observational analyses, the present study is intended to be based on the following hypothesis: the lower-tropospheric storm-generated downdraft substantially modifies the associated mesoscale environment generated by sea breeze circulation, thereby producing the necessary forcing which organizes the deep convection on the mesoscale environment.

Specifically, answers to the following questions will be sought:

(1) Under the synoptically undisturbed condition, how does Florida sea breeze circulation interact with the embedded deep convection during the lifetime of the convective system?

(2) What are the major deep convective effects upon the peninsular-scale dry sea breeze circulation?

(3) How does the sea breeze-convective interrelationship depend on the environmental condition (such as strong vs. weak prevailing wind; moist vs. dry troposphere; etc.)?

(4) With the deep convective effects incorporated, how is the mesoscale kinetic energy balance achieved, and different from that without the convection?

1-4. Approach

The main interest of the present study is, through using numerical simulations coupled with available observations, to understand the three-dimensional interactions between the Florida sea breeze circulation and the embedded deep convection, over a time period of about the lifetime of the convective system.

The aforementioned three-dimensional sea breeze model (Pielke, 1974; Pielke and Mahrer, 1978) will be utilized to provide the necessary sea breeze forcing for the deep convection to develop. More detailed introduction of this model will be included in Chapter 2, together with a kinetic energy budget equation which is derived for investigating the sea breeze kinetic energy balances with and without the deep convection.

Deep convective feedback effects upon the sea breeze mesoscale environment will be simulated using a modified version of the Fritsch-Chappell parameterization (Fritsch and Chappell, 1980). Since a cumulus parameterization used for the Florida mesoscale convective systems has never been documented before, the derivation of the parameterization modifications, at least partially, must necessarily be new. Nevertheless, as will be illustrated in detail in Chapter 3, the parameterization is derived based on simultaneously three sources of

information: available observation (such as that documented in Pielke and Cotton, 1977); previous parameterization logic (such as that documented in Fritsch and Chappell, 1980, and Frank and Cohen, 1984); and some diagnostic information from a cloud-scale explicit simulation (similar to that of Tripoli and Cotton, 1980). Also, the parameterization will be evaluated as to its conservation properties as well as sensitivities due to several inherent assumptions.

Chapter 4 will include the main simulation results and discussions (the "control run") on the mesoscale sea breeze-convective interactions. Deep convective effects upon the peninsular-scale surface and upper-level environments will be illustrated. In Chapter 5, several similar three-dimensional simulations will be illustrated concerning the sensitivities of the simulation due to various physical forcing. Different stages of the sea breeze-deep convective interactions during the lifetime of the convective system will be illustrated separately using conceptual models and will be discussed in Chapter 6. Finally, the summary and conclusion of this study are included in Chapter 7.

# Chapter 2

# MODEL EQUATIONS

In this chapter, the prognostic mesoscale model (into which the deep convective effects will be incorporated) will be briefly described. The computations of the model contains two main parts, being associated with atmospheric mesoscale dynamics and thermodynamics without latent heating; and subgrid-scale deep moist convection. The former part is largely following Pielke (1974), Mahrer and Pielke (1975, 1977, 1978), Pielke and Mahrer (1975, 1978) with only minor modifications. The latter part concerns parameterization for deep convective effects, which will be introduced and discussed in Chapter 3 and Chapter 4, and will not be included here.

In Section 1, model structure (including governing equations, dry PBL formulation, numerical schemes, and boundary conditions) will be briefly illustrated. Following this, the diagnostic kinetic energy budget equation (which includes a term representing convective effects obtained through the parameterization) will be introduced in Section 2.

## 2-1. Model Structure

As discussed in Chapter 1, under synoptically undisturbed conditions, the sea breeze circulation provides the primary environmental forcing and energy supply for the development of Florida deep moist convection. Thus, for the purpose of modeling Florida sea breeze-convective interactions, the sea breeze evolution must be satisfactorily simulated. The model used is a modified version of the

three-dimensional hydrostatic primitive equation model originally developed by Pielke (1974) in order to study the sea breezes over south Florida. Improvements made to this model since then have been described in Mahrer and Pielke (1975, 1977, 1978), Pielke and Mahrer (1978), among others.

The studies mentioned above had been focused primarily on the dry sea breeze circulation (i.e., sea breeze without moist convective effects). Thus, the model vertical domain extended to only about 5-6 km. Accordingly, the incompressible continuity equation had been used. In those studies, since the PBL diabatic processes was of the main concern, relatively high vertical resolution was used in the lowest 1 kilometer or so.

In the current study, deep convective effects are of the primary concern. Yet, the energy supply provided by the sea breeze are also required. Therefore, a larger vertical domain (up to 20 km) is used, while still maintaining relatively high resolution near surface. The 16 vertical levels are at: 9., 91., 390., 847., 1325., 1827., 2640., 3824., 5173., 6749., 8654., 10336., 11704., 13329., 15421., 20728.(m). Thermodynamic variables are staggered in the vertical with respect to the above heights. The effect of density variations in the vertical are incorporated into the calculation of vertical velocity. The grid resolution used in the mesoscale prognostic model (in which deep convection is parameterized) is 22 km. This grid resolution differs from that used by Pielke (1974) and Pielke and Mahrer (1978) for simulating dry sea breeze circulation (11 km was used in those studies). The use of the 22 km-grid is required in order that deep convective effects be considered as "subgrid-scale" processes, thereby requiring a

"parameterization" to simulate the effects. Using 22 km, the relative contribution from subgrid-scale processes can be more realistically isolated from the total quantities, as compared with using 11 km. In the following, the governing equations will be illustrated:

2-1-a. Governing Equations

- Horizontal momentum equations

$$\frac{\partial u}{\partial t} = -u\frac{\partial u}{\partial x} - v\frac{\partial u}{\partial y} - w\frac{\partial u}{\partial z} + fv - fV_g - \hat{f}w - \theta\frac{\partial \pi}{\partial x} + \frac{\partial}{\partial z}\left(K_z^m \frac{\partial u}{\partial z}\right) + \left.\frac{\delta u}{\delta t}\right|_{CU} + H^u \tag{1}$$

$$\frac{\partial v}{\partial t} = -u\frac{\partial v}{\partial x} - v\frac{\partial v}{\partial y} - w\frac{\partial v}{\partial z} - fu + fU_g - \theta\frac{\partial \pi}{\partial y} + \frac{\partial}{\partial z}\left(K_z^m \frac{\partial v}{\partial z}\right) + \left.\frac{\delta v}{\delta t}\right|_{CU} + H^v \tag{2}$$

where

| | | |
|---|---|---|
| $u,v,w$ | : | velocity components in x, y, z directions |
| $f,\hat{f}$ | : | coriolis parameters |
| $U_g,V_g$ | : | east-west and north-south geostrophic wind. |
| $K_z^m$ | : | vertical exchange coefficient of momentum. |
| $\left.\frac{\delta u}{\delta t}\right\|_{CU}, \left.\frac{\delta v}{\delta t}\right\|_{CU}$ | : | deep convective feedbacks. |
| $H^u,H^v$ | : | the horizontal filter effect. |

- Thermodynamic Energy Equation

$$\frac{\partial \theta}{\partial t} = -u\frac{\partial \theta}{\partial x} - v\frac{\partial \theta}{\partial y} - w\frac{\partial \theta}{\partial z} + \frac{\partial}{\partial z}\left(K_z^\theta \frac{\partial \theta}{\partial z}\right) + \left.\frac{\delta \theta}{\delta t}\right|_{CU} + H^\theta \tag{3}$$

where

| | | |
|---|---|---|
| $\theta$ | : | potential temperature. |
| $K_z^\theta$ | : | vertical exchange coefficient of heat. |

$\left.\frac{\delta\theta}{\delta t}\right|_{CU}$ : deep convective feedbacks.

$H^{\theta}$ : the horizontal filter effect.

- Moisture Conservation Equation

$$\frac{\partial q}{\partial t} = -u\frac{\partial q}{\partial x} - v\frac{\partial q}{\partial y} - w\frac{\partial q}{\partial z} + \frac{\partial}{\partial z}\left(K_z^q \frac{\partial q}{\partial z}\right) + \left.\frac{\delta q}{\delta t}\right|_{CU} + H^q \qquad (4)$$

where $q$ : specific humidity of water vapor

$K_z^q$ : vertical exchange coefficient of water vapor

$\left.\frac{\delta q}{\delta t}\right|_{CU}$ : deep convective feedbacks

$H^q$ : the horizontal filter effect.

- Deep Continuity equation

$$\nabla_3 \cdot \rho_o \vec{V} = 0 \qquad (5a)$$

The density term is assumed to be a function of height only, thus the continuity equation is also written as:

$$\nabla \cdot V + \frac{1}{\rho_o}\frac{\partial}{\partial z}(\rho_o w) = 0 \qquad (5b)$$

where $\nabla_3$, $\nabla$ : 3-D and 2-D del operators

$\vec{V}$, $V$ : 3-D and 2-D velocity vectors

$\rho_o$ : density, $\rho_o = \rho_o(z)$.

Vertical velocity is calculated by applying Eq. (5b) to the finite difference vertical grids in the model. From equation (5b), the vertical massflux is:

$$\rho_o w = -\int \rho_o(\nabla \cdot V)\, dz \; . \qquad (6a)$$

Therefore, vertical velocity at each level is calculated as:

$$w_j = \frac{\rho_{o_{j-1}}}{\rho_{oj}} w_{j-1} + \frac{\hat{\rho}_{oj}}{\rho_{oj}} (-\nabla \cdot v)_j \cdot \Delta z_j \qquad (6b)$$

where "j" is the index of the model vertical levels. Other parameters and variables defined as:

$$\Delta z_j = z_j - z_{j-1}$$

$$\hat{\rho}_{oj} = \tfrac{1}{2}(\rho_{oj} + \rho_{oj-1});$$

$\rho_o$ is diagnosed from: $\rho_o = \frac{P_{oo}}{R} \left( \frac{\pi_o}{C_p} \right)^{\frac{C_p}{R}-1} \cdot \frac{1}{\theta_o}$ (6c)

$P_{oo}$ : reference pressure

$\pi_o, \theta_o$ : the environmental scaled-pressure (to be defined below) and potential temperature, $\pi_o = \pi_o(z)$, $\theta_o = \theta_o(z)$.

$R$ : gas constant for dry air

$C_p$ : specific heat a constant pressure

Vertical velocity is identically zero at the surface. At the model top, a material surface is used which conserves the total mass of the model while allowing vertical motion to exist.

o Model Top Height Equation

$$\Delta S = \left(W_{top} - u \frac{\partial S}{\partial x} - v \frac{\partial S}{\partial y}\right) \Delta t \qquad (7)$$

where $\Delta S$ : height change of the material surface

$W_{top}$ : vertical velotiсy on the original Eulerian model top

$S$ : height of the material surface

- Diagnostic Hydrostatic Pressure Equation

$$\pi^{\tau}_{top} = \pi^{\tau-1}_{top} - \Delta S \frac{g}{\theta_{top}} \tag{8a}$$

$$\pi_j = \pi_{j+1} + g \cdot \int_j^{j+1} \frac{1}{\theta} \, dz \tag{8b}$$

where $\pi_{top}, \theta_{top}$ : scaled-pressure (defined below) and potential temperature at the top (i.e., the material surface)

$\tau, \tau-1$ : index of model time step

$g$ : acceleration of gravity

$$\pi \equiv C_p \left( \frac{P}{P_{oo}} \right)^{R/C_p} \tag{9}$$

$P$ : pressure

2-1-b. Dry PBL Diabatic Processes

The dry surface layer fluxes of heat, moisture and momentum are based on the work of Businger (1973), while the dry turbulent mixing in the remainder of the planetary boundary layer was parameterized for an unstable surface layer using an exchange coefficient formulation as described by O'Brien (1970). The depth of the dry planetary boundary layer for this case of upward heat flux is predicted utilizing a formulation introduced by Deardorff (1974). When deep convection is produced, the PBL height calculated from this formulation is modified (this modification will be illustrated in Chapter 3 when the cumulus convective parameterization is discussed).

The changes of air temperature due to short- and long-wave radiative fluxes are parameterized following the methods of Atwater and Brown (1974). Heating of the atmosphere by short-wave radiation is confined to water vapor, while carbon dioxide and water vapor are

considered in the long-wave radiation heating/cooling algorithm. When deep convection is generated, long-wave radiation is modified due to the net moistening of convection, while short-wave radiation, following Zhang (1985), is reduced to half (for the developing stage) and completely shut off (for the mature stage of a deep convection).

The temperature at the ground surface is calculated using an energy budget where the long- and short-wave radiation, the soil heat flux and the turbulent mixing of sensible and latent heat are used to calculate the equilibrium surface temperature. The downdraft effect is implicitly included through the radiation and the turbulent fluxes terms. The temperature at the water-air interface is prescribed and assumed invariant in the calculation.

The detailed computational steps of evaluating the eddy exchange coefficients and surface balanced temperature are included in Appendix A, and are discussed in the above referenced studies.

2-1-c. Numerical Schemes

The advective terms are evaluated by upstream interpolation with a cubic spline technique (Purnell, 1976; Mahrer and Pielke, 1978; Pielke, 1984). The vertical diffusion terms are evaluated by the Crank-Nicholson implicit method (Paegle et al., 1976) with a relatively larger weighting for the "future" step coefficient as opposed to the "current" step. The details of this implicit vertical diffusion calculation, as used in the model, can be found in Song et al. (1985).

The horizontal diffusion is represented by a selective low-pass filter developed by Pepper et al. (1979). The filter effectively removes $2\Delta x$ wave for any positive values of the coefficient (see Pielke, 1984 for a more detailed description of the filter). Waves

longer than $4\Delta x$ are essentially unchanged. In this study, a constant coefficient of 0.02 is used except in the absorbing layer (described in Subsection 2-1-d) of the model in the lower stratosphere when the deep convection is permitted.

2-1-d. Boundary Condition

At the lateral boundaries, a zero-gradient condition (Pielke and Mahrer, 1978) is used. When deep convective effects are incorporated, two extra procedures are applied in order to assure no wave reflection from the boundaries and no distortion of the desired model results. The first is to extend the horizontal domain to be sufficiently large, such that the atmospheric processes of interest are far removed from the lateral boundaries (Pielke, 1984). For this purpose, the domain is extended with extra grid points (pure water) on the sides. Since there was primarily southeasterly wind in the lower troposphere, and northeasterly wind in the upper troposphere for the case study discussed in Chapter 4, there are 7 grid points added to the west and north, and 1-3 grid points added to the east and south of the horizontal domain. In Chapter 4, the surface land-water distribution and the Florida coast line are illustrated.

Another procedure concerns the model top boundary condition when deep convective effects are incorporated. A sponge-type upper boundary condition is applied. The horizontal filter described above is assigned with gradually increasing coefficients for the top five levels (0.025, 0.03, 0.04, 0.06, 0.07). This extra filtering is applied only when deep convection occurs somewhere within the model domain, and only on potential temperature. Physically, this extra filtering is applied in the lower stratosphere (between about 11 km and 20 km), where

typically deep clouds expand horizontally to larger areas (anvil cloud). Therefore, the cloud-scale pressure gradients produced by convective heating are not expected to be significant in this lower stratospheric layer.

## 2-2. Kinetic Energy Budget Equation

Following Ward and Smith (1976), Vincent and Schlatter (1979), Fuelberg and Jedlovec (1982) and Pielke (1984), the KEB equation is derived in this section. Because of the hydrostatic framework of the model, the time tendency of the domain kinetic energy variation includes only the contributions of horizontal velocity components. This is because vertical velocity is not obtained prognostically in a hydrostatic model. However, when the "subgrid-scale" convective effect is significant, even in a hydrostatic framework on the resolvable-scale, there should be "parameterized" convective effects in the kinetic energy budget equation. Because such an equation in this study is only a diagnostic tool for studying the sea breeze kinetic energy budget, including a parameterized convective term does not affect the dynamic simulation, but only provides a comparison between the convective term and other budget components which are obtained from the hydrostatic model. The calculation of the convective term, however, requires the parameterization formulation, and therefore is included in Chapter 3. In the following kinetic energy budget equations the convective term is only indicated symbolically. The kinetic energy balances for the dry and moist sea breeze simulations will be briefly illustrated in Chapter 6.

2-2-a. Grid-Point Kinetic Energy Equaton

Equation (1) is multiplied by $(\rho_o u)$ and Eq. (2) by $(\rho_o v)$, and the results added. After applying the continuity equation, (5a), we obtain the prognostic equation for the model grid-point kinetic energy (KE) as follows:

$$\frac{\partial \rho_o k}{\partial t} = -\frac{\partial}{\partial x}(\rho_o uk) - \frac{\partial}{\partial y}(\rho_o vk) - \frac{\partial}{\partial z}(\rho_o wk) + \rho_o(-ufV_g - vfU_g)$$

(a) (b) (c1)

$$+ \rho_o\left(-\theta u \frac{\partial \pi}{\partial x} - \theta v \frac{\partial \pi}{\partial y}\right) + TUR + CON \quad . \tag{10}$$

(c2) (d) (e)

The left-hand-side is the time tendency of the grid-point horizontal KE, where $k = \frac{1}{2}(u^2+v^2)$. The right-hand-side includes the following terms:

- Horizontal Flux Convergence = Term (a)
- Vertical Flux Convergence = Term (b)
- Cross-Contour Term = Term (c1) and (c2)

In the model, the pressure gradient term is divided into two parts: a background pressure gradient (associated with the geostrophic wind, which is set to a constant in time); and the mesoscale perturbation pressure gradient (associated with the pressure resulting from heating of the land by the sun and convective heating). In the sea breeze simulations, term (c2) is always about an order of magnitude larger than term (c1).

- Turbulence term = Term (d)

  This term is explicitly written as: $\rho_o u \frac{\partial}{\partial z}(K_z^m \frac{\partial u}{\partial z})$

  $+ \rho_o v \frac{\partial}{\partial z} (K_z^m \frac{\partial v}{\partial z})$.

It represents the friction effect upon the model kinetic energy. Since the eddy exchange coefficients of momentum essentially become negligible above PBL in the absence of deep cumulus convection, the turbulence term in the model's KEB is significant only within PBL.

- Convective contribution term = Term (e)

  This term represents the "direct" effect due to the subgrid-scale convection upon the resolvable-scale kinetic energy balance. It is derived in Chapter 3, and briefly discussed in Chapter 6 together with other KEB components.

As in Fuelberg and Jedlovec (1982), vertical profiles of the horizontally averaged KEB components will also be discussed in Chapter 6.

2-2-b. Domain-Integrated Kinetic Energy Budget Equation

The domain-integrated KEB is obtained by integrating equation (10) over the three-dimensional domain. Since vertical mass fluxes are identically zero at the bottom and top boundaries, the vertical flux convergence term is integrated to zero. The integrated KEB equation is formally written as:

$$\frac{\partial K}{\partial t} = \frac{1}{L_y L_z} \int_y \int_z ((\rho_o uk)_W - (\rho_o uk)_E) dydz$$

$$+ \frac{1}{L_x L_z} \int_x \int_z ((\rho_o vk)_S - (\rho_o vk)_N) dxdz$$

$$+ \frac{1}{L_x L_y} \int_x \int_y \int_z \rho_o (-ufVg - vfUg - \theta u \frac{\partial \pi}{\partial x} - \theta v \frac{\partial \pi}{\partial y}) \, dxdydz$$

$$+ \frac{1}{L_x L_y} \int_x \int_y \int_z (TUR)\, dxdydz$$

$$+ \frac{1}{L_x L_y} \int_x \int_y \int_z (CON)\, dxdydz$$

$$+ \frac{1}{L_x L_y} \int_x \int_y \rho_o k \frac{\Delta S}{\Delta t}\, dxdy \qquad (11)$$

where $$K = \frac{1}{L_x L_y} \int_x \int_y \int_z (\rho_o k)\, dxdydz \qquad (12)$$

$L_x, L_y, L_z$ = length of domain in the direction specified by the subscript

subscripts (W,E,S,N) = the west, east, south, north boundaries

The last term in equation (11) arises from Leibnitz's rule since the material surface is a function of time, and all the vertical integrations refer to the material surface. Generally, this term is always more than three orders of magnitude smaller than the other terms (Fuelberg and Jedlovec, 1982; among others), and therefore is neglected in the KEB analysis of this study. Following Anthes and Warner (1978), the model domain-integrated kinetic energy tendency obtained from the budget equation is compared with that obtained directly from the model momentum quantities in Appendix C, for the three-dimensional moist sea breeze simulation (introduced in Chapter 4).

# Chapter 3

# PARAMETERIZING FLORIDA'S DEEP CONVECTION

## Introduction

In this chapter, a modified version of the Fritsch-Chappell cumulus parameterization (Fritsch and Chappell, 1980; hereafter referred to as FC scheme) will be introduced, which will then be used for the investigation of the Florida sea breeze-convective interactions (when coupled with the model introduced in Chapter 2). Details concerning the design and application of the FC scheme can be found in Fritsch and Chappell (1980), Frank (1983) and Zhang (1985), and will not be included in this study. The main feature of the modified FC scheme to be used in the current study is discussed in Section 3-2. The scheme is then tested regarding its conservation properties (Section 3-3) as well as its sensitivities (Section 3-4). Modifications upon the dry PBL formulation are included in Section 3-5. The convective direct contribution term upon a hydrostatic kinetic energy budget is illustrated in Section 3-6.

The FC scheme is chosen as the framework (upon which modifications will be made) for the following reasons:

(1) It differs from the conventional one-dimensional schemes (such as Kuo, 1974; Anthes, 1977) in that it includes convective downdrafts along with the convective updraft processes.

(2) It develops deep convection by considering, in addition to the instantaneous grid-scale forcing, a convective self-generated enhancing mechanism (see more detailed discussions in Fritsch, 1975; Maddox, 1980; Fritsch and Maddox, 1981).

(3) It is most applicable to mesoscale modeling in which updraft, downdraft, and the cloud-free grid-environment each occupy non-negligible fractions of a grid area. Therefore, it can include the parameterization of several convective induced processes (such as surface outflow, subsidence, etc.) which the one-dimensional scheme generally can not.

(4) It is economical while still representing many of the important convective processes.

For the particular investigation performed in the present study, however, the FC scheme is found to be unsuitable with respect to its formulation for calculating the convective intensity. The more significant changes made to the FC scheme concern the following assumptions of that scheme:

(1) The FC scheme assumes that the resolvable-scale condition within a grid element remains unchanged for a time period of about 30 min to 1 hour (during which convective feedback effects are incorporated into the resolvable-scale field). Although the instantaneous effect of using such an assumption may not be significant, it is found that the cumulative effect could significantly distort the simulation results (this problem is discussed later in this chapter).

(2) The intensity of convection in the FC scheme is essentially determined by the specified "convective effective time" of

30 min to 1 hour (that is, convection must be such that it completely stabilizes the grid within the specified time period). For those convective systems having lifetime of more than one hour, without being displaced significantly, such an assumption may overestimate the convective effect during its earlier stage.

(3) The vertical distribution of the resulted convective heating is such that the heating maximum is nearly always around cloud top height (due to an assumed updraft mass flux which increases monotonically from cloud base to cloud top).

In the next section, the convective parameterization to be used for the present study (hereafter referred to as the current scheme, which is used for the Florida simulations) will be described. Special attention will be paid to the modifications made on the FC scheme, and to the physical background regarding why the modifications are necessary. The other parts of FC scheme's formulation are largely retained, and therefore will not be discussed in this chapter (the step-by-step formulation used in the current scheme are included in Appendix B).

## 3-2 Convective Parameterization

As indicated in Frank (1983), the cumulus parameterization problem includes parameterizing the subgrid-scale convective processes as well as simulating the intercommunications between the parameterized cloud and its resolvable-scale environment (that is, in terms of the two-way exchanging rates of energy and/or momentum between the resolvable and the subgrid-scale fields).

The task of a convective parameterization can be separated into two parts: (A) the calculation of convective intensity; and (B) the updating of the resolvable-scale field due to the convection. Part (A) includes evaluating the level-by-level thermodynamic properties of the updraft, downdraft and grid-environment; while Part (B) determines how the diagnosed convective effect is incorporated into the associated prognostic model. Formulations of Part (A) for the current scheme, as included in Appendix B, basically follows the same general approach as other techniques and therefore will not be discussed in detail. Part (B) of the current scheme, on the other hand, is considered distinct from the aforementioned schemes, and therefore will be discussed in detail.

3-2-a. Frequency of Updating the Resolvable-Scale

As mentioned above, the most important difference between the current scheme and FC scheme concerns the intercommunication formulation between the parameterized convection and the resolvable-scale dynamics and thermodynamics.

Instead of requiring the convective environmental condition to be unchanged for a time period of 30 min-1 hour (as in FC scheme), the current scheme requires that the resolvable-scale dynamic and thermodynamic conditions be updated in response to the convective effect at a higher frequency. The time period is chosen to be the typical amount of time for a convective downdraft (which typically is initiated around the mid-troposphere) to reach the surface. A time of 20 min is used for this purpose, which is consistent with observations (such as Byers and Braham, 1949, for Florida's thunderstorm). Thus, the parameterized convection will interact with its mesoscale environment every 20 min

Table 3-2. Parameterization results without the adjustments.

| Z (cm) | $\frac{\delta T}{\delta t}$ ($\frac{°C}{20\ min}$) | $\frac{\delta T}{\delta t}$ ($\frac{°C}{day}$) | $\frac{\delta q}{\delta t}$ ($\frac{g/g}{s}$) | $\frac{\delta q}{\delta t}$ ($\frac{g/kg}{20\ min}$) | $\theta_{new}$ | $\theta_{old}$ | $q_{new}$ | $q_{old}$ |
|---|---|---|---|---|---|---|---|---|
| 2072839.0 | -.00 | -.00 | -.0000000 | -.0000000 | 476.00 | 476.00 | .0000100 | .0000100 |
| 1662468.0 | -.22 | -16.00 | .0000000 | .0000001 | 367.06 | 367.28 | .0000100 | .0000100 |
| 1421823.0 | -.53 | -38.07 | .0001360 | .0067996 | 337.79 | 338.32 | .0001461 | .0000101 |
| 1243921.0 | .10 | 7.21 | .0000020 | .0000996 | 335.41 | 335.31 | .0000120 | .0000100 |
| 1096781.0 | 1.14 | 82.26 | .0000956 | .0047802 | 333.23 | 332.08 | .0001114 | .0000158 |
| 970418.0 | 1.64 | 118.42 | -.0000510 | -.0024584 | 330.70 | 329.06 | .0002987 | .0003497 |
| 760291.0 | .74 | 53.01 | -.0000649 | -.0032467 | 323.76 | 323.02 | .0014321 | .0014970 |
| 589461.0 | .82 | 59.01 | -.0001570 | -.0078493 | 316.34 | 315.52 | .0034210 | .0035780 |
| 589461.0 | .82 | 59.01 | -.0001570 | -.0078493 | 316.34 | 315.42 | .0034210 | .0035780 |
| 445078.0 | .42 | 30.17 | .0009492 | .0474582 | 310.36 | 309.94 | .0044862 | .0035370 |
| 319663.0 | .17 | 12.33 | .0004383 | .0219167 | 305.38 | 305.20 | .0076903 | .0072520 |
| 208384.0 | -.00 | -.33 | .0014895 | .0744775 | 303.80 | 303.80 | .0101235 | .0086340 |
| 156975.0 | -.11 | -7.64 | -.0003296 | -.0164816 | 302.35 | 302.45 | .0135404 | .0138700 |
| 108086.0 | -.67 | -48.17 | -.0001843 | -.0092135 | 301.96 | 302.63 | .0157857 | .0159700 |
| 61351.0 | -.67 | -48.17 | -.0005943 | -.0297135 | 301.96 | 302.63 | .0157857 | .0163800 |
| 16487.0 | -.67 | -48.17 | -.0008043 | -.0402135 | 301.96 | 302.63 | .0157857 | .0165900 |
| 1718.0 | -2.09 | -150.57 | -.0003449 | -.0172467 | 302.61 | 304.71 | .0163851 | .0167300 |

(note, the interaction is "two-way", that is, every 20 min the convective effect is incorporated into the mesoscale dynamic field; meanwhile the grid condition is updated for initiating the subsequent convection).

The physical basis for making such an assumption comes from the observed convective characteristics over the summer Florida environment. It has long been recognized that in the summer Florida convection, convective downdrafts play an important role in the convective development as well as convective-mesoscale interactions. Byers and Braham (1949) indicated that storm downdrafts tend to produce rather significant surface horizontal gradients of temperature, pressure and divergence, thereby modifying the mesoscale flow. Ulansky and Garstang (1978) found a close relationship between Florida's deep convection and surface convergence produced by cumulus convective downdraft outflows. Cooper et al. (1982) indicated that the convective downdraft is able to modify the mesoscale forcing which originally initiates the convection. Recently, Cunning and DeMaria (1986) observed that the surface cooling produced by downdrafts, together with the sea breeze convergence, is responsible for the enhanced surface convergence and vertical mass transports on both the cloud-scale and mesoscale. As shown in Fig. 3-1 (reproduced from Cunning and DeMaria, 1986), the enhanced mesoscale and cloud-scale mass fluxes increase from System I to System II over a time of about 20 min (1432-1450 EDT).

The essential meaning of using 20 min for the intercommunication is, however, beyond the particular application described above. The purpose is to obtain a more general frequency of intercommunication which is, to the best degree possible, independent of the involved

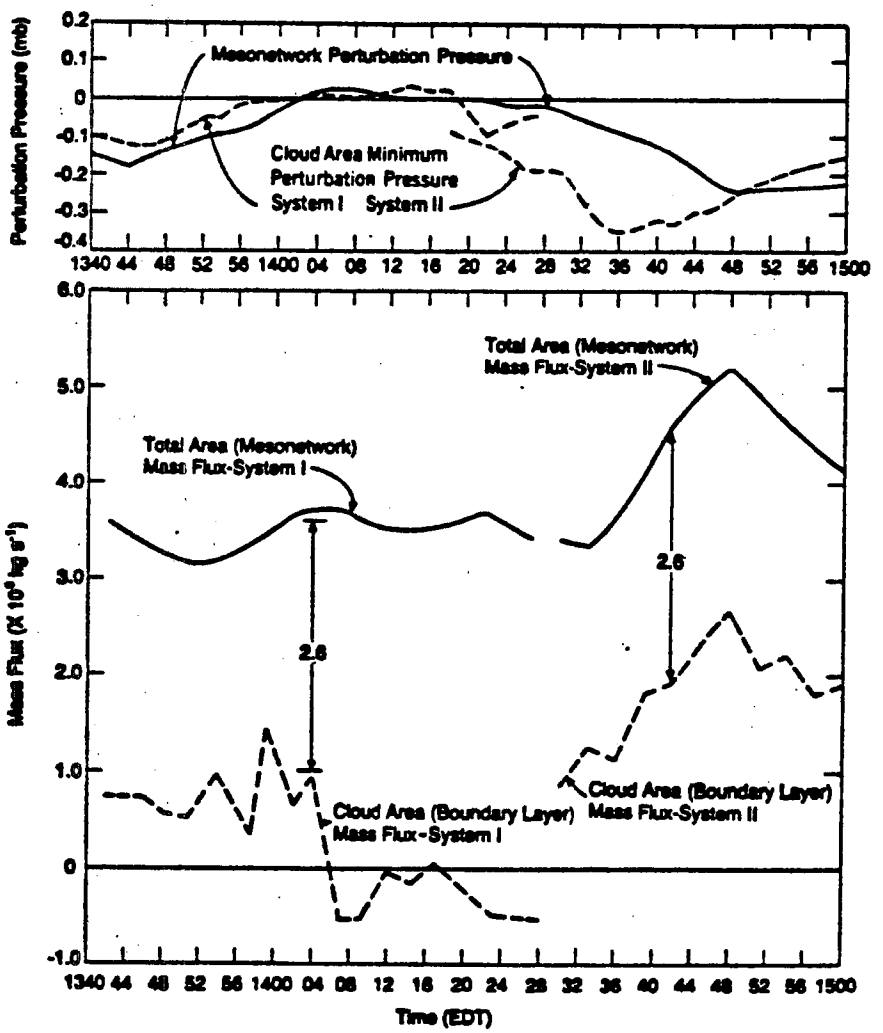


Figure 3-1. The mesoscale pressure perturbation (upper) is the averaged pressure perturbation over the domain of ~ 35 km x 50 km. A constant mesoscale pressure gradient of -0.2 mb 35 $km^{-1}$ in the absence of friction would result in a horizontal wind acceleration of 2.5 $ms^{-1}$/hour. From Cunning and DeMaria (1986).

numerical techniques (such as model resolution, etc.). Cumulonimbus generated downdrafts typically lag convective initiation by about 20 min, regardless of where, when, and how the measurement is taken. Therefore, it is expected that using 20 min (as compared with the 30 min to 1 hour used in FC) should provide a more realistic method to parameterize the convective downdraft effects.

3-2-b. Calculating Convective Intensity

The FC scheme requires that the amount of convection is such that the grid element is completely stabilized during the specified time period (30 min to 1 hour). In the current scheme, since a more frequent interaction is allowed between the subgrid-scale convection and the grid-scale environment, there is no need to "specify" the lifetime for the convective system. That is, the system could evolve through longer or shorter lifetimes depending on the combined factor including its own intensity and the updated grid condition.

For this reason, the current scheme divides the lifetime of any parameterized convection into three stages; namely the developing, mature, and decaying stages, each of 20 min. The developing stage (or Stage 1) is associated with the earlier lifetime of the convection where there is only the environmental forcing (that is, the downdraft effect has not yet developed). The mature stage (or Stage 2) is associated with the enhanced convection due to the combination of the environmental forcing and the convective-generated downdraft forcing (that is, downdraft outflow tends to enhance the convection from which it is generated). Associated with the downdraft enhancement is the surface stabilization produced by the downdraft cooling. Typically during the mature stage of a deep convection, the downdraft process

stabilizes the convection itself, while simultaneously producing enhanced convection (or convergence) in the surrounding immediate environment. The decaying stage (or Stage 3) refers to the rest of the convective lifetime excluding the above two stages. This stage may have a longer or shorter (than 20 min) time period, depending on the degree of grid element stabilization. The above two stages may be needed to be repeated until the stabilization is reached; in which no further convection can develop. The grid element then becomes associated with only resolvable-scale motions. Figure 3-2 shows schematically how the convective effects are parameterized in the current scheme. As indicated earlier, the procedures of initiating deep convection, as well as calculating the level-by-level properties of updraft, downdraft, and the grid-environment (i.e., Step 1 through 8 in Fig. 3-2) follow the general approach of the FC scheme. Although there do exist differences regarding these computational steps between the current scheme and FC scheme, it is found that Step 9 appears to be far more important than other modification made. Therefore, special attention will be paid to Step 9 in the remainder of this section.

The particular observation made by Cunning and DeMaria (1986), shown in Fig. 3-1, shows that the first system they observed (which is not enhanced due to the downdraft effect) has its peak (cloud-scale) mass flux of $1.5 \times 10^{10}$ kg/s, while that for the second system (enhanced by the downdraft effect) reaches about $3.0 \times 10^{10}$ kg/s. This indicates that the "ratio" (shown in Step 9 of Fig. 3-2) is of the magnitude 2.0. Such a value is consistent with that observed by Cooper et al. (1982). That is, the convective downdraft mass flux is comparable to the mesoscale mass flux (at the cloud base level), such that

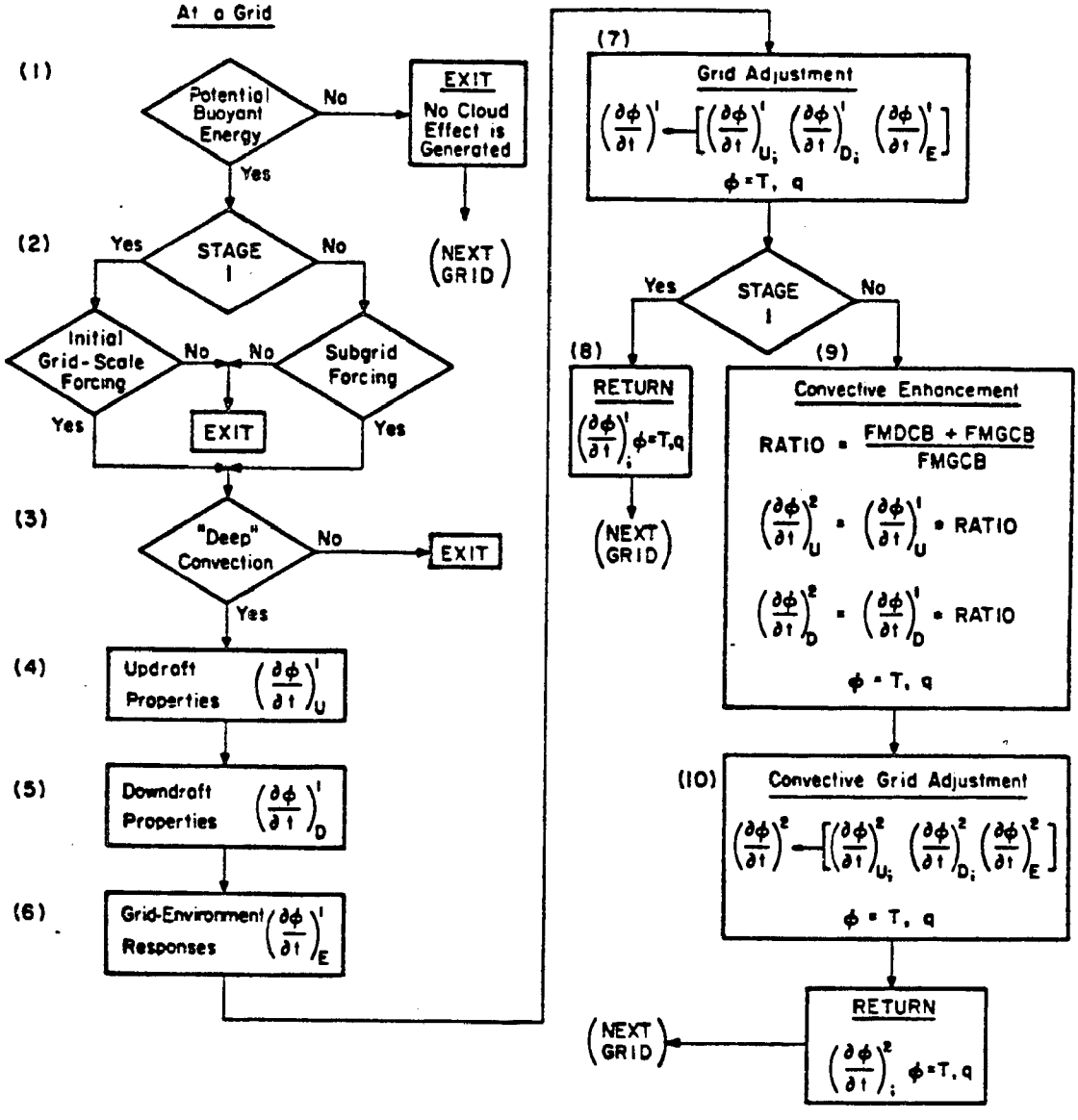


Figure 3-2. A schematic illustration of the convective parameterization used for the moist sea breeze simulations discussed in this study.

when the downdraft enters into the subcloud layer the subsequent convection is "stronger" than the initial convection by a "ratio" formulated in Fig. 3-2. Conceptually, such an assumption is consistent with the fact of considering the "three-dimensional" mass convergence in the subcloud layer (Frank, 1982; personal communication). That is, convection is developed due to both the grid-scale horizontal convergence and the vertical mass influx due to the downdrafts. Therefore, the current scheme calculates the enhanced convective effect for the mature stage by computing the ratio using the updated grid-scale mass flux at cloud base and the updated downdraft mass flux at cloud base.

Finally, Stage 3 involves repeating the first two stages until no new convective initiation occurs. The lifetime for the convective system is ended when the grid element is stabilized. In the rest of this chapter, the current scheme is discussed in detail as to its fidelity, specific ability and general performances. Its application as being incorporated into the moist sea breeze simulation will be illustrated in Chapter 4.

## 3-3 Conservation of Moist Static Energy and Water Substance by the Parameterization

Within a grid volume in which a cumulus parameterization is executed, the overall effect of cumulus convection is to redistribute sensible heat and water substance in the vertical, and to produce net condensation which can reach the surface (i.e., rainfall). Because of this net condensation, there is net heating in the grid volume. Meanwhile, because the net condensation is assumed to exit the domain, there must be net drying in the grid volume. An exact correspondence among the three terms (net heating; surface rainfall; net drying)

indicates conservation of both the moist static energy and water substance.

After the cumulus parameterization is performed, an adjustment to assure exact conservation is achieved by first requiring water substances to be balanced, and then requiring that the final net heating to correspond to the net condensation. An iterative procedure is used to reach the balance conditions. The condition for the convergences is such that the residuals being smaller than the involved quantities by at least two orders of magnitude.

An example of using an arbitrarily selected sounding is given below. The convection produces total condensation during its convective effective time (20 min) of $0.477532 \times 10^{12}$ (g). The total evaporation includes $0.121973 \times 10^{9}$ (kg) (within the downdraft) and $0.379948 \times 10^{8}$ (kg) (from the anvil). Therefore, there is a net condensation of $0.317565 \times 10^{9}$ (kg), corresponding to a rainfall rate of 2.0 (mm/hr) for the grid area of 22 km x 22 km. The resultant final net heating is $0.15788 \times 10^{3}$ (Joule/kg). Table 3-1 summarizes these grid volume net quantities. Detailed vertical distributions of the

Table 3-1.

| | | |
|---|---|---|
| Total condensation (g) | | .477532E+12 |
| Downdraft evaporation (g) | | .121973E+12 |
| Anvil evaporation (g) | | .379948E+11 |
| Net condensation (g) | | .317565E+12 |
| Total rainfall (g) | | .317565E+12 |
| Rain time/area (sec)/cm$^2$ | 1200.0 | .4840E+13 |
| Rainfall rate (mm/hr) | 2.0 | |
| Net latent heating (erg/g) | | .157880E+07 |

convective heating and moistening are listed in Table 3-2 and Table 3-3. In order to show the effect of requiring the conservation

Table 3-3. Parameterization results with the adjustments.

| Z (cm) | $\frac{\delta T}{\delta t}$ ($\frac{°C}{20\ min}$) | $\frac{\delta T}{\delta t}$ ($\frac{°C}{day}$) | $\frac{\delta q}{\delta t}$ ($\frac{g/g}{s}$) | $\frac{\delta q}{\delta t}$ ($\frac{g/kg}{20\ min}$) | $\theta_{new}$ | $\theta_{old}$ | $q_{new}$ | $q_{old}$ |
|---|---|---|---|---|---|---|---|---|
| 2072839.0 | -.01 | -.60 | -.0000000 | -.0000000 | 475.99 | 476.00 | .0000100 | .0000100 |
| 1662468.0 | -.23 | -16.46 | -.0000000 | -.0000000 | 367.06 | 367.28 | .0000100 | .0000100 |
| 1421823.0 | -.53 | -38.39 | .0001031 | .0051568 | 337.79 | 338.32 | .0001132 | .0000101 |
| 1243921.0 | .09 | 6.83 | .0000019 | .0000940 | 335.40 | 335.31 | .0000119 | .0000100 |
| 1096781.0 | 1.14 | 81.90 | .0000952 | .0047594 | 333.22 | 332.08 | .0001110 | .0000158 |
| 970418.0 | 1.64 | 118.07 | -.0000571 | -.9925844 | 330.70 | 329.06 | .0002980 | .0003497 |
| 760291.0 | .73 | 52.69 | -.0000669 | -.0033432 | 323.75 | 323.02 | .0014301 | .0014970 |
| 589461.0 | .82 | 58.71 | -.0001616 | -.0080795 | 316.33 | 315.52 | .0034164 | .0035780 |
| 445078.0 | .42 | 29.89 | .0009284 | .0464198 | 310.35 | 309.94 | .0044654 | .0035370 |
| 319663.0 | .17 | 12.06 | .0003888 | .0194398 | 305.37 | 305.20 | .0076408 | .0072520 |
| 319663.0 | .17 | 12.06 | .0003888 | .0194398 | 305.37 | 305.20 | .0076408 | .0072520 |
| 208384.0 | -.01 | -.60 | .0014065 | .0703240 | 303.79 | 303.80 | .0100405 | .0086340 |
| 156975.0 | -.11 | -7.91 | -.0003777 | -.0188827 | 302.34 | 302.45 | .0134923 | .0138700 |
| 108086.0 | -.67 | -48.36 | -.0002260 | -.0112987 | 301.96 | 302.63 | .0157440 | .0159700 |
| 61351.0 | -.67 | -48.36 | -.0006360 | -.0317987 | 301.96 | 302.63 | .0157440 | .0163800 |
| 16487.0 | -.67 | -48.36 | -.0008460 | -.0422987 | 301.96 | 302.63 | .0157440 | .0165900 |
| 1718.0 | -2.09 | -150.57 | -.0004506 | -.0225320 | 302.61 | 304.71 | .0162794 | .0167300 |

of both moist static energy and water substance in the parameterization, the heating/moistening are listed separately for the cases without (Table 3-2) and with (Table 3-3) the adjustment.

Comparing Table 3-2 and Table 3-3, we see that due to the iterations of requiring the conservation, the maximum heating, for example, changes by only 0.3 percent. The maximum cooling at surface changes by only negligible amount (smaller than the second decimal point). Therefore, we see that the parameterized net heating is essentially conserved without the conservation readjustment.

Relatively larger effects appear only on the humidity quantities, but the absolute value of the residuals are still significantly smaller than variation due to phyical processes. For example, both the mid-tropospheric moistening (at level 7) and surface drying are changed by only 0.6 percent. The only relatively large change is at cloud top (detrainment induced evaporational moistening), which changes by about 25 percent. Since moisture content is typically negligible at that height (14 km), the change is considered not important.

## 3-4 Sensitivity Experiments with the Deep Convective Parameterization

In this section, sensitivity experiments of the cumulus parameterization will be performed and discussed. The purpose of these experiments is to understand quantitatively the involved sensitivities of the parameterization performance due to several assumptions used in the cumulus parameterization. In the following sub-sections, all the sensitivities will be shown quantitatively by the convective heating/moistening (over a 20-min. period), or by other cloud properties which are most related to the parameter chosen for the sensitivity test.

Other parameterization quantities not discussed in this section are found to be relatively insensitive to the chosen parameter.

3-4-a. Sensitivity to the Non-hydrostatic Parameter in the Vertical Equation of Motion

The β parameter in the vertical velocity equation is, as indicated in Kreitzberg and Perkey (1976), associated with the compensating effect of neglecting the nonhydrostatic pressure perturbation in the buoyancy equation. It is realized that there are other important terms in the complete buoyancy equation (such as the vertical pressure gradient and loading term, etc.). However, since cloud-scale pressure field and microphysical processes are not included in the current scheme, the sensitivity concerning the buoyancy equation is only on the β term.

Table 3-4 indicates the effects of varying β.

Table 3-4.

| β | $W_{u,max}$ (m/s) | Max. Heating (°C/20 min) | (°C/day) |
|---|---|---|---|
| 0.1 | 53.7 | 1.79 | 128.9 |
| 0.3 | 49.4 | 1.79 | 128.9 |
| 0.5 | 46.0 | 1.80 | 129.6 |
| 0.7 | 43.2 | 1.80 | 129.6 |
| 0.9 | 40.8 | 1.80 | 129.6 |

It is seen that increasing the β from 0.1 to 0.9 decreases the vertical maximum velocity by about 25 percent. The final convective maximum heating is essentially unchanged, however. Therefore, it is clear that the β parameter has relatively little effect upon the performance of the cumulus parameterization.

3-4-b. Sensitivity to Precipitation Efficiency

In the following sensitivity experiment (Table 3-5), precipitation efficiency (PEF) is varied using the values 10, 30, 50, 70 and 90 percent.

Table 3-5.

| PEF | Total rainfall (g/s) | (mm/hr) | $\Delta TD_{ML}$* | Anvil-Evaporational cooling (°C) | moistening (g/kg) |
|---|---|---|---|---|---|
| 10% | $0.81 \times 10^8$ | ~0.8 | -2.97 | -2.02 | +0.0954 |
| 30% | $0.24 \times 10^9$ | ~2.3 | -3.25 | -2.01 | +0.0691 |
| 50% | $0.41 \times 10^9$ | ~4.0 | -3.54 | -1.94 | +0.0428 |
| 70% | $0.57 \times 10^9$ | ~6.0 | -3.82 | -0.45 | +0.0164 |
| 90% | $0.73 \times 10^9$ | ~8.0 | -4.10 | -0.08 | -0.0099 |

* $\Delta TD_{ML}$: Downdraft temperature-deficit in the melting layer.

It is seen that using a larger PEF results in somewhat stronger downdraft (stronger cooling in the melting layer) and somewhat weaker anvil evaporation (weaker cooling and moistening in the anvil layer) than using a smaller PEF. Except for the anvil layer, the final convective heating and moistening, however, are essentially unchanged.

3-4-c. Sensitivity to Ice-Percentage of the Total Liquid Condensate

The ice-percentage refers to the fraction of total liquid condensate produced in lower troposphere (below the -5°C level) which is then converted to ice in the upper troposphere. Table 3-6 shows the effects of changing the ice-percentage (FRACI).

It is seen that changing the ice-percentage affects the determination of cloud depth more significantly than that of the final maximum heating. The latter is basically not affected by the

Table 3-6.

| FRACI | Cloud depth (km) | Max. heating (°C) |
|---|---|---|
| 10% | 10.0 | 1.79 |
| 30% | 13.6 | 1.80 |
| 50% | 13.6 | 1.80 |

ice-percentage effect. The increase of cloud depth, using FRACI values from 30 percent to 50 percent, is generated by an extra buoyancy of +1.11°C near 10 km for the updraft. Meanwhile, the downdraft obtains an extra negative buoyancy of -0.66°C near 3.6 km (within the melting layer).

3-4-d. Sensitivity to Entrainment Rate

Entrainment rate is referred to as the rate of the mass increase with height for updraft or downdraft. In this subsection, three entrainment rates are considered for the sensitivity test: a zero-entrainment case (i.e. updraft mass does not increase with height); a case in which updraft mass increases two times from cloud base to the maximum mass flux level; and a case of four times increase. In Table 3-7, case 1, 2, 3 refer to, respectively, the zero-entrainment, doubling, and quadruple cases.

Table 3-7

| Case | Downdraft mass flux at cloud base (g/s) | Total updraft-produced condensate (g/s) | Total downdraft evaporation (g/s) | Cloud depth (km) | Final surface cooling (°C) | Max. upper heating (°C) |
|---|---|---|---|---|---|---|
| 1 | $0.25\times10^{11}$ | $0.73\times10^{9}$ | $0.14\times10^{9}$ | 14.3 | -5.04 | +0.96 |
| 2 | $0.42\times10^{11}$ | $0.89\times10^{9}$ | $0.22\times10^{9}$ | 13.6 | -6.02 | +1.80 |
| 3 | $0.76\times10^{11}$ | $1.21\times10^{9}$ | $0.37\times10^{9}$ | 9.3 | -7.52 | +2.05 |

It is seen that, as expected, both updraft and downdraft intensities are rather significantly dependent upon the entrainment rate. Accordingly, cloud depth varies with the entrainment rate. The final convective heating, although being more sensitive to the entrainment rate than to the parameters discussed in Section 3-4-a to 3-4-c, changes by only about 0.2°C for the heating and 1.5°C for the cooling (between case 2 and case 3).

3-4-e. Sensitivity to Initial Downdraft Thermodynamic Property

At the downdraft initiation level, the initial downdraft temperature and humidity are assumed to be weighted averages between the updraft and the environments values. That is:

$$\begin{matrix}\text{Initial}\\ \text{downdraft}\\ \text{property}\end{matrix} = \alpha \cdot \left(\begin{matrix}\text{environmental}\\ \text{property}\end{matrix}\right) + (1 - \alpha) \cdot \left(\begin{matrix}\text{updraft}\\ \text{property}\end{matrix}\right)$$

Table 3-8 shows the effects of changing the weighting factor $\alpha$.

Table 3-8

| $\alpha$ | Downdraft surface max. temperature deficit (°C) | Max. cooling at surface (°C) |
|---|---|---|
| 10% | -11.82 | -5.20 |
| 30% | -12.34 | -5.39 |
| 50% | -12.80 | -5.56 |
| 70% | -13.40 | -5.79 |
| 90% | -13.99 | -6.02 |

It is seen that between a "50-50 mixture" assumption (i.e. $\alpha$ = 50 percent) and the $\alpha$ = 90 percent assumption, the final surface cooling differ by only about 0.5°C. Therefore, the downdraft intensity is relatively insensitive to its initial thermodynamic property.

3-4-f. Sensitivity to Initial Downdraft Massflux

In this sensitivity experiment, the initial downdraft massflux is assumed to be the updraft massflux at cloud base multiplied by a ratio, $\nu$. That is, initial downdraft massflux = $\nu$ · initial updraft massflux (at cloud base). Johnson (1976) discussed in more details about this ratio. Table 3-9 shows the effects of changing $\nu$.

It is seen that, as expected, downdraft intensity is directly proportional to its initial massflux. The maximum surface cooling/drying change significantly with $\nu$, indicating significant variations of downdraft stabilization effects. For larger values of $\nu$ from 50 percent to 90 percent (which are expected to be characteristic of downdrafts initiating in the lower troposphere) the change in maximum

Table 3-9.

| | Downdraft massflux at cloud base (g/s) | Fraction of surface grid area of the downdraft replacement (%) | Max. final surface-layer cooling (°C) | drying (g/kg) |
|---|---|---|---|---|
| 10% | $0.85 \times 10^{10}$ | 14.3 | -1.89 | -0.024 |
| 30% | $0.26 \times 10^{11}$ | 33.3 | -4.41 | -0.057 |
| 50% | $0.43 \times 10^{11}$ | 45.5 | -6.02 | -0.078 |
| 70% | $0.60 \times 10^{11}$ | 53.8 | -7.13 | -0.092 |
| 90% | $0.77 \times 10^{11}$ | 60.0 | -7.94 | -0.103 |

final surface-layer cooling and drying are about 25 percent (which reflects an estimated magnitude of an existing source of uncertainty in the model. More detailed analysis on this is underway).

3-4-g. Sensitivity to Downdraft Relative Humidity

In this sensitivity experiment, for a downdraft relative humidity (RHD) $\lesssim$ 50 percent, there is not enough cooling to sustain the downdraft, or not enough cooling for the downdraft to reach the sub-cloud layer. Therefore, only 70 percent and 90 percent are considered. Table 3-10 shows the effects of changing RHD.

Table 3-10.

| RHD | Downdraft evaporation (g/s) | Max. surface temperature deficit (°C)** | Max. surface** cooling (°C) | drying (g/kg) |
|---|---|---|---|---|
| 70% | $0.17 \times 10^9$ | -11.11 | -4.63 | -0.102 |
| 90% | $0.22 \times 10^9$ | -13.99 | -6.02 | -0.078 |

**The surface cooling is the surface temperature deficit times the fraction of grid area associated with the surface-layer downdraft replacement.

It is seen that, for RHD = 70 percent, there is relatively smaller cooling and larger drying in the surface layer; while for RHD = 90 percent there is larger cooling and smaller drying. The maximum difference is 1.4°C for cooling and 0.024 (g/kg) for drying.

3-5 Deep Convective Modification Upon Boundary Layer Processes

Observations show that the Florida deep cumulonimbus convection on undisturbed days during the summer, typically do not develop until about 11 AM local time (Pielke and Cotton, 1977). Before 11 AM, the combination of solar radiation and the thermal contrast between land and sea gradually produces land/sea differences of convective available potential energy (CAPE). The CAPE is defined as the vertically integrated (net) buoyant energy for a surface air parcel; higher values of CAPE indicates larger convective potential. Figure 3-3 shows how

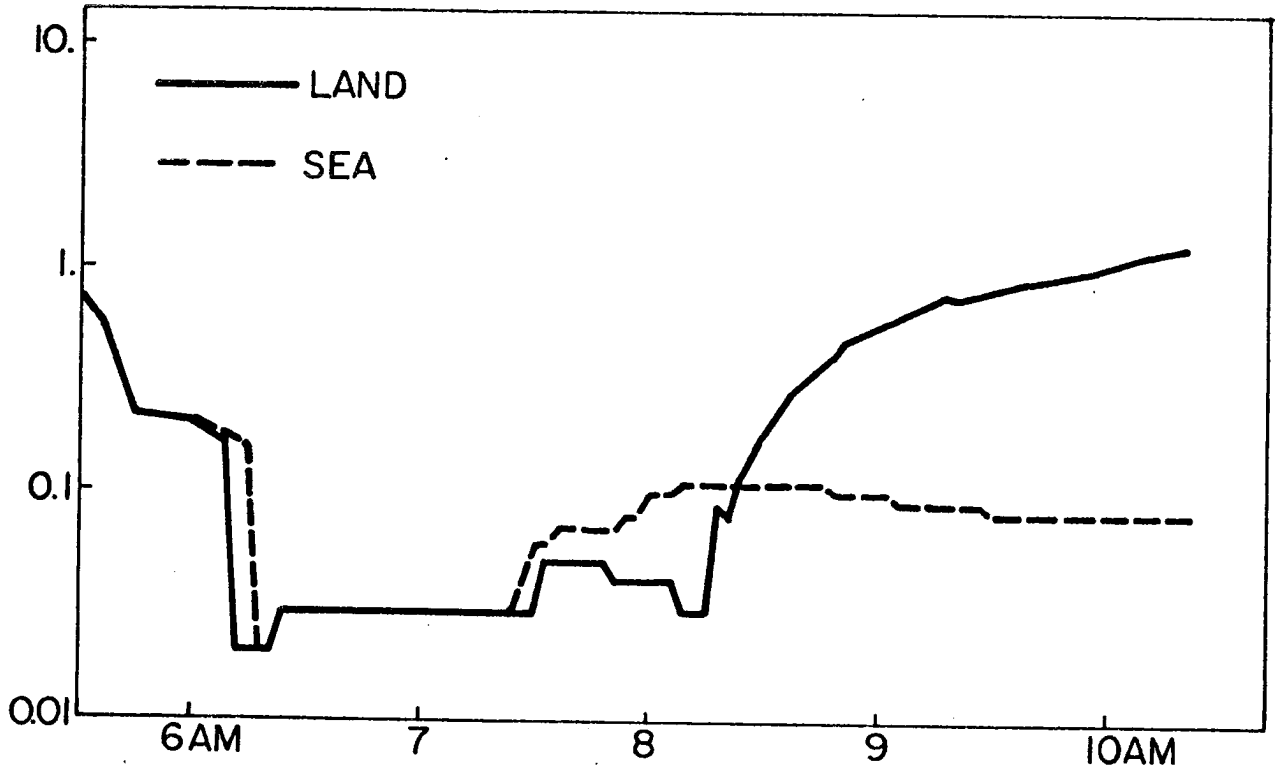


Figure 3-3. The calculated CAPE over a land and a water grid point during the morning hours (using the initial condition of the control run).

land/sea difference of CAPE is established during the morning hours of a typical sea breeze day. It is clear that during the daytime, the convective potential is much higher over the land than over the sea, consistent with observations.

Since the CAPE over the land surface in the morning is developed solely through boundary layer turbulence without any latent heating processes involved, the calculation in the model for the morning hours is following that of Pielke and Mahrer (1978), which is described in detail in Appendix A. When the convective potential is sufficiently large (say after 10 AM, over the land surface), typically shallow nonprecipitating cumulus clouds develop over land. These shallow clouds provide net moistening within the lower troposphere (about 2-4 km above ground) which is found to be important for subsequent deep convection to initiate (Johnson, 1978). Following Frank (1982, personal communication), this shallow-cumulus moistening effect is crudely included in the parameterization. The method is to distribute the "updraft" moisture (that is, the humidity content of the most unstable layer near surface) into the grid-environment when the updraft does not reach a height of 4 km above ground. Typically such updraft occupies on the order of 1 percent of the grid area. Clouds reaching heights above 4 km are considered deep convection and will be included in the parameterization.

After about 11 AM until sunset, typically there is deep cumulus convection over south Florida. Due to the deep convectively generated downdrafts, the boundary layer turbulence motions are subject to significant modifications. In addition to a cooler surface temperature in the convective areas relative to the nonconvective areas, the boundary

layer thickness is changed. As detailed in Appendix A, the dry boundary layer height is calculated using the formulation of Deardorff (1974). When deep convection is produced, the grid-environmental subsidence motion lowers the boundary layer height while the surface cooling reduces the surface upward heat flux. The combination of these two processes forms the modification upon Deardorff's PBL height equation due to convection. Figure 3-4 shows the surface temperature and PBL height for a dry sea breeze simulation and a moist sea breeze simulation. It is seen, for example, the PBL height is lower by about 400 m between 3-4 PM due to the deep convective effect.

## 3-6 The Subgrid-scale Convective Contribution to a Hydrostatic Kinetic Energy Budget Equation

When the hydrostatic assumption is used to construct a numerical model, vertical velocity is diagnosed using the horizontal velocities. Thus there is no hydrostatic kinetic energy source/sink over the domain due to the vertical motion. This is true for the grid-scale processes. However, if convective activities are considered to be important within the domain, then there are subgrid-scale contributions which may be nonhydrostatic. For example, convective heating can be parameterized within a hydrostatic model which provides energy that is not associated with hydrostatic processes.

In this section, it is intended to approximately compare the kinetic energy associated with subgrid-scale deep convection with that associated with grid-scale horizontal velocities as prognosed in a hydrostatic model. Since such a comparison is necessarily dependent upon the intensity of the horizontal wind, the comparison to be illustrated below applies only to the summer Florida environment where deep

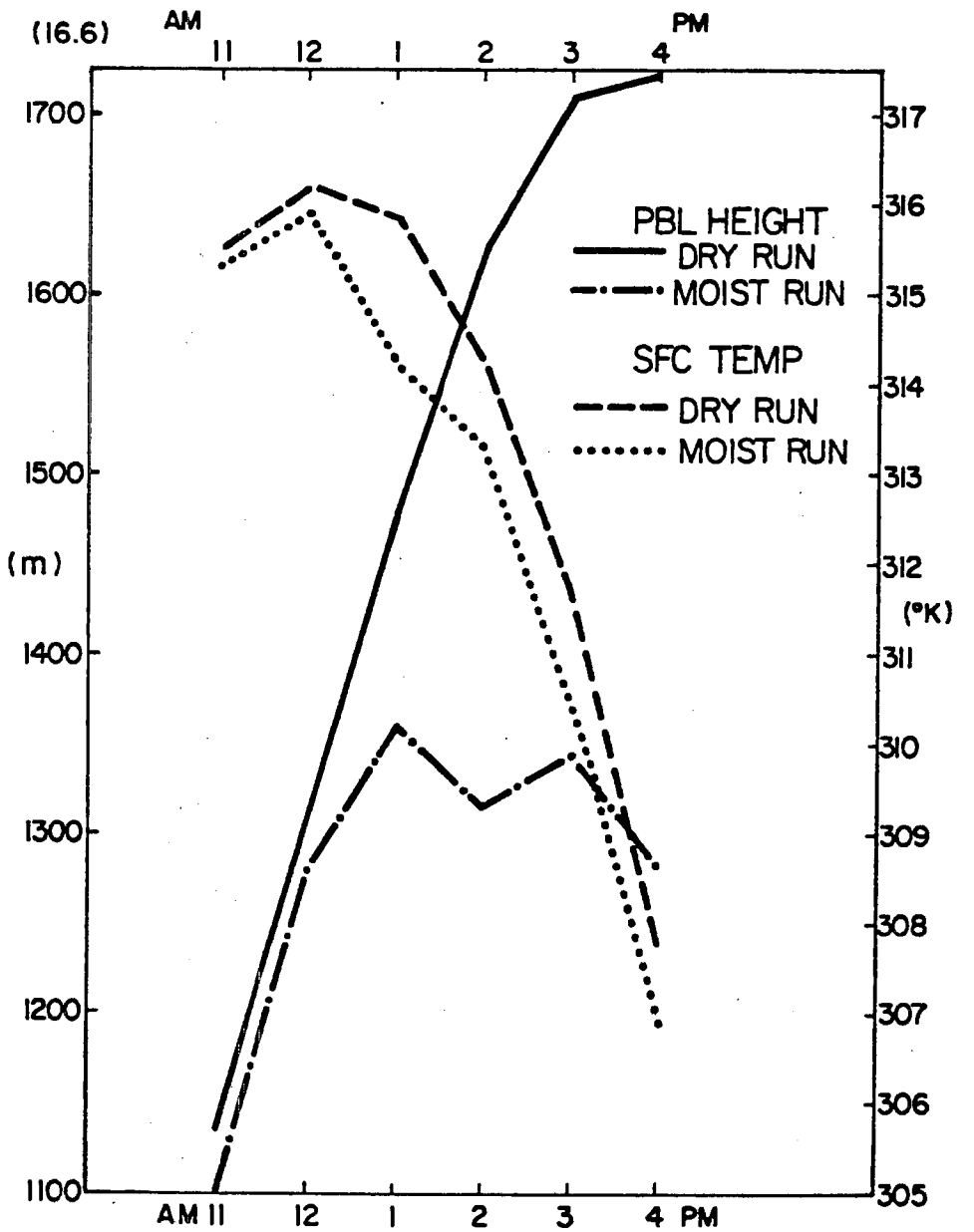


Figure 3-4. The calculated surface temperature and PBL height during the afternoon at a land point over south Florida.

convection is regularly modulated by the lower tropospheric sea breeze circulation.

Because the three-dimensional motion field associated with deep convection must be resolved in order to compare the vertical and horizontal kinetic energy, the cloud-scale fully-compressible nonhydrostatic model developed by Cotton and Tripoli (1978) and Tripoli and Cotton (1980) is utilized. The cloud model is initialized with the composite wind and thermodynamic profiles used in Tripoli and Cotton (1980), which represent a preconvective situation for July 17, 1973 over south Florida.

During the cloud model simulation, the domain horizontally averaged values of horizontal kinetic energy ($1/2(\overline{u}^2+\overline{v}^2)$) and vertical kinetic energy ($1/2\ \overline{w}^2$) are calculated every 2 minutes (the overbar indicates horizontal averages over the cloud-model domain) and presented in Table 3-11. A vertical profile is established for the ratio of the above two quantities ($\overline{w}^2/(\overline{u}^2+\overline{v}^2)$) after each time step. Finally, a time-averaged profile of the ratio term is established over the total simulation time corresponding to the typical lifetime of a deep cumulonimbus cloud (about 35 min).

For the particular physical background chosen, such a time-averaged profile of the ratio term provides a first order representation as to quantitatively how the subgrid-scale deep convection affects the grid-scale (i.e., mesoscale) horizontal kinetic energy budget. Table 3-12 shows that over the vertical domain the ratio depends on height but is generally on the order of unity. Relatively larger ratios are found around the middle troposphere (~3-7 km), where the cloud mass is accelerating upwards.

Table 3-11.

Ratio of $w^2/(u^2+v^2)$

| | | | | | | | | | | | | | | | | | | |
|---|---|---|---|---|---|---|---|---|---|---|---|---|---|---|---|---|---|---|
| 28 | 20 km | 0.00 | 0.00 | 0.00 | 0.00 | 0.00 | 0.00 | 0.00 | 0.00 | 0.00 | 0.00 | 0.00 | 0.00 | 0.00 | 0.00 | 0.00 | 0.00 | 0.00 |
| 27 | | 0.00 | 0.00 | 0.00 | 0.00 | 0.00 | 0.00 | 0.00 | 0.00 | 0.00 | 0.00 | 0.00 | 0.00 | 0.00 | 0.00 | 0.00 | 0.00 | 0.00 |
| 26 | | 0.00 | 0.00 | 0.00 | 0.00 | 0.00 | 0.00 | 0.00 | 0.00 | 0.00 | 0.00 | 0.07 | 0.08 | 0.08 | 0.21 | 0.13 | 0.21 | 0.05 |
| 25 | | 0.00 | 0.00 | 0.00 | 0.00 | 0.00 | 0.00 | 0.00 | 0.00 | 0.04 | 0.10 | 0.13 | 0.19 | 0.19 | 0.21 | 0.18 | 0.30 | 0.08 |
| 24 | | 0.00 | 0.00 | 0.00 | 0.00 | 0.00 | 0.00 | 0.00 | 0.04 | 0.09 | 0.12 | 0.15 | 0.18 | 0.13 | 0.15 | 0.16 | 0.21 | 0.08 |
| 23 | | 0.00 | 0.00 | 0.00 | 0.00 | 0.00 | 0.00 | 0.00 | 0.02 | 0.09 | 0.11 | 0.10 | 0.11 | 0.11 | 0.12 | 0.11 | 0.17 | 0.06 |
| 22 | 15 km | 0.00 | 0.00 | 0.00 | 0.00 | 0.00 | 0.00 | 0.02 | 0.03 | 0.09 | 0.09 | 0.13 | 0.14 | 0.12 | 0.08 | 0.11 | 0.13 | 0.09 |
| 21 | | 0.00 | 0.00 | 0.00 | 0.00 | 0.00 | 0.01 | 0.05 | 0.06 | 0.07 | 0.09 | 0.12 | 0.11 | 0.08 | 0.06 | 0.09 | 0.08 | 0.05 |
| 20 | | 0.00 | 0.00 | 0.00 | 0.00 | 0.00 | 0.01 | 0.11 | 0.12 | 0.10 | 0.10 | 0.17 | 0.16 | 0.13 | 0.10 | 0.16 | 0.13 | 0.08 |
| 19 | | 0.00 | 0.00 | 0.00 | 0.00 | 0.01 | 0.04 | 0.19 | 0.24 | 0.20 | 0.20 | 0.30 | 0.33 | 0.28 | 0.29 | 0.43 | 0.34 | 0.18 |
| 18 | | 0.00 | 0.00 | 0.00 | 0.00 | 0.01 | 0.09 | 0.27 | 0.31 | 0.26 | 0.27 | 0.34 | 0.34 | 0.29 | 0.37 | 0.52 | 0.43 | 0.22 |
| 17 | | 0.00 | 0.00 | 0.00 | 0.01 | 0.03 | 0.18 | 0.41 | 0.39 | 0.28 | 0.29 | 0.36 | 0.33 | 0.30 | 0.43 | 0.55 | 0.46 | 0.25 |
| 16 | | 0.00 | 0.00 | 0.00 | 0.01 | 0.08 | 0.33 | 0.55 | 0.41 | 0.29 | 0.35 | 0.39 | 0.36 | 0.33 | 0.51 | 0.54 | 0.48 | 0.29 |
| 15 | 10 km | 0.00 | 0.00 | 0.00 | 0.02 | 0.16 | 0.53 | 0.54 | 0.38 | 0.32 | 0.39 | 0.40 | 0.41 | 0.41 | 0.60 | 0.55 | 0.56 | 0.33 |
| 14 | | 0.00 | 0.00 | 0.00 | 0.06 | 0.33 | 0.65 | 0.47 | 0.38 | 0.40 | 0.43 | 0.43 | 0.48 | 0.51 | 0.64 | 0.59 | 0.65 | 0.38 |
| 13 | | 0.00 | 0.00 | 0.01 | 0.17 | 0.75 | 0.69 | 0.47 | 0.44 | 0.52 | 0.54 | 0.50 | 0.55 | 0.62 | 0.70 | 0.67 | 0.76 | 0.46 |
| 12 | | 0.00 | 0.00 | 0.03 | 0.50 | 1.58 | 0.78 | 0.64 | 0.66 | 0.80 | 0.84 | 0.75 | 0.77 | 0.89 | 0.89 | 0.97 | 1.04 | 0.70 |
| 11 | | 0.00 | 0.00 | 0.13 | 1.38 | 2.01 | 0.85 | 0.82 | 0.99 | 1.18 | 1.21 | 1.14 | 1.10 | 1.21 | 1.28 | 1.35 | 1.22 | 0.99 |
| 10 | | 0.00 | 0.03 | 0.35 | 3.40 | 1.78 | 0.98 | 1.02 | 1.43 | 1.74 | 1.56 | 1.50 | 1.37 | 1.53 | 1.61 | 1.63 | 1.32 | 1.33 |
| 9 | | 0.00 | 0.11 | 1.01 | 6.61 | 1.71 | 1.32 | 1.38 | 1.75 | 2.18 | 2.07 | 1.91 | 1.94 | 2.05 | 1.97 | 1.62 | 1.21 | 1.80 |
| 8 | 5 km | 0.00 | 0.20 | 2.50 | 4.63 | 1.62 | 1.55 | 1.59 | 1.71 | 1.85 | 1.98 | 1.77 | 1.89 | 2.09 | 1.54 | 1.36 | 1.21 | 1.72 |
| 7 | | 0.00 | 0.37 | 6.61 | 3.57 | 2.04 | 1.75 | 1.63 | 1.63 | 1.54 | 1.48 | 1.76 | 1.61 | 1.56 | 1.20 | 1.06 | 1.17 | 1.81 |
| 6 | | 0.00 | 0.60 | 4.40 | 1.27 | 0.76 | 0.56 | 0.53 | 0.64 | 0.67 | 0.90 | 1.04 | 0.96 | 0.77 | 0.77 | 0.83 | 0.96 | 0.98 |
| 5 | | 0.00 | 1.35 | 2.62 | 0.54 | 0.27 | 0.20 | 0.24 | 0.42 | 0.70 | 1.17 | 1.22 | 0.83 | 0.66 | 0.60 | 0.67 | 0.67 | 0.76 |
| 4 | | 0.00 | 0.13 | 0.15 | 0.08 | 0.07 | 0.09 | 0.10 | 0.09 | 0.09 | 0.14 | 0.25 | 0.35 | 0.47 | 0.58 | 0.53 | 0.49 | 0.23 |
| 3 | | 3.22 | 1.10 | 0.80 | 0.48 | 0.26 | 0.18 | 0.15 | 0.14 | 0.14 | 0.16 | 0.26 | 0.32 | 0.29 | 0.27 | 0.25 | 0.22 | 0.51 |
| 2 | | 0.07 | 0.06 | 0.04 | 0.03 | 0.02 | 0.02 | 0.02 | 0.02 | 0.02 | 0.02 | 0.04 | 0.08 | 0.08 | 0.09 | 0.09 | 0.09 | 0.05 |
| 1 | | 0.07 | 0.06 | 0.04 | 0.03 | 0.02 | 0.02 | 0.02 | 0.02 | 0.02 | 0.02 | 0.04 | 0.07 | 0.08 | 0.08 | 0.09 | 0.09 | 0.05 |

Time ($\Delta t$ = 2 min) →

According to this analysis, we see that for a grid element (in a mesoscale model) in which deep convection is generated, the convection tends to produce vertical kinectic energy which is comparable to the cloud-domain averaged horizontal kinetic energy. Such a relationship depends somewhat on height with the importance of vertical kinetic energy generation being greater around the midtroposphere.

Table 3-12 shows the horizontal kinetic energy tendency profile obtained from the parameterized convection and the time-averaged ratio profile as obtained from Table 3-11. The diagnostic cloud calculation of the parameterization was integrated for the same background thermodynamic and wind sounding as used to run the nonhydrostatic cumulus model. The parameterized horizontal kinetic energy obtained from the diagnostic cloud model is calculated as:

$$K^{\tau}_{cu_j} = \frac{1}{2} \cdot F_j \cdot (\delta_u \cdot w_u^2 + \delta_D \cdot w_D^2 + \delta_E \cdot w_E^2); \quad \left.\frac{\delta K}{\delta t}\right|_{cu_j} = \left(\frac{K^{\tau+1}_{cu} - K^{\tau}_{cu}}{\Delta t}\right)_j$$

where, $K^{\tau}_{cu_j}$, $\left.\frac{\delta K}{\delta t}\right|_{cu_j}$ = kinetic energy and its tendency due to the parameterized convective effect. (Subscript j indicates the vertical level).

$F_j$ = the ratio of $w^2/(u^2+v^2)$ obtained from Table 3-11.

$\delta_u$, $\delta_D$, $\delta_E$ / $w_u$, $w_D$, $w_E$ = fractional coverage and vertical velocity of updraft, downdraft, and grid-environment.

$\Delta t$ = time interval for evaluating the tendency.

It is seen from Table 3-12 that the convective contribution upon the mesoscale horizontal kinetic energy (i.e., the $\delta K/\delta t|_{cu}$ term) has a peak around the mid-troposphere and another peak within the lowest 1 km, both with magnitudes of 2-3 watt/$m^2$/km. The mid-tropospheric peak is associated with the comparatively strong values of $w_u$. Within the lowest 1 km or so, the peak of the $\delta K/\delta t|_{cu}$ term is related to

Table 3-12

| Z (cm) | Ratio | $\frac{\delta K}{\delta t}_{cu}$ ($\frac{watt}{m^2}$/km) |
|---|---|---|
| 2072839.0 | 0.00 | 0.0 |
| 2001421.0 | 0.00 | 0.0 |
| 1930003.1 | 0.00 | 0.0 |
| 1858585.1 | 0.05 | 0.0 |
| 1787167.1 | 0.08 | 0.0 |
| 1715749.2 | 0.08 | 0.0 |
| 1644331.2 | 0.07 | 0.0 |
| 1572913.2 | 0.07 | 0.0 |
| 1501495.3 | 0.07 | 0.565E-11 |
| 1430077.3 | 0.06 | 0.197E-01 |
| 1358659.3 | 0.13 | 0.105E+00 |
| 1287241.4 | 0.20 | 0.237E+00 |
| 1215823.4 | 0.24 | 0.376E+00 |
| 1144405.4 | 0.25 | 0.488E+00 |
| 1072987.5 | 0.29 | 0.676E+00 |
| 1001569.5 | 0.33 | 0.884E+00 |
| 930151.6 | 0.38 | 0.112E+01 |
| 858733.6 | 0.46 | 0.123E+01 |
| 787315.6 | 0.70 | 0.166E+01 |
| 715897.7 | 0.99 | 0.209E+01 |
| 644479.7 | 1.33 | 0.246E+01 |
| 573061.7 | 1.80 | 0.282E+01 |
| 501643.8 | 1.76 | 0.225E+01 |
| 430225.8 | 1.76 | 0.177E+01 |
| 358807.8 | 1.40 | 0.123E+01 |
| 287389.9 | 0.87 | 0.592E+00 |
| 215971.9 | 0.50 | 0.257E+00 |
| 144553.9 | 0.37 | 0.244E+00 |
| 73136.0 | 0.28 | 0.282E+01 |
| 1718.0 | 0.05 | 0.251E-04 |

the downdraft outflow in which the downdraft is deflected into horizontal flow by the ground. A similar phenomenon (i.e., vertical flow deflected into horizontal flow) may occur around cloud top. However, the horizontal detrainment process (which creates the anvil) takes place over a much thicker layer than the surface layer. Therefore, there is no corresponding peak in the upper troposphere.

In the particular moist sea breeze simulation performed in the present study, the mesoscale kinetic energy budget components are typically with magnitudes of: 10-30 watt/$m^2$/km for the cross-contour pressure gradient force term; and 1-10 watt/$m^2$/km for the horizontal and vertical flux convergence terms. Near the surface, the mesoscale budget components have magnitudes of about 2-4 watt/$m^2$/km. Therefore, for this particular simulation, the direct contribution of deep convection to the grid-area horizontal kinetic energy does not seem to be crucial to the overall atmospheric developments on the mesoscale environment surrounding the deep convection.

# Chapter 4

# SEA BREEZE - DEEP CUMULUS CONVECTIVE INTERACTIONS

## 4-1. Introduction

During the last decade there has been considerable interest in understanding mesoscale weather systems and their interactions with both large-scale circulations and cumulus convection. An ideal location for examining these interactions is the south Florida peninsula where mesoscale sea breeze circulations on both coasts regularly initiate deep convection on synoptically undisturbed days.

A considerable amount of observational study has been devoted to the south Florida mesoscale region bounded by the east and west coasts and Lake Okeechobee. Frank, Moore, and Fisher (1967), for example, have summarized radar analyses on the peninsula-scale convective patterns for a diurnal period, as well as related shower activity to the regular displacement of the sea breeze convergence zone. The convective-scale data network (FACE) has also provided valuable help in understanding thunderstorm processes and how storms interact with their immediate mesoscale environment (e.g., Cunning et al., 1982; Cooper et al., 1982; among others). The role played by the diurnally varying sea breeze circulation in modulating the convective activities has been numerically simulated which provides further insight as to large-scale-mesoscale-cumulus convective interactions (e.g., Pielke, 1974; Pielke and Mahrer, 1978; Simpson et al., 1980; among others).

The relationship between convective rainfall and peninsula-scale forcing has also been investigated by Burpee (1979) and Burpee and Lahiff (1984), in which it was concluded that the mid-tropospheric moistening (due to pre-existing convection) is important for generating convective rainfall during the afternoon period. A thorough statistical analysis of Florida's convective activities performed by Lopez et al. (1984a,b) confirmed that the majority of Florida's mesoscale convective systems are mergers of smaller systems, being consistent with the earlier finding of the "tendency to form clusters" (Byers and Braham, 1949) and the merging hypothesis of Simpson et al., (1980).

However, due to the difficulties of performing a peninsula-scale observational program, investigations of the convective feedback effects upon the mesoscale sea breeze circulation and on the peninsula-scale environment have been very limited. From the point of view of understanding Florida's sea breeze-convective interactions, it is unfortunate that there have been essentially no mesoscale/peninsula-scale observations which also include storm-environmental interactions. This is unfortunate for at least two reasons:

(1) The sea breeze circulation is clearly a mesoscale to peninsular-scale phenomenon; therefore if the sea breeze-deep cumulus convective interactions can not be clearly understood, we cannot understand the deep convective feedback effects upon the larger-scale environment in general. The latter has long been recognized as one of the most challenging and important research topics of atmospheric science. Since deep convective activities all over the world have features in common, an understanding of the Florida

convective-environmental interaction should provide some insight concerning deep convective/large-scale interrelationships in other places.

(2) One of the reasons that the summer Florida environment provides an excellent natural laboratory for investigating deep convective-environmental interactions is that there is typically a regular well-developed sea breeze circulation which produces cumulonimbus, without other large-scale disturbances. Because the sea breeze circulation provides regular forcing for convection to develop, a mesoscale investigation of the sea breeze-convective interaction should provide knowledge as to the deep cumulus convective effects on a larger scale atmospheric feature.

Because a meaningful study of the sea breeze-cumulonimbus interaction must cover the spatial and time scales of about 300 km x 300 km and ~12 hours, the current computational resource limitations generally exclude the use of cloud-scale explicit simulations such as those performed by Tripoli and Cotton (1980) or Tao and Simpson (1985). Therefore, to circumvent this computational resource problem, it is proposed in this study to utilize a convective parameterization approach. One advantage of using such an approach for the Florida investigation is that the upper troposphere (above about 5-6 km) is generally not perturbed by the sea breeze circulation without deep cumulonimbus convection. Therefore, the influence of deep cumulus convection in the middle and upper troposphere can be clearly distinguished from the shallow sea breeze circulation which occurs in the absence of deep cumulus clouds.

Before discussing the sea breeze-deep cumulus convective interactions, the model results of the moist sea breeze simulation (i.e., the control run) are first illustrated and validated by being compared with observations in Section 4-2. The observational data used for this purpose include a high-resolution manually digitized radar (MDR) composite analysis for Florida thunderstorms performed in Michaels et al. (1986), the surface radar rainfall observations made by Pielke and Cotton (1977) for July 17, 1973 over South Florida, and the satellite image composite analyses for several synoptically based categories made by McQueen and Pielke (1985). In Section 4-3, the deep convective effects upon the peninsula-scale surface divergence field will be discussed. In particular, the mechanism associated with surface cooling due to the downdraft effect upon the peninsula-scale environment will be described. The deep convective effects upon the peninsula-scale upper tropospheric environment are then discussed in Section 4-4. Attention is paid to the vertical solenoidal circulation patterns induced by the deep convective effects, and their close relationship with the boundary layer downdraft mechanism discussed in the Section 4-3.

## 4-2 The Moist Sea Breeze Simulation and Its Validation

The goal of the moist sea breeze simulations is to investigate the interrelationship between the sea breeze circulation and the evolution of deep cumulus convection. Once generated, deep cumulus convection constantly interacts with its mesoscale environment, thereby producing changes on the environmental flow as well as subsequent convective development. One particular deep convective-environmental interaction is focused on in this study–the surface divergence/convergence coupling

generated by the cooling associated with the deep convective downdrafts and the mesoscale surface flow. As will be illustrated in this section, this surface convergence is found to play an important role in enhancing and/or maintaining cumulonimbus convection of Florida, as well as producing feedback effects upon the larger scale environment.

Before illustrating the deep cumulus convective effects upon the Florida surface and upper tropospheric environment, the moist sea breeze simulation (hereafter referred to as the control run) is introduced and validated by being compared with observational analyses. The observational data used for this purpose include the following:

(a) a composite radar echo frequency analysis for a diurnal cycle (interval 3 hours) using data for the months May through August, 1963, performed by Frank, Moor and Fisher (1967);

(b) a high resolution radar statistical analysis performed by Michaels et al. (1986). A total of 10,000 hours of high resolution (47.6 x 47.6 $km^2$) manually digitized radar (MDR) data for June to August of 1972 to 1982 Florida thunderstorms (defined as a video integrator and processor (VIP) reflectivity of 3.0 or greater, Reap and Foster, 1979) were analyzed for the period;

(c) a composite satellite image analysis for different synoptic categories performed by McQueen and Pielke (1985). Included analyses for use in this section are the all-undisturbed days and the light southeasterly days during the afternoon (with an observation of interval 2 hours);

(d) hourly surface radar rainfall maps for July 17, 1973, documented in Pielke and Cotton (1977). The early morning

sounding of this day at Miami and the 0700 EST synoptic surface analysis was used for initiating the simulation (shown in Fig. 4-2-1a and b).

Model results chosen for the validation in this section include vertical velocities near 10 km and 1 km and model generated surface rainfall maps for the time period of 1 PM-5 PM at an interval of one hour. Vertical velocities are shown in units of cm/s, with a constant contour interval of 3 cm/s. Rainfall results shown are the convective rainfall rates (mm/10 hour) obtained from the parameterization and averaged in time over a 10 min period around the hour (the plotted magnitudes can be divided by 10 to be in the unit mm/hr).

4-2-(a) Results at 1 PM

Figure 4-2-2 shows the vertical velocity maps at 1 PM near 10 km (top) and 1 km (middle), as well as the rainfall rate map (bottom). We see that during synoptically undisturbed days with a low-level east-southeasterly wind as represented in this simulation, the southern tip of the Florida peninsula and its nearby southwest coastal area are associated with the earliest deep convection. The northwest coastal zone of the domain (slightly south of Tampa) is associated with a secondary peak of the deep cumulus convective activity at this time.

Figure 4-2-3 (reproduced from Frank, Moore and Fisher, 1967) shows that at 1 PM, the composite radar echo frequency distribution for the southern half of the peninsula has its major peak around the southern tip. Echos are also found to the southwest and southeast of Lake Okeechokee and the area between the lake and eastcoast. Smaller frequencies are also seen along the west coast between Fort Myers and Tampa. Figure 4-2-4(a) (reproduced from Michaels et al., 1986) shows

Figure 4-2-1(a). The early morning (07 EST) Miami sounding of July 17, 1973, which is used for initiating the moist sea breeze simulation (or the control run). The surface wind is seen in Fig. 4-2-1(b).

Figure 4-2-1(b). The synoptic-scale surface pressure pattern over Florida region at 7 AM, July 17, 1973. The surface wind (at a speed about 4 m/s; in the direction of east-southeasterly) is used for the surface wind initiation of the control run.

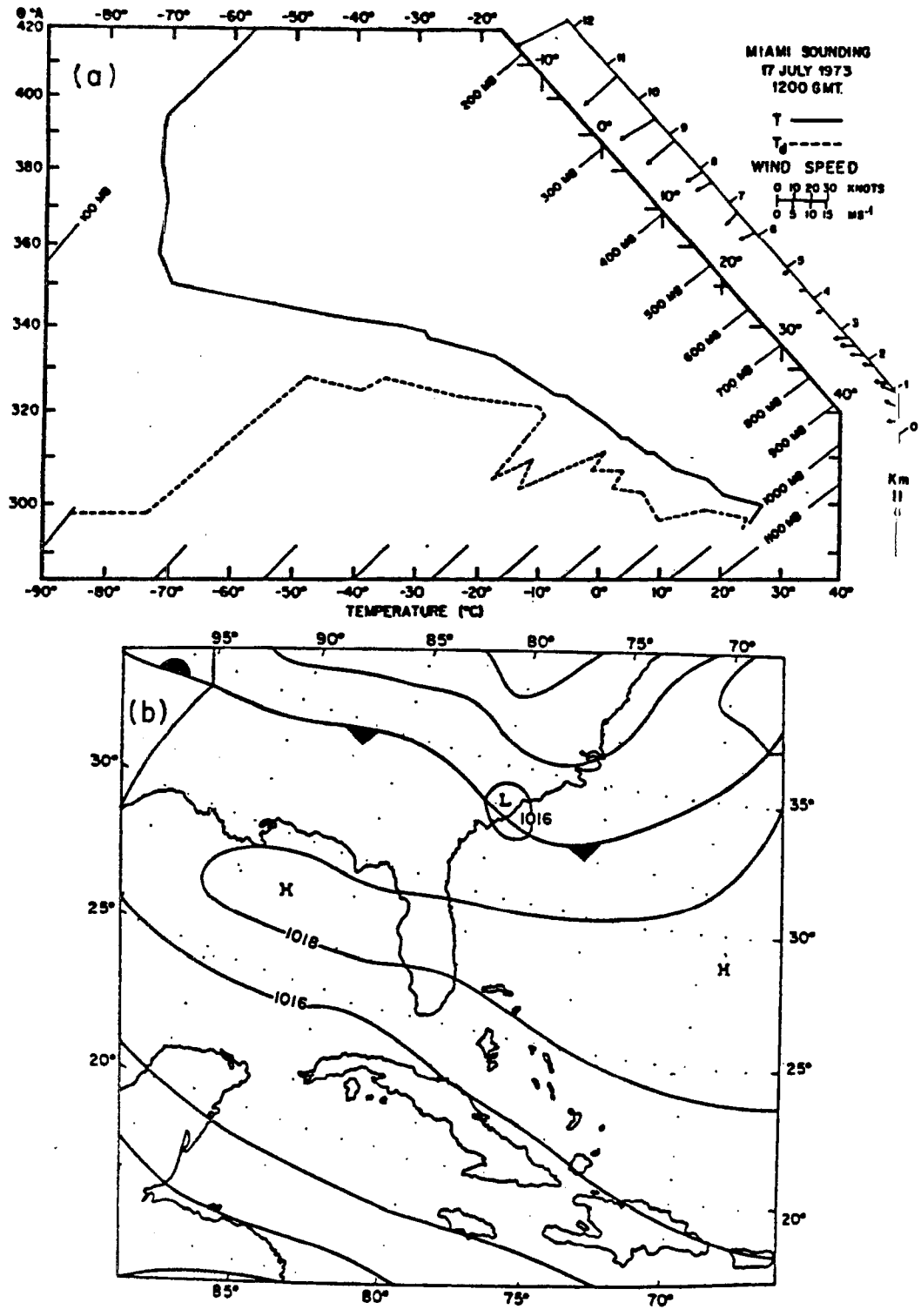
(a)
MIAMI SOUNDING
17 JULY 1973
1200 GMT.
T
$T_d$
WIND SPEED
0 10 20 30 KNOTS
0 5 10 15 ms⁻¹
θ °A
420
400
380
360
340
320
300
100 MB
200 MB
300 MB
400 MB
500 MB
600 MB
700 MB
800 MB
900 MB
1000 MB
1100 MB
-90° -80° -70° -60° -50° -40° -30 -20° -10° 0° 10° 20° 30° 40°
TEMPERATURE (°C)
Km
(b)
95° 90° 85° 80° 75° 70°
30°
25°
20°
35°
L
1016
H
1018
1016
H
85° 80° 75° 70°

Figure 4-2-2. The model produced horizontal maps of vertical velocity (cm/s) near 10 km (top) and 1 km (middle); and the model rainfall rate (mm/10 hour) (bottom), at 1 PM. The symbol "H" indicate upward motions, while "L" indicate downward motions. The contour interval for the velocities is 3 cm/s, and for the rainfall rates 2.2 mm/hour.

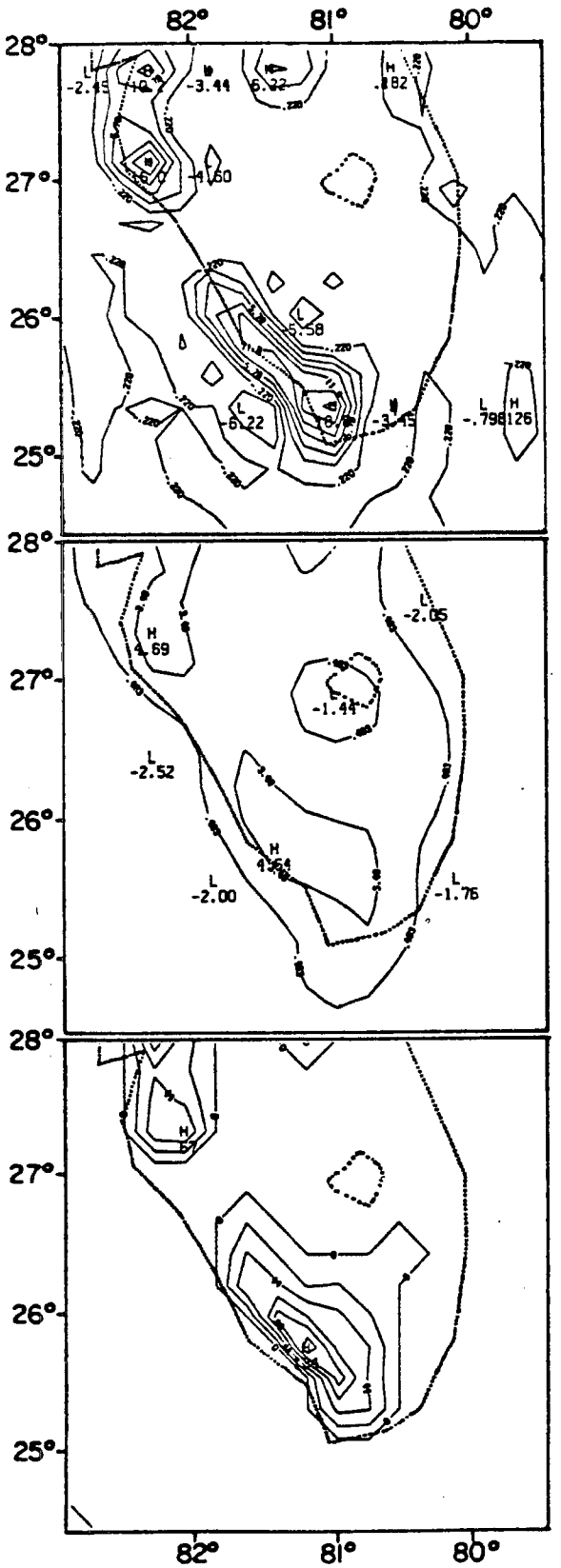
82°
81°
80°
28°
27°
26°
25°
Model Result
(1 PM)
W
(cm/s)
10 km
W
(cm/s)
1 km
Rain Rate
(mm/10hr)

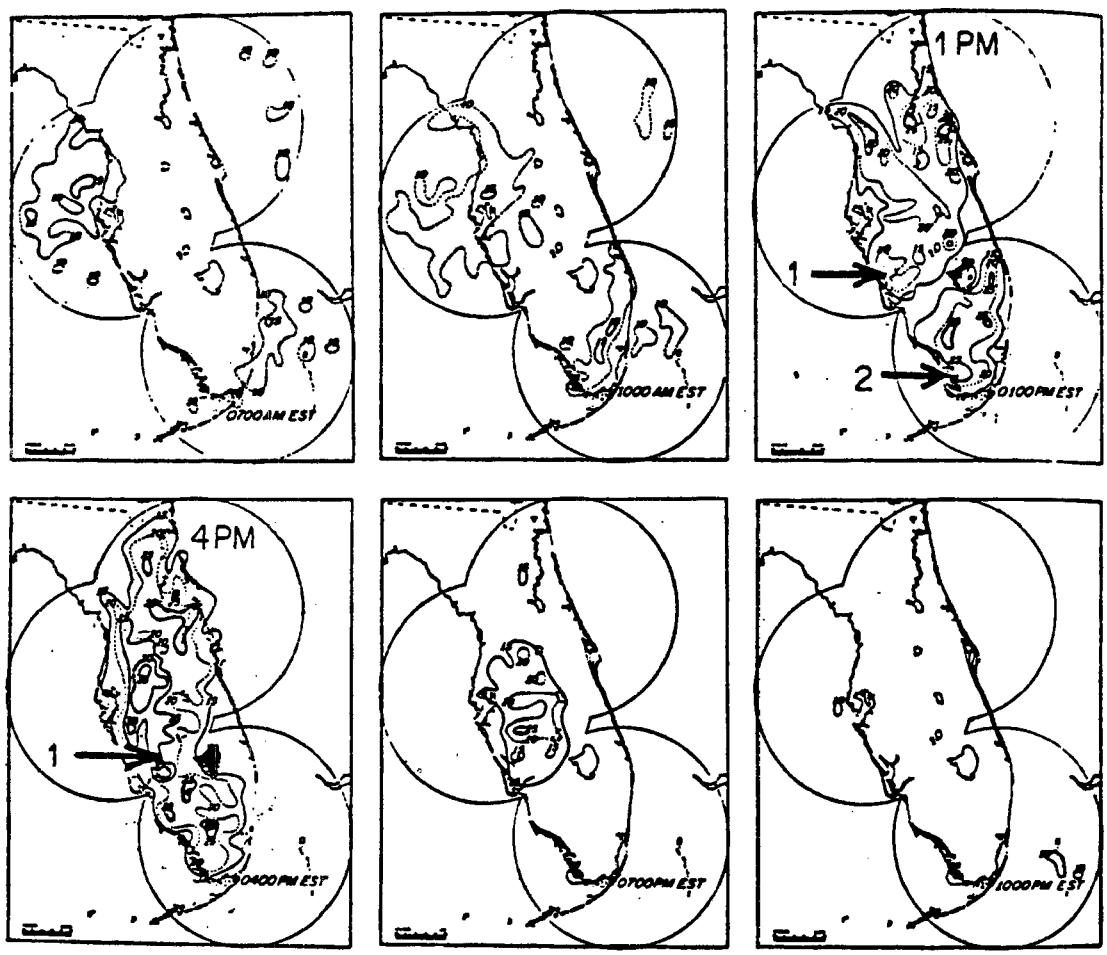


Figure 4-2-3. The seasonal diurnal cycle of echo frequencies over the Florida peninsula for the months May through August 1963 excluding the 0100 and 0400 charts. Frequency isolines have been drawn in 5 percent intervals beginning with the 10 percent line. Arrows "1" and "2" indicate the west coast convective systems discussed in section 4-2. (This figure is reproduced from Frank et al., 1967).

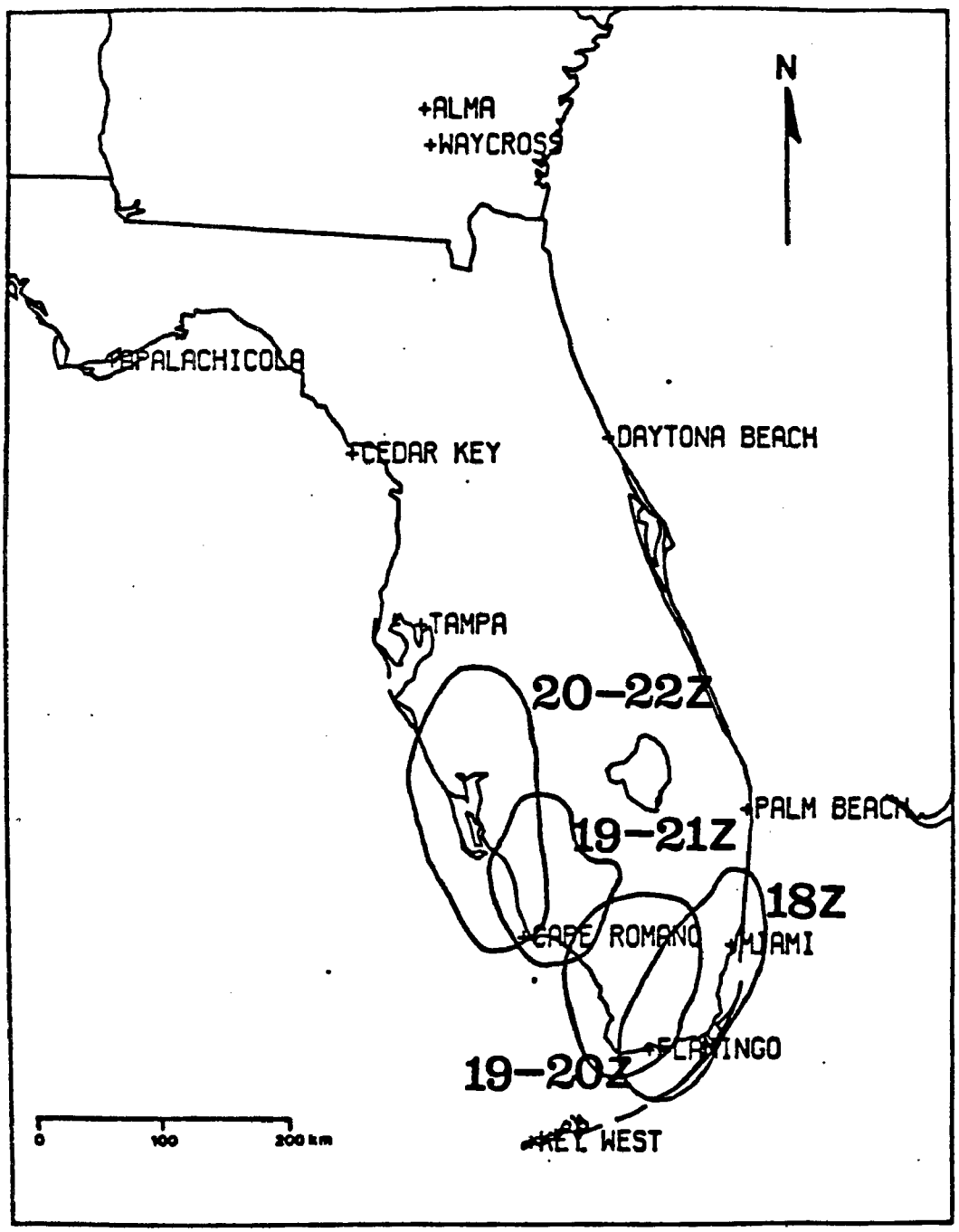


Figure 4-2-4(a). The northward marching of the statistically most favored locations of convective activities at the times during a day as indicated (from Michaels et al., 1986).

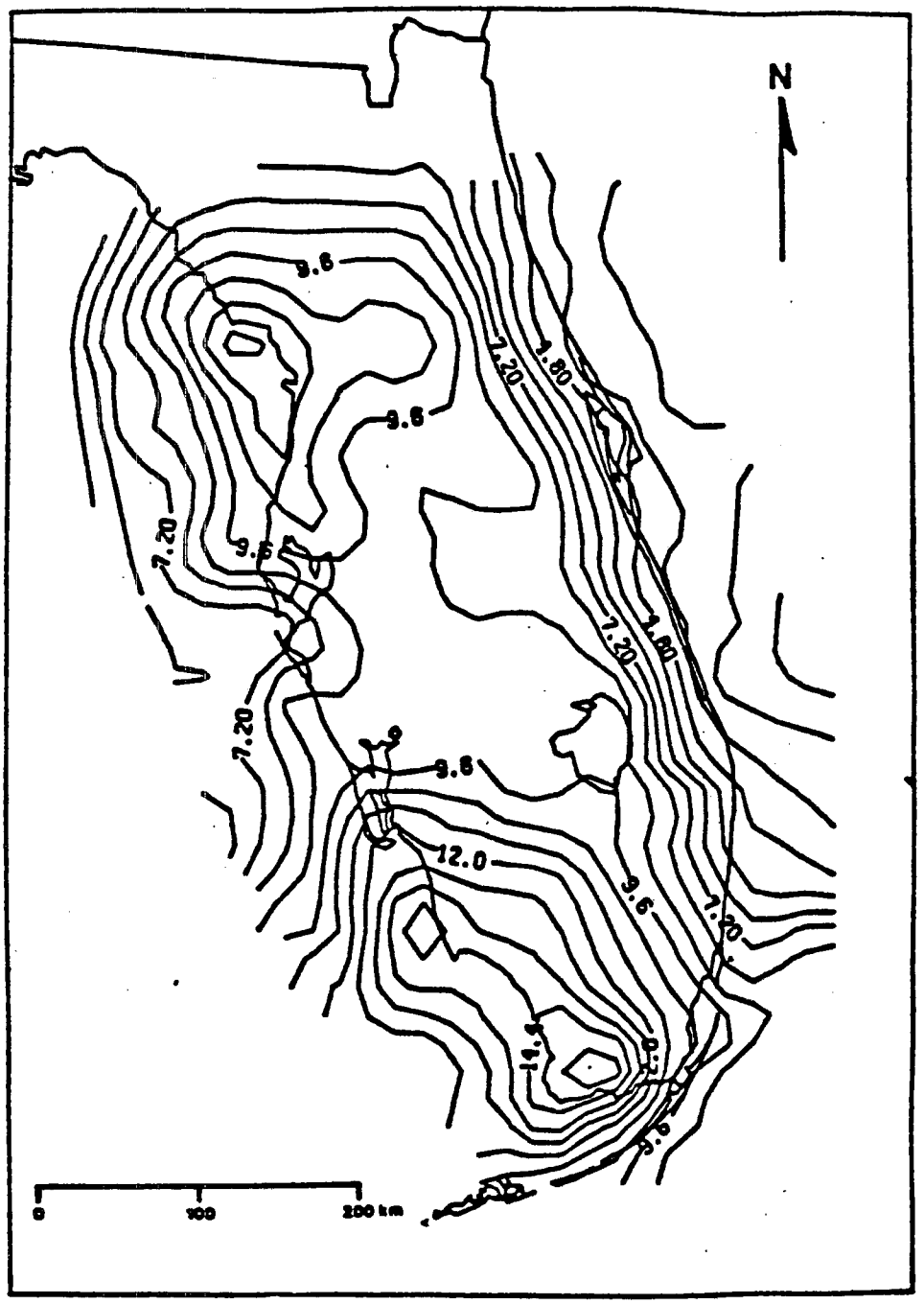


Figure 4-2-4(b). Mean percent of hours that a MDR VIP return of 3.0 or greater was observed (from Michaels et al., 1986).

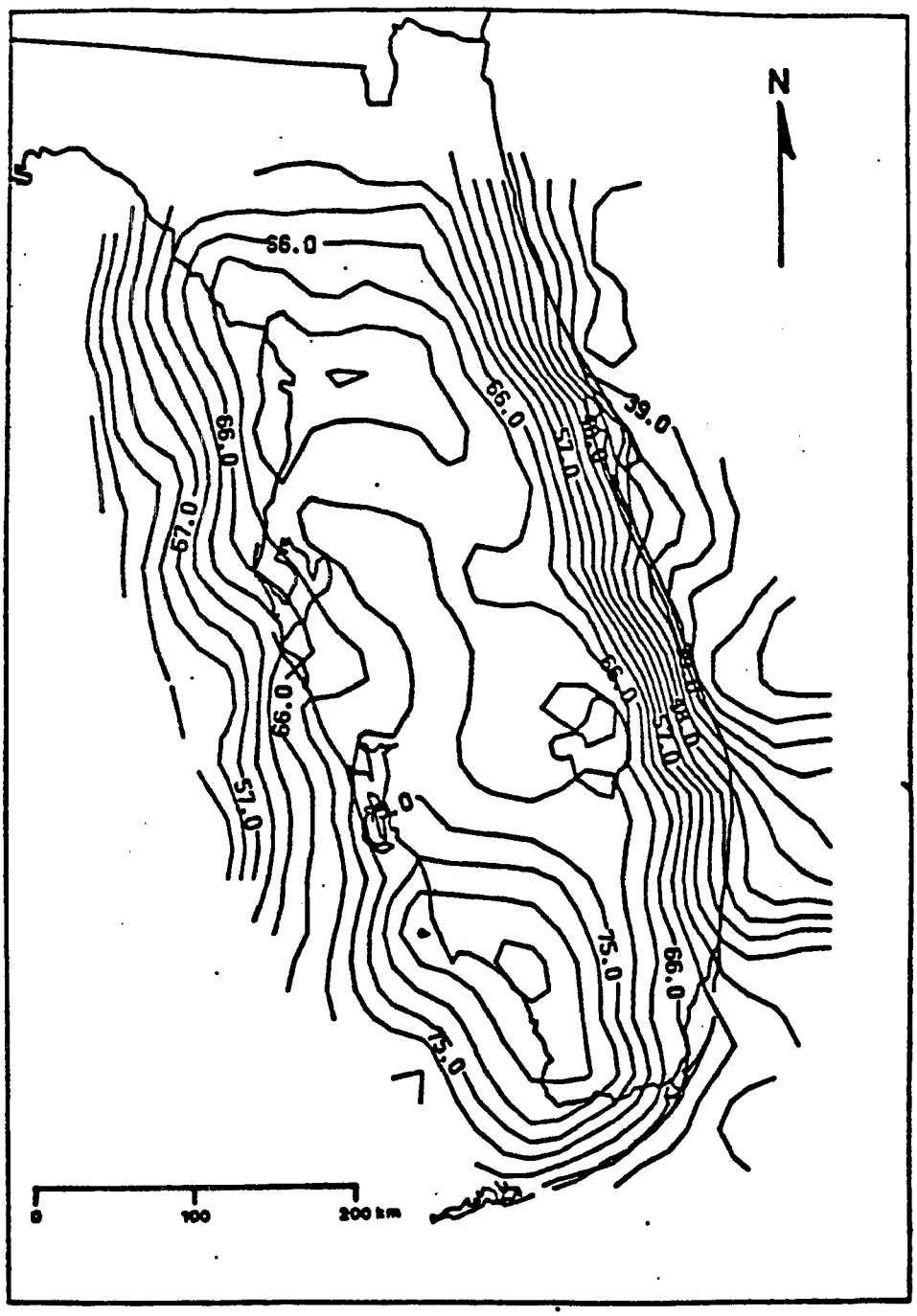


Figure 4-2-4(c). Mean percent of summer (June-August) days in which an MDR return of 3.0 or greater is observed (from Michaels et al., 1986).

that the diurnal March of the MDR VIP region starts from the southeast corner and the southern tip of the peninsula. Figure 4-2-4(b) and (c) (reproduced from Michaels et al., 1986) further show that the southern tip and the southwest coastal area are the statistically most favored locations for initiating Florida's summertime deep convection. Figure 4-2-5 shows the radar rainfall map at surface at 1 PM (July 17, 1973). As discussed in more detail in Pielke and Cotton (1977), the convective activities were seemingly associated with two elongated zones: one along the southwest coast and the other extended (NNE-SSW) from the eastside of Lake Okeechobee to the southwest corner of the peninsula.

Comparing the model results at 1 PM (Fig. 4-2-2) with the aforementioned observational analyses, we see that the model has simulated the precipitation zone around the southern tip and the nearby southwest coastal area. The rainfall observed (Fig. 4-2-5) to the east or immediate southeast of Lake Okeechobee is not simulated. The reason for this appears to be that using 22 km as the horizontal grid spacing, the lake effect is not well simulated; see the lack of significant low level vertical motion in this area in Fig. 4-2-2 (middle) (in Pielke, 1974 and Pielke and Mahrer, 1978, where substantial ascent was simulated in this area, 11 km was used as the grid spacing). The convective development along the upper west coast is associated with the sea breeze convergence zone generated by the model. This rain region corresponds to the local peak of radar echo statistics shown in Fig. 4-2-3 (indicated by arrow 1).

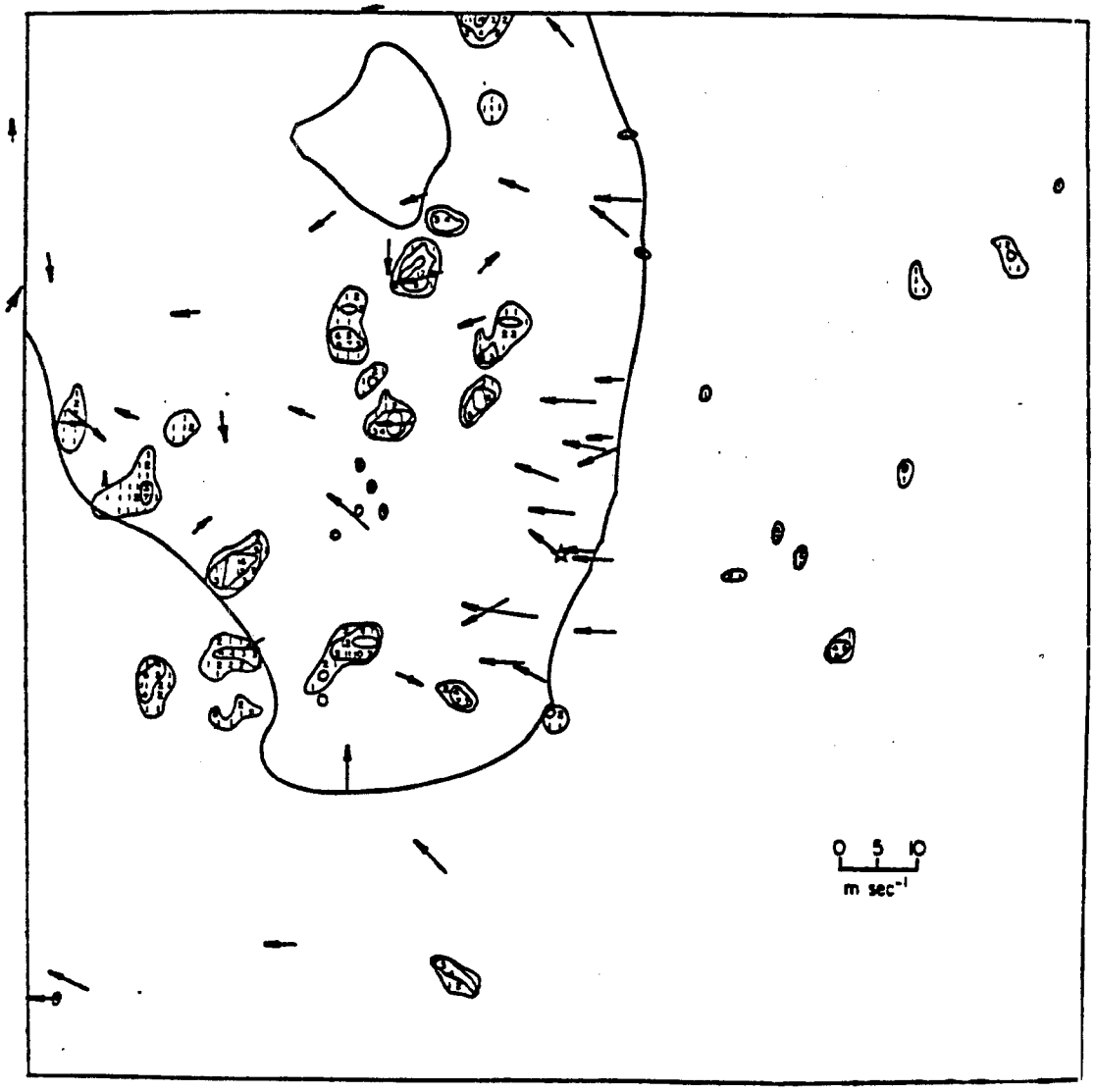


Figure 4-2-5. Surface radar rainfall map at 1300 EST over the southern Florida of July 17, 1973. Also included are the surface wind vectors (from Pielke and Cotton, 1977).

4-2-(b) Results at 2 PM

Figure 4-2-6 shows two peak areas of model rainfall are produced at 2 PM: one along the west coast to the north of the lake, and the other along the southwest coast. The rain area covers a large fraction over the western part of southern Florida.

Figure 4-2-7 (reproduced from McQueen and Pielke, 1985) shows the composite satellite images for deep convection (defined as cloud top temperatures <-38°C and visibly bright clouds) at 2 PM, under the light southeast (top) and strong southeast (bottom) synoptic categories. The strong southeast category was defined as an early morning surface geostrophic wind speed about 3.5 $ms^{-1}$ while the light southeast category included speeds between 1.0 and 3.5 $ms^{-1}$. From Fig. 4-2-7 it is evident that the speed of the synoptic prevailing wind normally produces rather significant differences in the deep convective cloud cover pattern at 2 PM. The cloud pattern of the light southeast category is chosen to compare with the model integration since the control run initialization is closer to that situation. We see clearly that at 2 PM climatologically likely location for deep convective development occurs along the west coast just south of Tampa; along the southwest coastal area; the southern tip of the peninsula; as well as north and east of Lake Okeechobee.

Figure 4-2-8 shows the radar rainfall along the southwest coast during the last hour. Surface outflow appears to be detectable from the measured winds along the west coastal region.

Comparing the model result (Fig. 4-2-6) with the observational analyses shown in Fig. 4-2-7(a), the climatologically preferred areas of deep cumulus convection except for the area over and east of the

Figure 4-2-6. The model produced horizontal maps of vertical velocity (cm/s) near 10 km (top) and 1 km (middle); and the model rainfall rate (mm/10 hour) (bottom), at 2 PM. The symbol "H" indicate upward motions, while "L" indicate downward motions. The contour interval for the veloities is 3 cm/s, and for the rainfall rates 2.2 mm/hour.

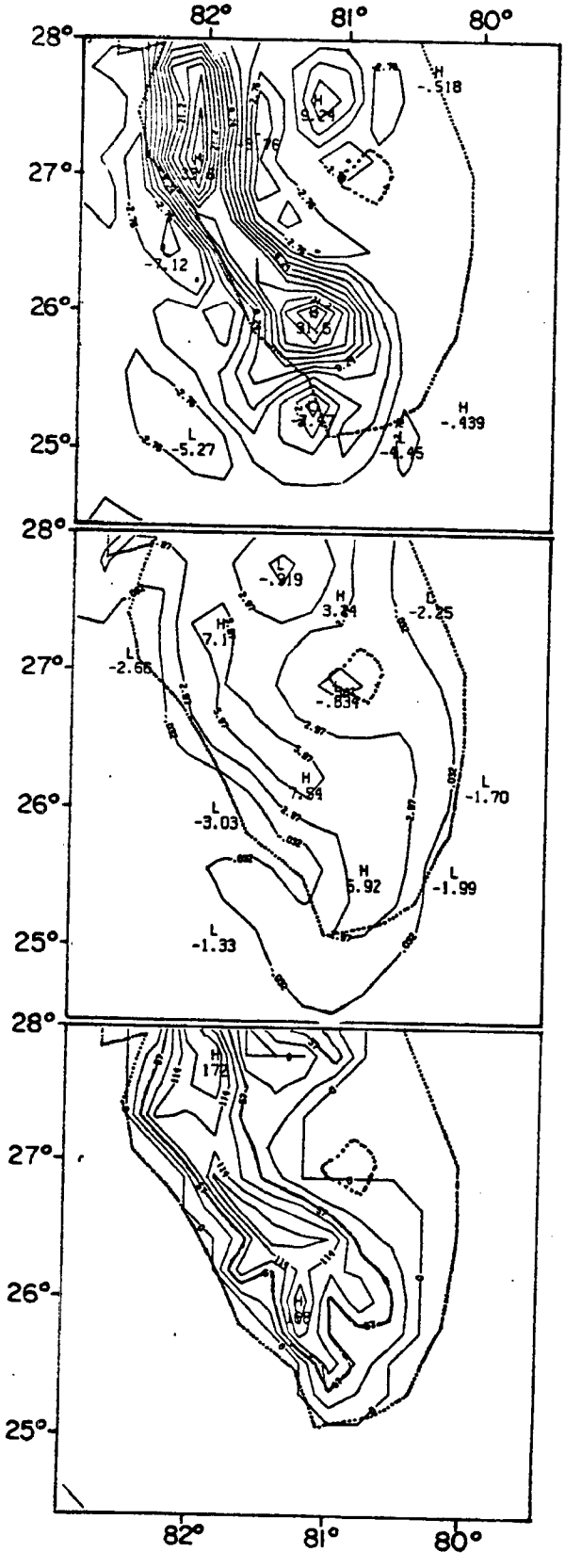
82°
81°
80°
28°
27°
26°
25°
Model Result
(2 PM)
W
(cm/s)
10 km
W
(cm/s)
1 km
Rain Rate
(mm/10hr)

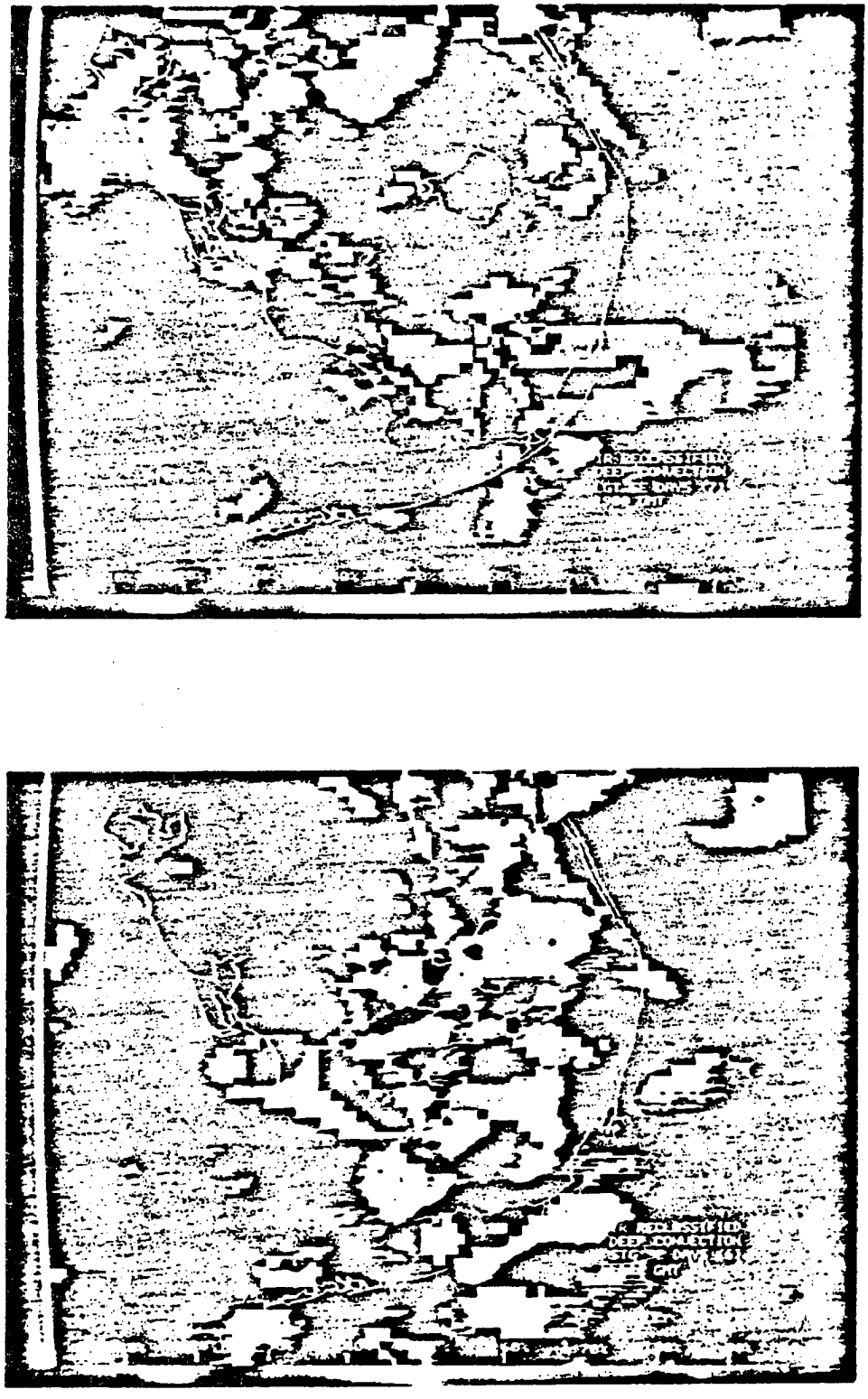

Figure 4-2-7. Satellite image composites by synoptic flow for (a) light southeast and (b) strong southeast synoptic classes at 1400 EST (from McQueen and Pielke, 1985).


Figure 4-2-8. Surface radar rainfall map at 1400 EST over the southern Florida of July 17, 1973. Also included are the surface wind vectors (from Pielke and Cotton, 1977).

lake generally occurs within the region of model predicted cumulonimbus convection. The agreement with the radar pattern on July 17 is not as good, although there appears to be a correlation between model predicted areas of highest convective activity and location of convective rain.

4-2-(c) Results at 3 PM

By 3 PM, the most significant development in the simulation is the generation of a new precipitation center (Fig. 4-2-9, bottom) which is stronger than the two nearby centers. The latter are associated with the two peaks shown in the previous hour's map (Fig. 4-2-6). This new activity has resulted from cooling by downdrafts (from the earlier two convective systems) which result in a horizontal pressure gradient and outflow from the older systems into a region in which the air was not yet modified by the downdraft cooling (this mechanism is discussed in more detail in section 4-3). The observed heaviest rainfall area along the west coast is slightly south, but close to the model predicted heaviest rainfall. The observed rainfall east of the lake, as described earlier, is not resolved in the model simulation because of the 22 km horizontal grid use.

Figure 4-2-10 shows a relatively larger convective system had formed by 3 PM near the southwest coast and to the east of Lake Okeechobee. From the surface flows indicated in Fig. 4-2-10, it appears that the west coast convective system is sustained by:

- the west coast and east coast sea breezes which had penetrated to the west coast region; and

Figure 4-2-9. The model produced horizontal maps of vertical velocity (cm/s) near 10 km (top) and 1 km (middle); and the model rainfall rate (mm/10 hour) (bottom),at 3 PM. The symbol "H" indicate upward motions, while "L" indicate downward motions. The contour interval for the velocities is 3 cm/s, and for the rainfall rates 2.2 mm/hour.

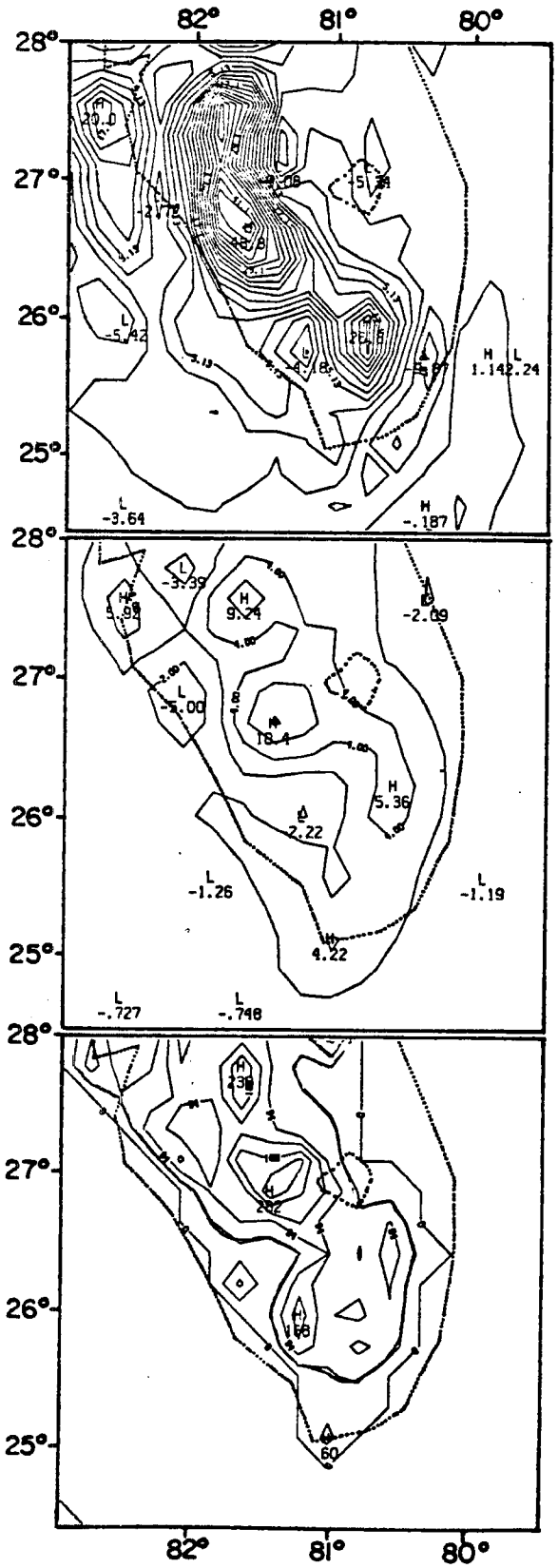
82°
81°
80°
28°
27°
26°
25°
Model Result
(3 PM)
W
(cm/s)
10 km
W
(cm/s)
1 km
Rain Rate
(mm/10hr)

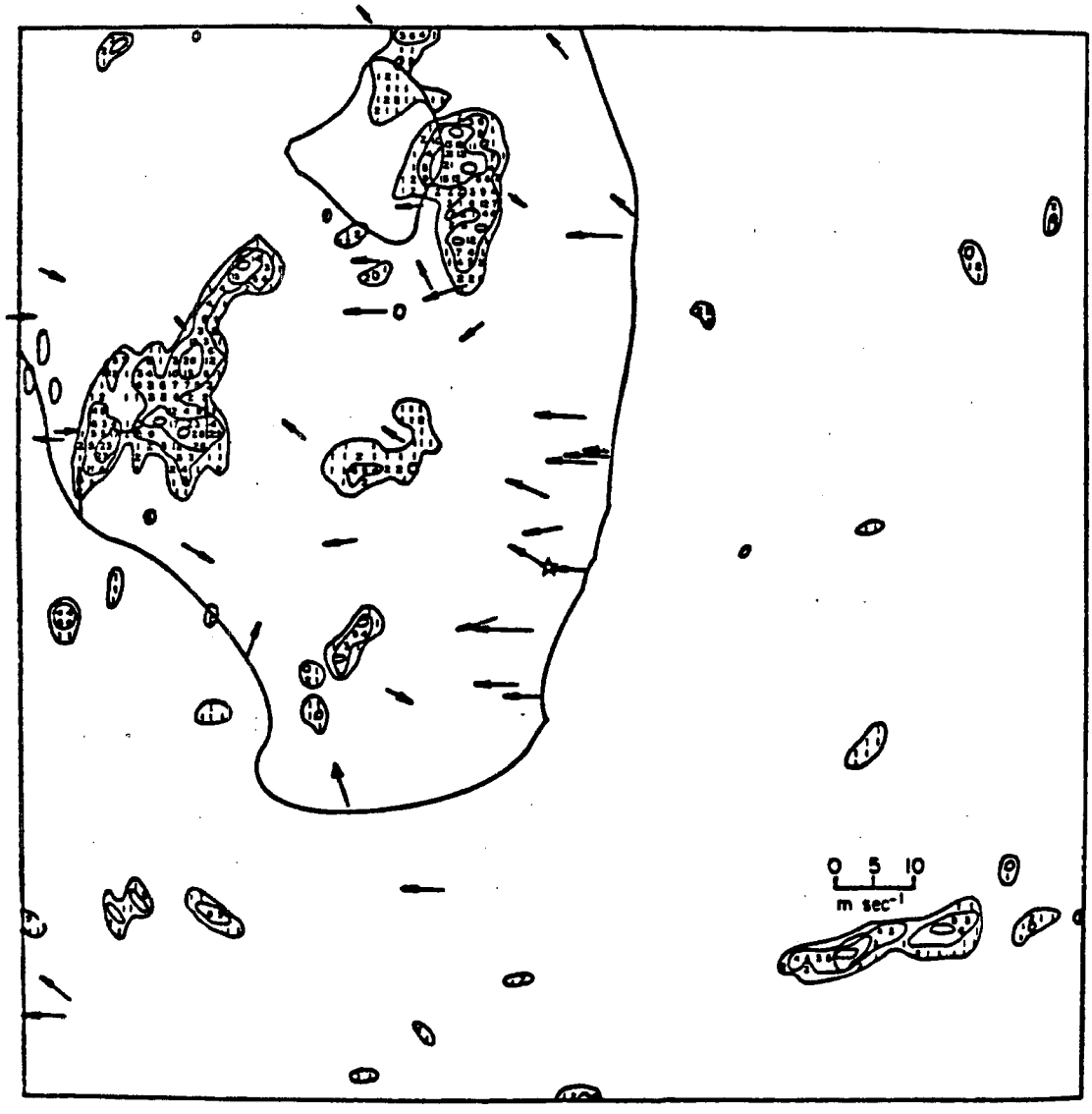


Figure 4-2-10. Surface radar rainfall map at 1500 EST over the southern Florida of July 17, 1973. Also included are the surface wind vectors (from Pielke and Cotton, 1977).

- convective surface outflow from nearby earlier deep convective systems to the northeast and to the southwest along the west coast.

Both of these mechanisms enhance low level convergence.

4-2-(d) Results at 4 PM

By 4 PM, Fig. 4-2-11 (top) shows that, due to surface downdraft cooling, the original sea breeze convergence zone has become associated with downward motion, while on its east and west sides upward motions are found. The simulated rainfall map at 4 PM (Fig. 4-2-11, bottom) shows that the peak rainfall is located just to the north of Lake Okeechobee, being associated with the original west coast convection. Two new rainfall peaks can be seen along the west coast: one to the southwest of the lake, and the other around Tampa.

The development of the west coast convection to the north of Lake Okeechobee during undisturbed days can be seen in the 1 PM and 4 PM figures of Fig. 4-2-3. It is seen that between the 1 PM and 4 PM composites the west coast convection (indicated by the arrows) is apparently able to develop such that the radar rainfall regions to the north and south of Lake Okeechobee are connected.

Figure 4-2-12 (top) shows that the most significant difference, as compared with the 2 PM composite (Fig. 4-2-7) during the afternoon for the light southeast category, is associated with the deep convective development to the west of Lake Okeechobee. This northward marching of the west coast convective systems is clearly seen from the MDR composite analysis shown in Fig. 4-2-4. While the statistically evident northward march is not seen on the July 17 rainfall map at 4 PM (Fig. 4-2-13), it is nevertheless seen (comparing Fig. 4-2-13 with

Figure 4-2-11. The model produced horizontal maps of vertical velocity (cm/s) near 10 km (top and 1 km (middle); and the model rainfall rate (mm/10 hour) (bottom), at 4 PM. The symbol "H" indicate upward motions, while "L" indicate downward motions. The contour interval for the velocities is 3 cm/s, and for the rainfall rates 2.2 mm/hour.

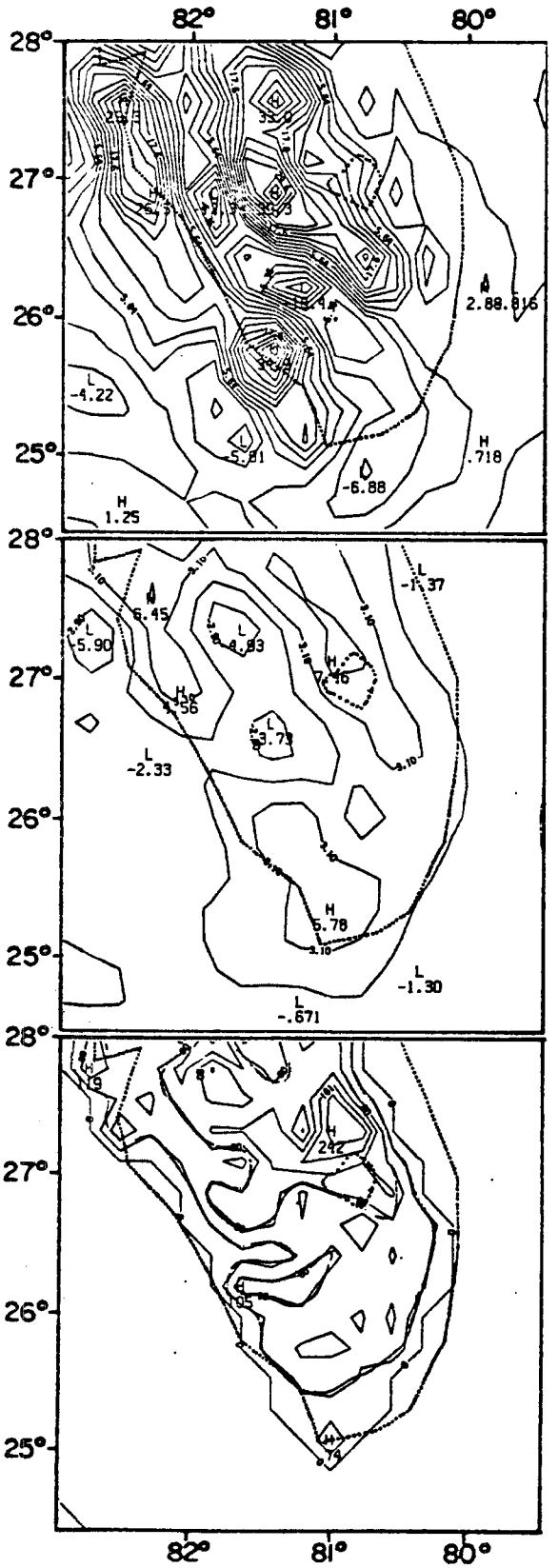
82°
81°
80°
28°
27°
26°
25°
Model Result
(4 PM)
W
(cm/s)
10 km
W
(cm/s)
1 km
Rain Rate
(mm/10hr)

Figure 4-2-12. Satellite image composites by synoptic flow for (a) light southeast and (b) strong southeast synoptic classes at 1600 EST (from McQueen and Pielke, 1985).

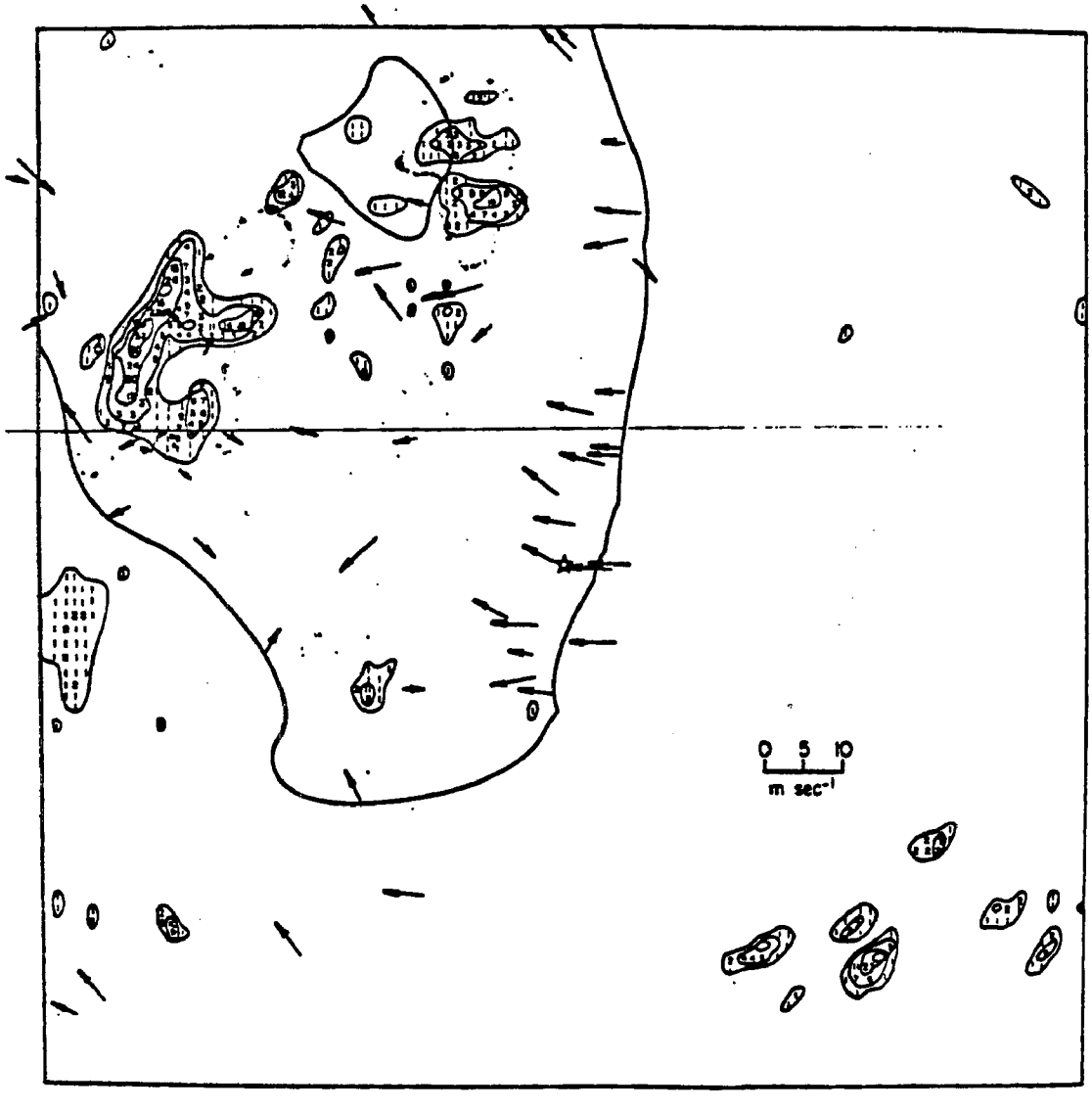


Figure 4-2-13. Surface radar rainfall map at 1600 EST over the southern Florida of July 17, 1973. Also included are the surface wind vectors (from Pielke and Cotton, 1977).

Fig. 4-2-10) that the southern part of the peninsula became essentially free of convection. The original tendency for elongated convective zones have become replaced by locally enhanced convective systems by 4 PM. This indicates the mature convective development is no longer within the original sea breeze convergence zones.

The model result at 4 PM has simulated the convective developments surrounding the area just to the west and south of Lake Okeechobee (comparing Fig. 4-2-11, top and bottom, with Fig. 4-2-12, top and Fig. 4-2-13). Also the relatively clear and rainfree areas around the southwest coast (Fig. 4-2-12, top, and Fig. 4-2-13) and around Fort Myers (Fig. 4-2-12, top) can be seen from the model result (Fig. 4-2-11, top and bottom).

4-2-(e) Results at 5 PM

Finally, the model result at 5 PM is shown in Fig. 4-2-14. We see that the basic pattern from the previous hour is retained except that the new convective development along the west coast has become rather significant at 5 PM. In the area between this new west coast convection and the (old) convection (which is to the north and south of the lake) we see a region of downward motion (Fig. 4-2-14, top). It'll be discussed in more detail in section 4-3 that the convective downdraft cooling at the surface is the hypothesized physical mechanism which produces the stabilized zone as well as the new convective developments surrounding this zone.

Figure 4-2-15 shows that the original convective area has diminished, and that there are new convective developments surrounding the earlier convective area by 5 PM. It appears that the original convective system produced surface outflows (see Fig. 4-2-13) due to

Figure 4-2-14. The model produced horizontal maps of vertical velocity (cm/s) near 10 km (top) and 1 km (middle); and the model raifall rate (mm/10 hour) (bottom), at 5 PM. The symbol "H" indicate upward motions, while "L" indicate downward motions. The contour interval for the velocities is 3 cm/s, and for the rainfall rates 2.2 mm/hour.

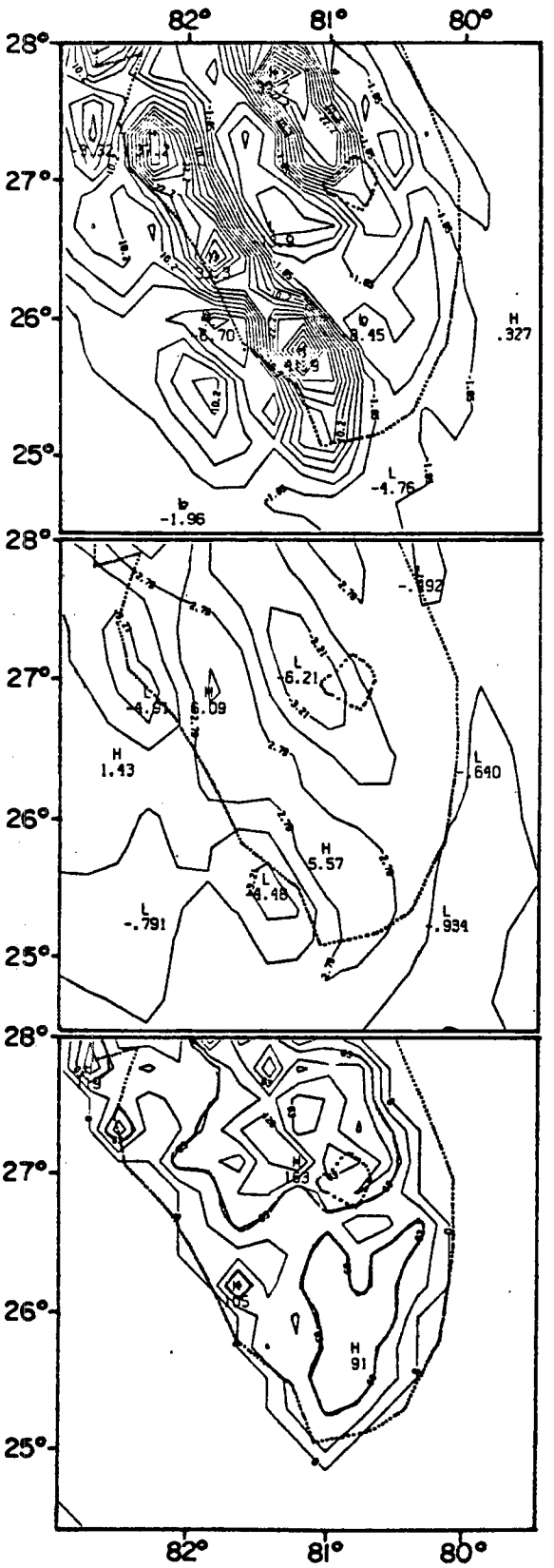
82°
81°
80°
28°
27°
26°
25°
Model Result
( 5 PM)
W
(cm/s)
10 km
W
(cm/s)
1 km
Rain Rate
(mm/10hr)


Figure 4-2-15. Surface radar rainfall map of 1700 EST over the southern Florida of July 17, 1973. Also included are the surface wind vectors (from Pielke and Cotton, 1977).

downdraft cooling which produced low-level convergence around its periphery and resultant new shower development. The remnants of the east and west coast sea breezes enhanced the low-level convergence by 5 PM. This analysis suggests that the Florida summer deep cumulus convection substantially interacts with the sea breeze circulation through the surface cooling effect due to convective downdrafts.

## 4-3 Deep Cumulus Convective Effects Upon the Peninsula-Scale Surface Convergence

A dry sea breeze simulation is made which is otherwise exactly the same as the moist sea breeze simulation presented in Section 4-2 (the control run) except that no convective parameterization is included.

By subtracting the results of the dry sea breeze simulation from that of the control run, we obtain the deep cumulus convective effects upon the mesoscale environment. The differences between the two simulations indicate the mesoscale responses due to the convective forcing. In the following figures, "total" refers to the result of the control run, while "total-dry" refers to the results when the dry solution is subtracted from the control integration.

Figure 4-3-1 shows the divergence at 9 m at 1 PM for the control run (top) and for the pure convective effect at the same time (bottom). Figure 4-3-1 (top) shows that the well developed west coast sea breeze convergence zone has a peak value of about $-1.0 \times 10^{-4}$ $s^{-1}$. Surface convergence occurs throughout the peninsula except Lake Okeechobee, while surface divergence occurs over the surrounding water, with larger values just off the west coast. Since at this time the deep convective feedbacks upon its environment are not yet significant, the west coast convergence zone represents the sea breeze forcing for initiating deep convection. Figure 4-3-1 (bottom) illustrates that the deep convection

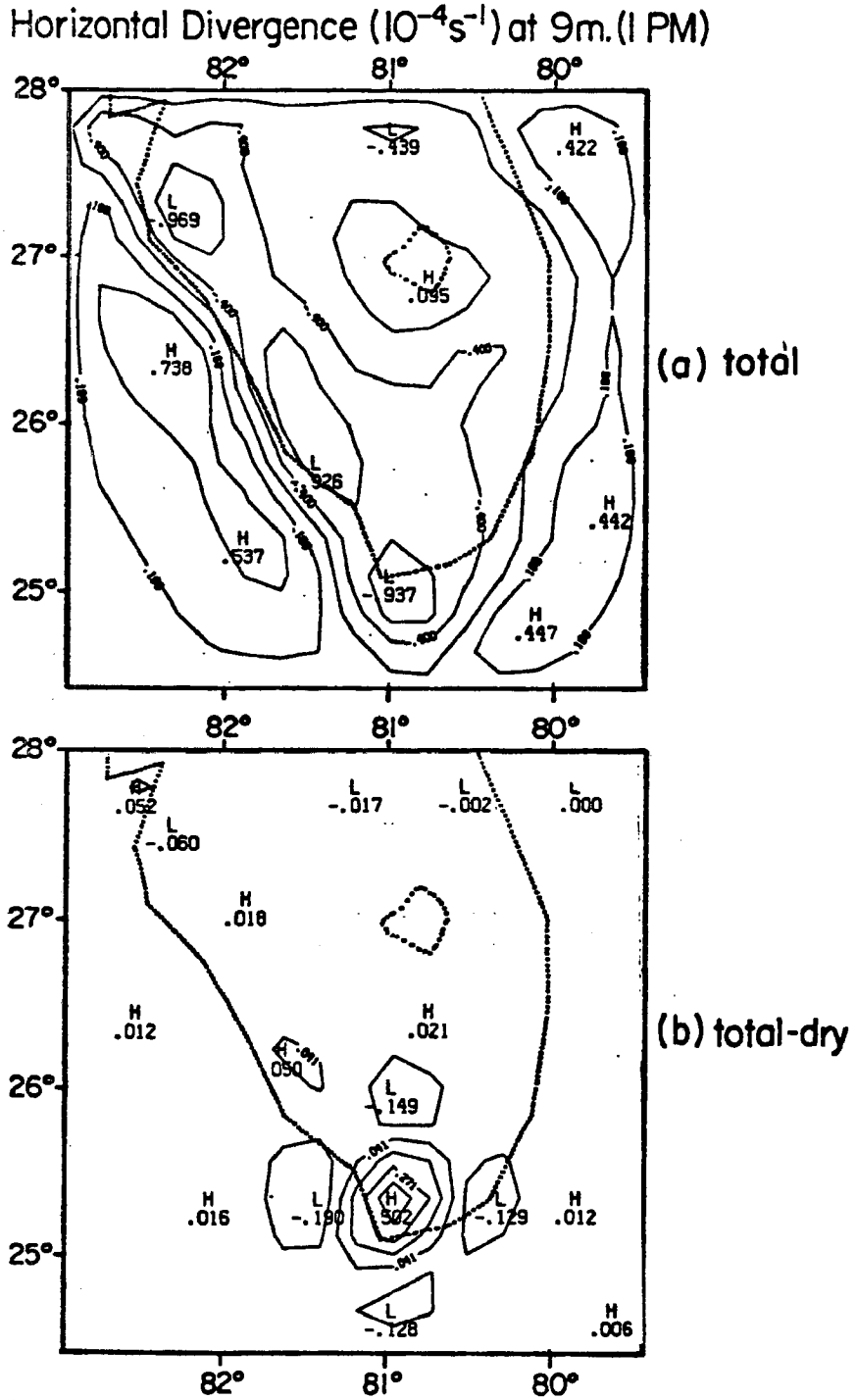


Figure 4-3-1. Horizontal distributions at 9 m of model produced horizontal divergences at 1 PM ($10^{-4}$ $s^{-1}$), from the control run (indicated as "total") (top); and from the difference by subtracting a dry run result from the control run result (indicated as "total-dry") (bottom). "H" indicates divergence center and "L" indicates convergence center.

is producing a dramatically different surface divergence pattern. The deep convection contributes surface divergence surrounded by a convergence contribution around the southern tip of the peninsula. This enhanced surface convergence surrounding the deep convection results from low-level wind acceleration out from the downdraft cooled boundary layer air toward the areas with unmodified warmer boundary layer air.

The convective induced horizontal divergence at 9 m is in response to the convective induced boundary layer cooling at 9 m (Fig. 4-3-2(a)) and the resultant horizontal winds (consider only the east-west component for simplicity) at 9 m (Fig. 4-3-2(b)). That is, the deep cumulus convection produces surface cooling due to downdrafts over the convective area (which is around the southern tip of the peninsula and the nearby southwest coast, by 1 PM). This surface cooling generates localized high pressure (a "mesohigh" at the surface), which produces localized surface divergence (Fig. 4-3-1, bottom) with surface convergence where the outflow from the cooled air meets an opposing sea breeze and synoptic wind flow.

By 2 PM, Fig. 4-3-3 shows that deep convective systems have developed along the southwest coastal area and in the northwest of the domain (near Tampa). The surface divergence region produced by downdraft cooling is enlarged and enhanced. Relatively larger surface convergence areas (Fig. 4-3-3, top) are produced which surround the main divergence areas (Fig. 4-3-3, bottom). Since the convergence zone tends to provide a favorable environment for deep convection to develop, it is clear that the development of cool boundary layer pockets by the deep cumulus downdrafts is an important forcing mechanism which organizes deep convection on the mesoscale (Byers and Braham, 1984; Simpson

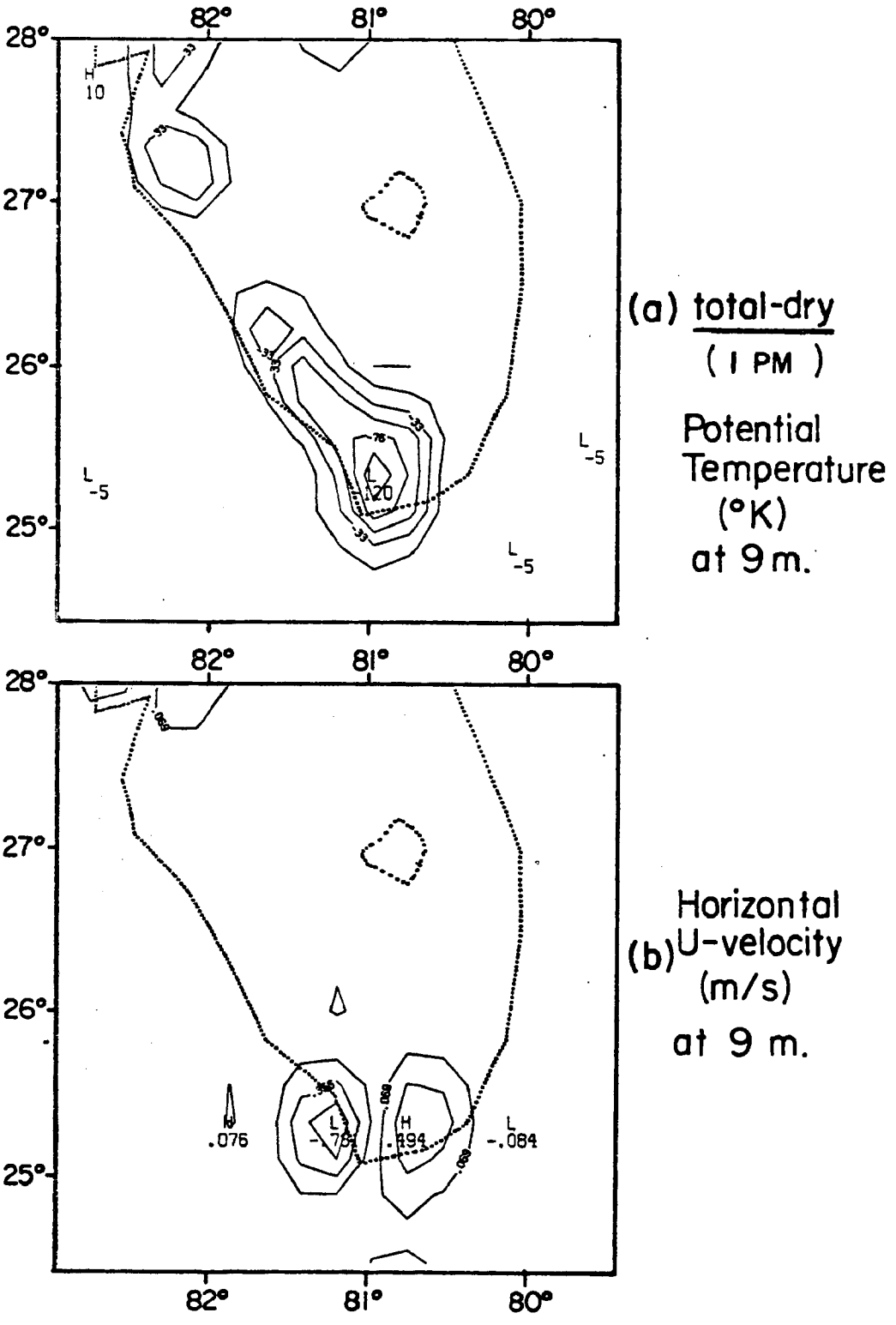


Figure 4-3-2. The "total-dry" quantities at 9 m at 1 PM, including (a) potential temperature (note magnitudes are scaled by 100) and (b) horizontal u-velocity (m/s).

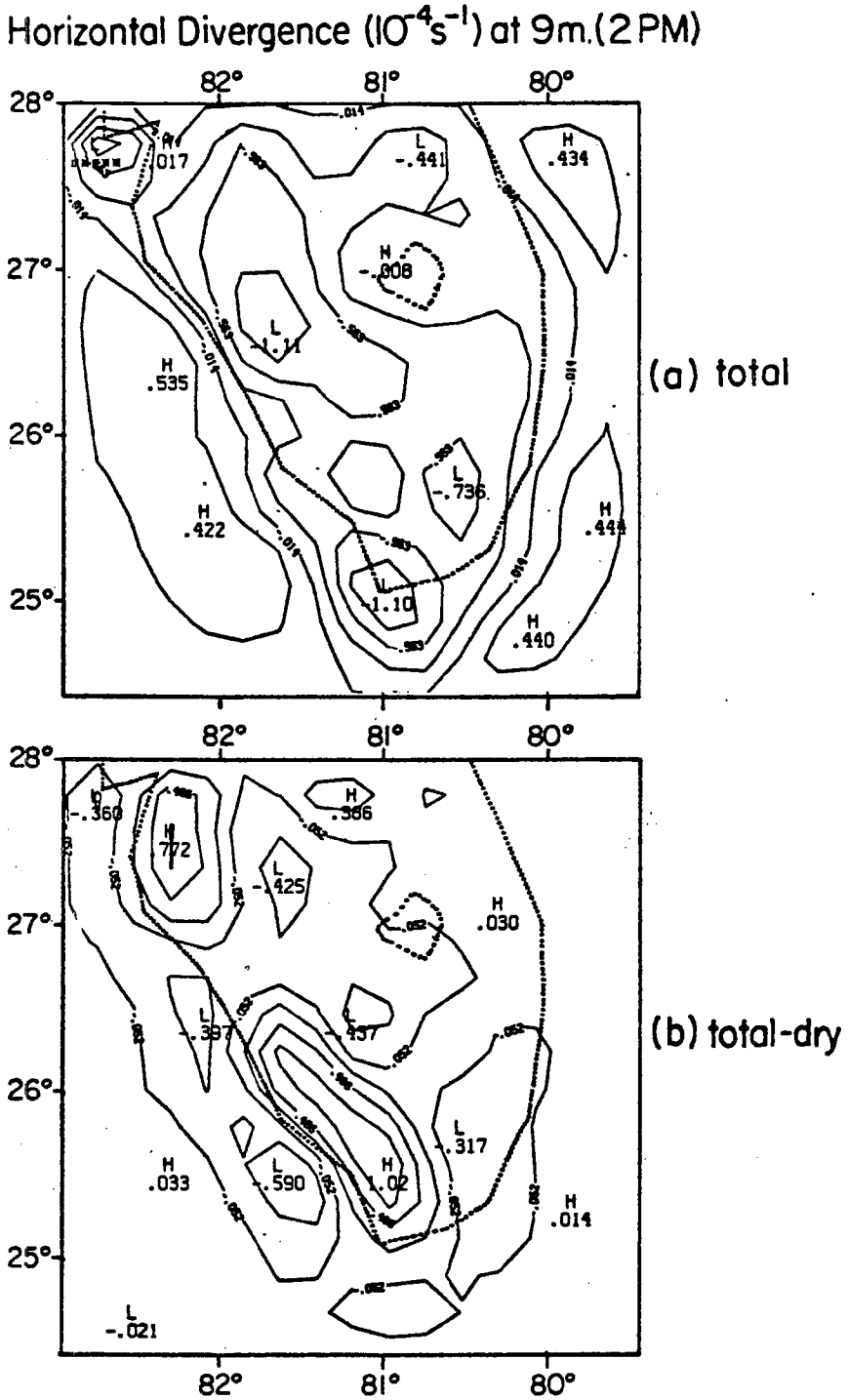


Figure 4-3-3. Horizontal distribution at 9 m of model produced horizontal divergences at 2 PM ($10^{-4}$ $s^{-1}$) from the control run (indicated as "total") (top); and from the difference by subtracting a dry run result from the control run result (indicated as "total-dry") (bottom). "H" indicates divergence center and "L" indicates convergence center.

et al., 1980). The enlarged surface cooling is clearly seen in Fig. 4-3-4 (top). This cooling generates horizontal flows at 9 m (Fig. 4-3-4, bottom).

By 3 PM, Fig. 4-3-5 shows that due to the downdraft cooling, a continuous zone with deep cumulus convection (indicated by the surface divergence) is formed. Comparing Fig. 4-3-5 (top) with Fig. 4-3-1 (top), we see that the mesoscale surface convergence pattern originally produced by the sea breeze circulation has been significantly changed. The downdraft-produced surface divergence is now as large as the original mesoscale convergence (the convective-produced divergence reaches a peak value of $1.1 \times 10^{-4}$ $s^{-1}$). Figure 4-3-6(a) and (b) show that the two originally separated convective systems have merged to form a continuous system along the original sea breeze convergence zone. Surface convergence areas are now found on both sides of the divergence zone. In particular, we see from Fig. 4-3-5 that a new convergence area formed just to the west of Lake Okeechokee, which is apparently produced due to the surface divergent flow from the west coast convective system and the sea breeze (easterly) flow. It will be seen for the chosen XZ cross section discussed later in this chapter that this convergence produces the mesoscale low-level upwind-side upward motion which is associated with the important lower tropospheric moistening. Figure 4-3-7 and Fig. 4-3-8 show that by 4 PM, the west coast convective system has developed/propagated to the new convergence area shown above, thereby producing enlarged surface cooling and divergence over the peninsula.

This discussion of the mesoscale response due to cumulonimbus convection indicates that the model result is consistent with climatological observations in two aspects:

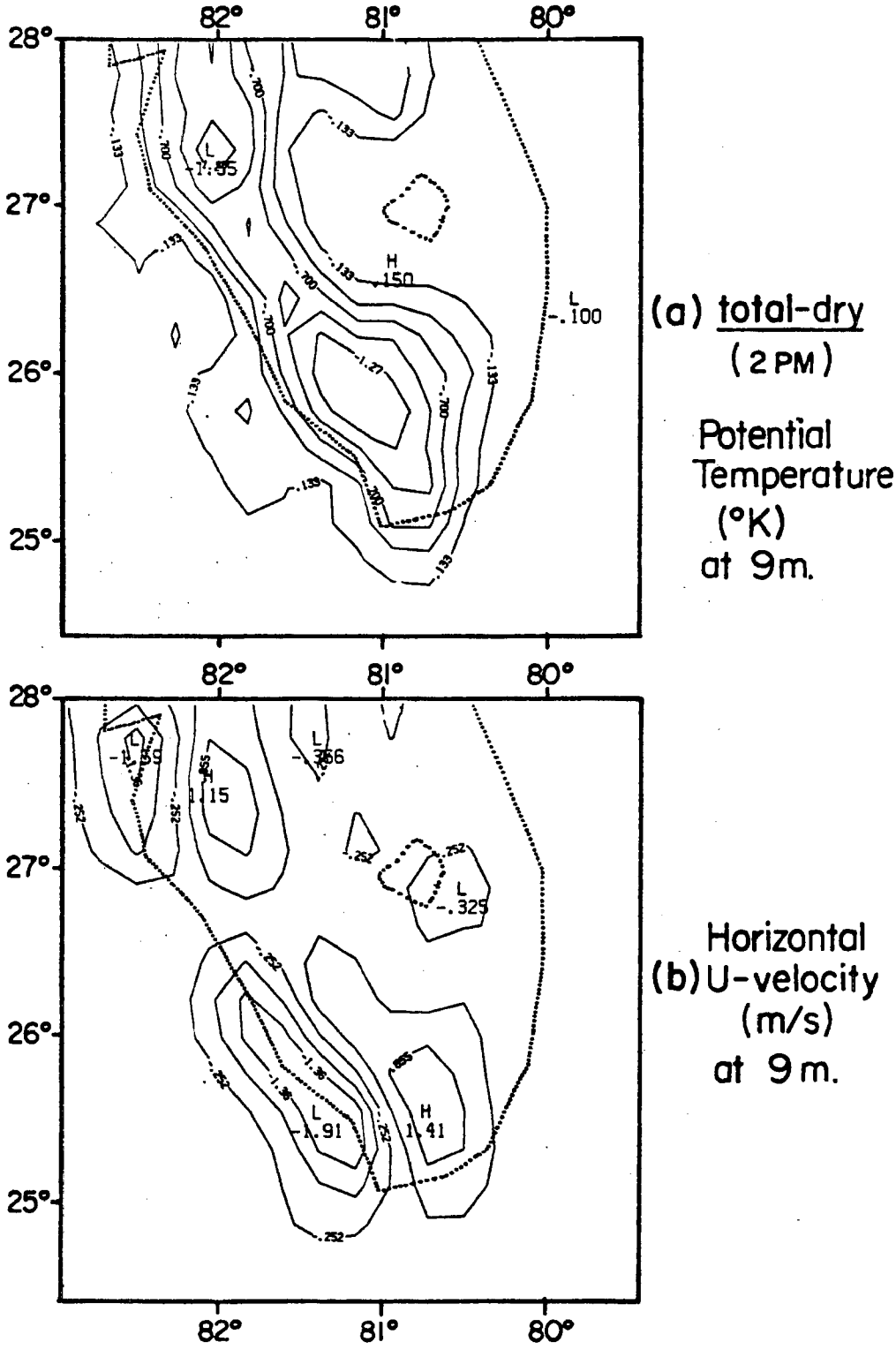


Figure 4-3-4. The "total-dry" quantities at 9 m at 2 PM, including (a) potential temperature (note magnitudes are scaled by 100) and (b) horizontal u-velocity (m/s).

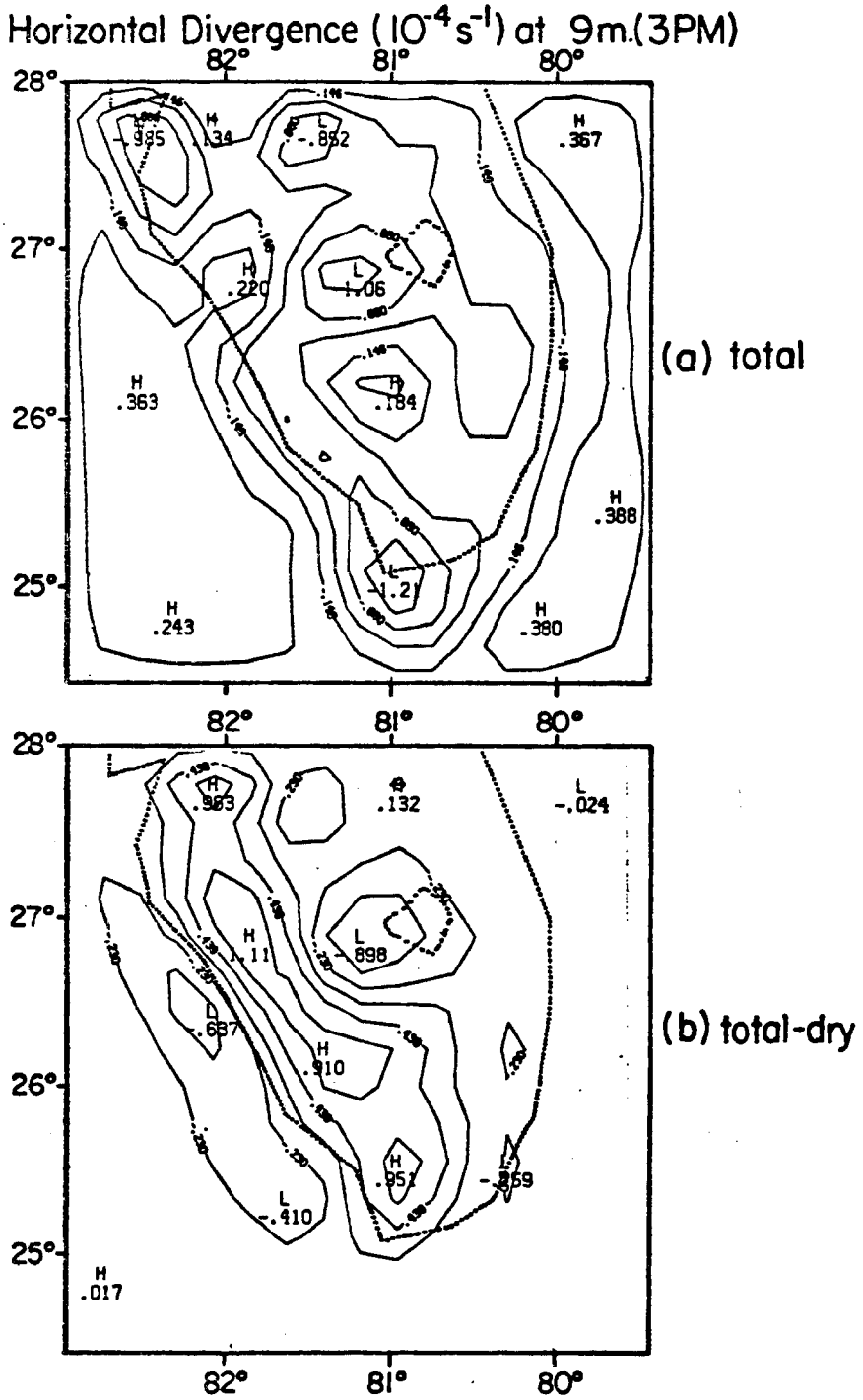


Figure 4-3-5. Horizontal distributions at 9 m of model produced horizontal divergences at 3 PM ($10^{-4}$ $s^{-1}$) from the control run (indicated as "total") (top); and from the difference by subtracting a dry run result from the control run result (indicated as "total-dry") (bottom). "H" indicates divergence center and "L" indicates convergence center.

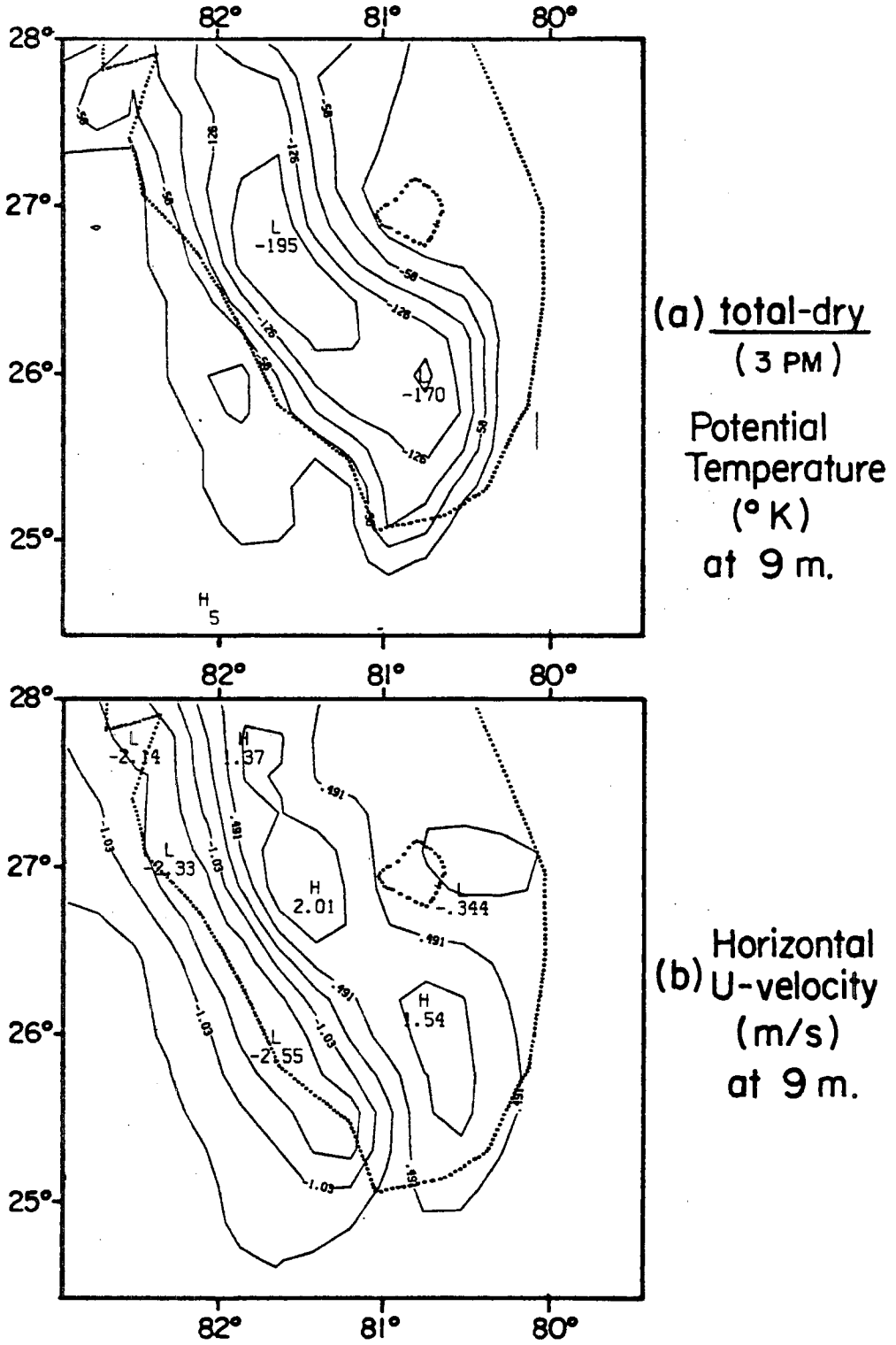


Figure 4-3-6. The "total-dry" quantities at 9 m at 3 PM, including (a) potential temperature (note magnitudes are scaled by 100) and (b) horizontal u-velocity (m/s).

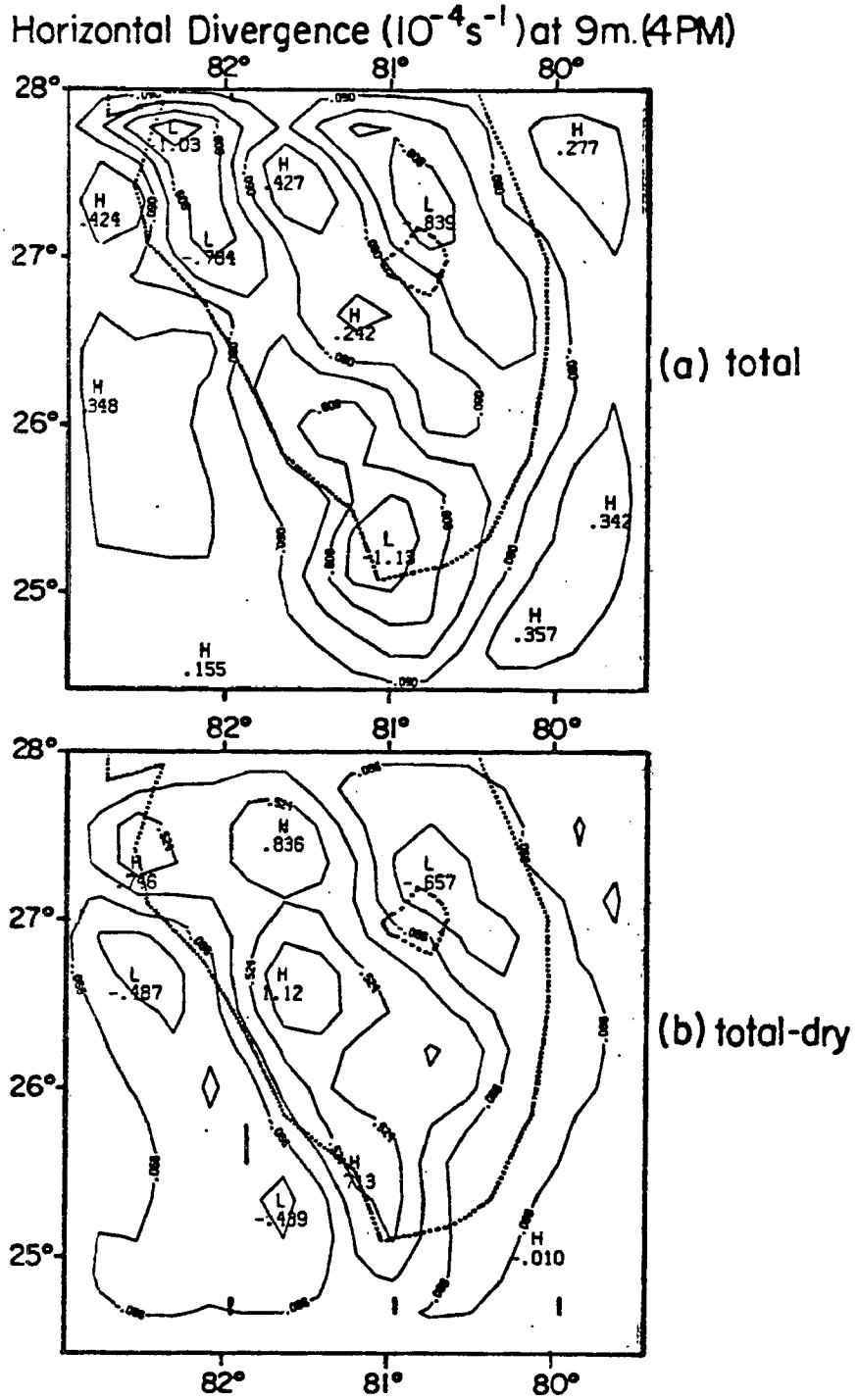


Figure 4-3-7. Horizontal distributions at 9 m of model produced horizontal divergences at 4 PM ($10^{-4}$ $s^{-1}$) from the control run (indicated as "total") (top); and from the difference by subtracting a dry run result from the control run result (indicated as "total-dry") (bottom). "H" indicates divergence center and "L" indicates convergence center.

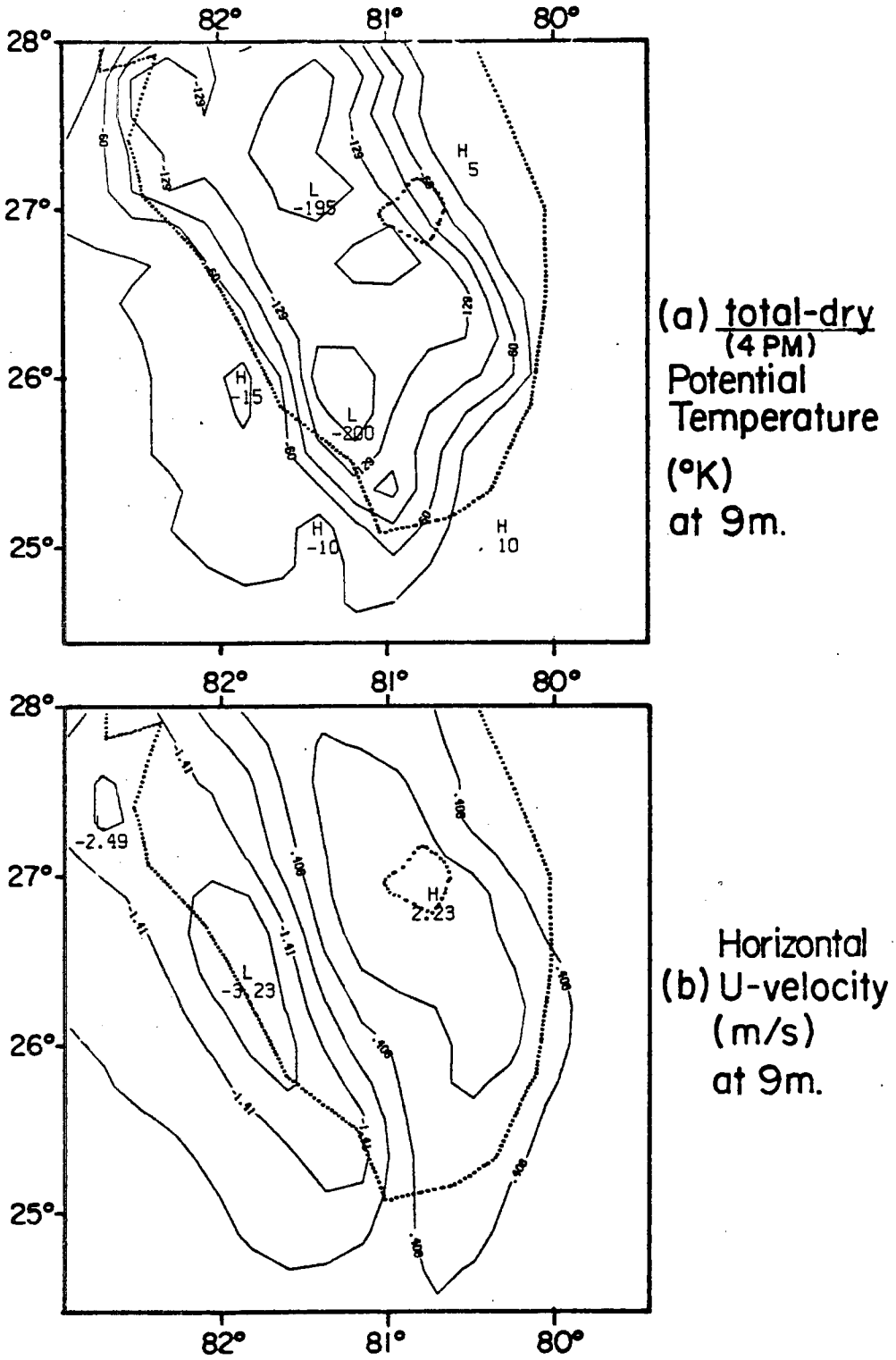


Figure 4-3-8. The "total-dry" quantities at 9 m at 4 PM, including (a) potential temperature (note magnitudes are scaled by 100) and (b) horizontal u-velocity (m/s).

(1) The deep convective area (Fig. 4-3-5, bottom) matches well with the original sea breeze convergence zone (Fig. 4-3-1, top), suggesting clearly that the sea breeze provides the necessary favorable preconditioned environment for deep convection to grow (Pielke, 1978; Lopze et al., 1984a,b).

(2) The peninsular or mesoscale surface divergence pattern can be rather significantly modified on the local areas due to deep convective downdrafts (Cooper et al., 1982).

The enrichment of the atmosphere by sea breeze flow and by motion which occurs because of deep convection is clearly seen in Fig. 4-3-9. Figure 4-3-9 shows the vertical moisture fluxes by the grid-scale motion from the control run at 3 PM and 4 PM. Before about local noon, the moisture fluxes are closely related to the vertical motions of the sea breeze circulation. When the west coast deep convection developed, however, in addition to the upper tropospheric moistening due to the convection, a particularly important lower and middle tropospheric moistening is generated due to the low-level upwind-side upward motion. The system is clearly seen to develop into a stronger intensity (as seen in Section 4-2) and to propagate toward the low-level upwind-side upward motion location. Thus, the Florida deep convective downdraft is found to play an important role in determining subsequent cumulonimbus intensity and location of preferential development as well as substantially modify the dry sea breeze environment in the later afternoon.

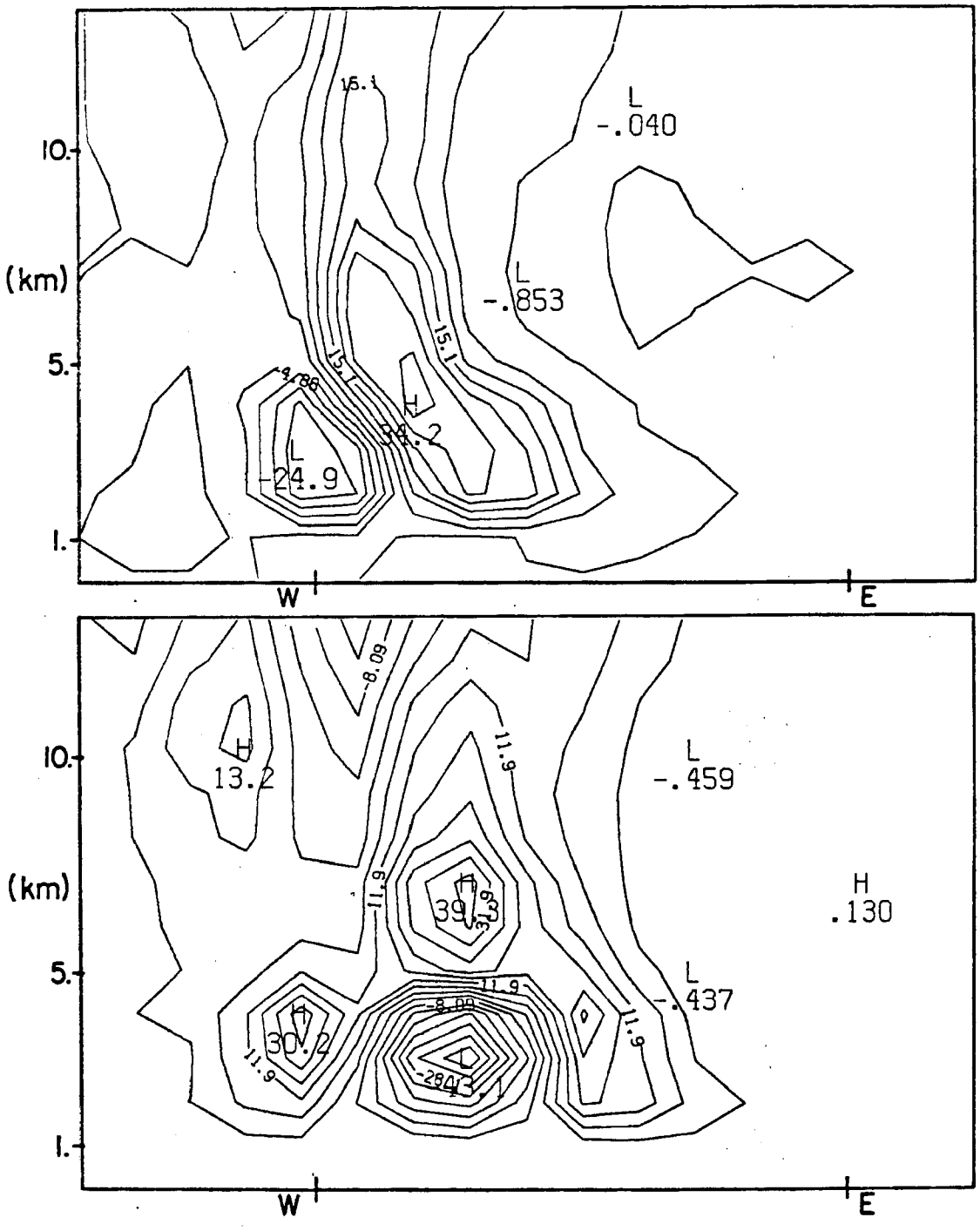


Figure 4-3-9. Vertical grid-scale moisture fluxes (wq) at 3 PM (top) and 4 PM (bottom) on an XZ-cross section crossing the southern half of Lake Okeechobee. The vertical velocity (w) is in cm/s, while model's specific humidity (q) is in kg/kg. The magnitudes shown in the figures are for the products wq. Hereafter the west coast and east coast are indicated by the short vertical lines with "W" and "E" marks, respectively, shown on the bottoms of the XZ-cross section.

## 4-4 Deep Cumulus Convective Effects Upon the Peninsula-Scale Tropospheric Flow

Convective-produced effects on the surface flow have been illustrated in the previous section. The parameterized cumulonimbus effect upon the upper troposphere will be illustrated in this section.

Unfortunately, very little has been reported in the literature concerning deep convective-induced mesoscale tropospheric circulations for the Florida environment. Therefore it is necessary to compare several of the model results with observed deep convective activities in other areas. In the following figures, the pure convectively induced mesoscale circulations will be illustrated at 3 PM and 4 PM (when deep convective effects were most-well developed).

First we see from Fig. 4-4-1(a) that at 3 PM, the deep convection produced a "cooling-warming-cooling" pattern with height on the resolvable-scale potential temperature field. This pattern is caused by, respectively, cloud top overshooting cooling (including the cooling of adiabatic expansion associated with mesoscale upper tropospheric ascent); net convective heating; and surface downdraft cooling. The result of this heating profile is a "divergence-convergence-divergence" pattern of the horizontal flow (Fig. 4-4-1(b)). In particular, we see that the eastern branch of the surface outflow is related to the surface convergence mentioned in the previous section. At this time the outflow induced surface convergence (with a peak absolute value of $0.9 \times 10^{-4}\ s^{-1}$) is as large as the heating-induced mid-tropospheric convergence (a peak absolute value of $1.0 \times 10^{-4}\ s^{-1}$). Also, the surface divergence induced by the downdraft (a peak value of $1.1 \times 10^{-4}\ s^{-1}$) is as large as the upper tropospheric divergence (a peak value of $1.1 \times 10^{-4}\ s^{-1}$).

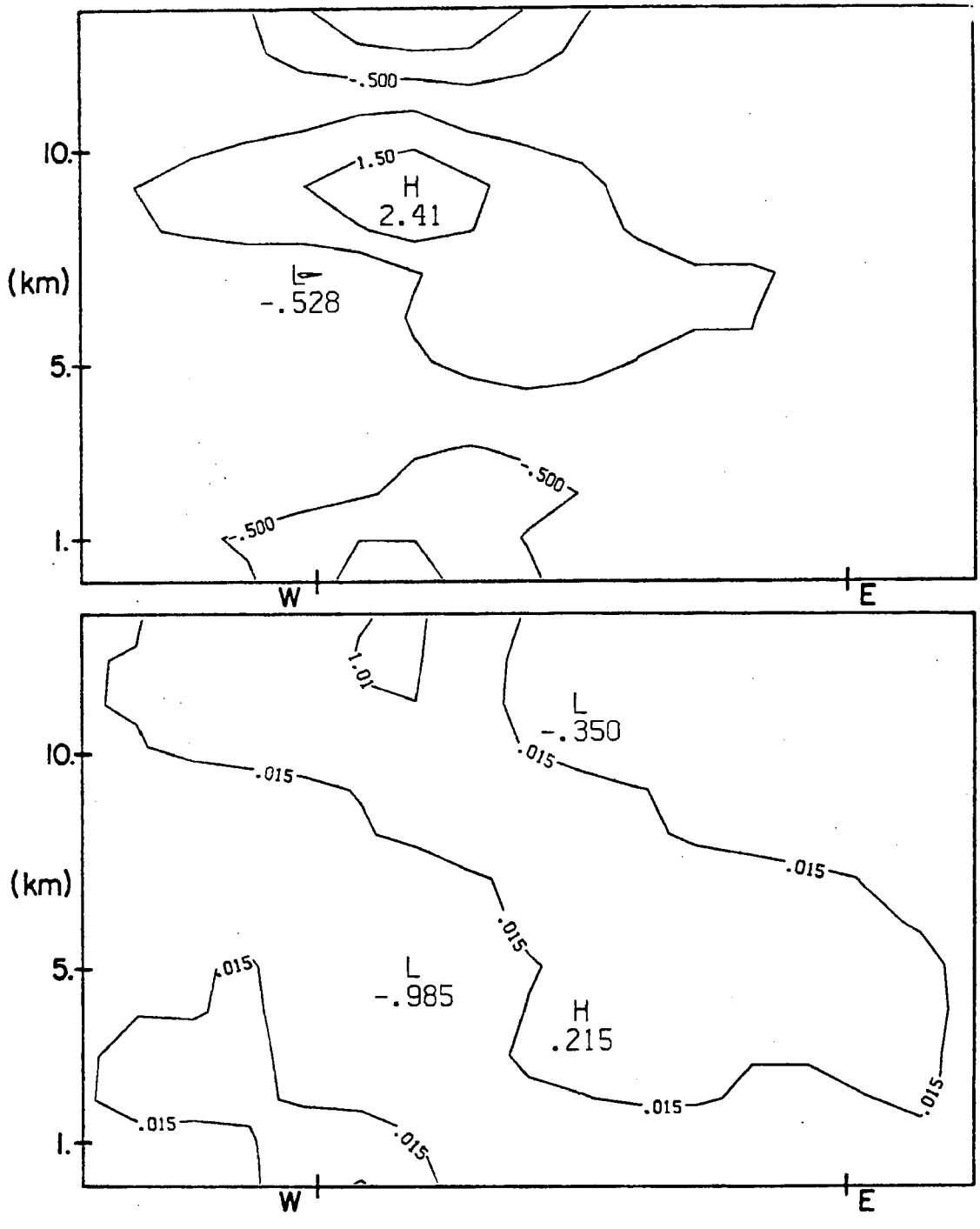


Figure 4-4-1. The "total-dry" potential temperature (°K, top) and horizontal divergence ($10^{-4}$ $s^{-1}$, bottom) at 3 PM, on the XZ-cross section crossing the southern half of Lake Okeechobee. The two coasts are indicated as in Fig. 4-3-9.

Due to the heating pattern shown above, a "four-cell" vertical solenoidal circulation pattern is evident in the horizontal u-velocity field (Fig. 4-4-2(a)) and the Y-direction vorticity field (Fig. 4-4-2(b)) (i.e., due to upper divergence; mid-level convergence and surface divergence). The production of such a four-cell circulation pattern indicates that the deep convective effect upon the mesoscale environment is not uniform in the vertical (i.e., not a single vertically stretched solenoidal circulation). Rather, deep cumulus convection appears to enhance mid-tropospheric horizontal convergence, while producing surface divergence due to downdraft cooling which then enhances surface convergence in the surrounding area. This statement is consistent with the fact that, in the absence of an upper-level synoptic or propagated mesoscale system disturbance, Florida's upper troposphere (above about 3 km) is free of horizontal divergences when only the dry sea breeze (without cumulus convection) exists. Thus, the convective induced warming of the mid and upper tropospheric mesoscale environment is directly responsible for the generation and enhancement of mid-tropospheric convergence. Johnson and Kriete (1982) described a similar cloud-induced upscale development for their tropical deep convective analysis. The effect of the convective heating on the vertical motion in a specific grid will be illustrated at the end of this section. Freeman (1984), using the 2-D model developed by Hack and Schubert (1976), obtained a similar circulation pattern with a similar heating pattern (although the surface cooling in their case is due to longwave radiation at night). The corresponding vertical motion field and the vertical component of vorticity are shown in Fig. 4-4-3(a) and (b), respectively.

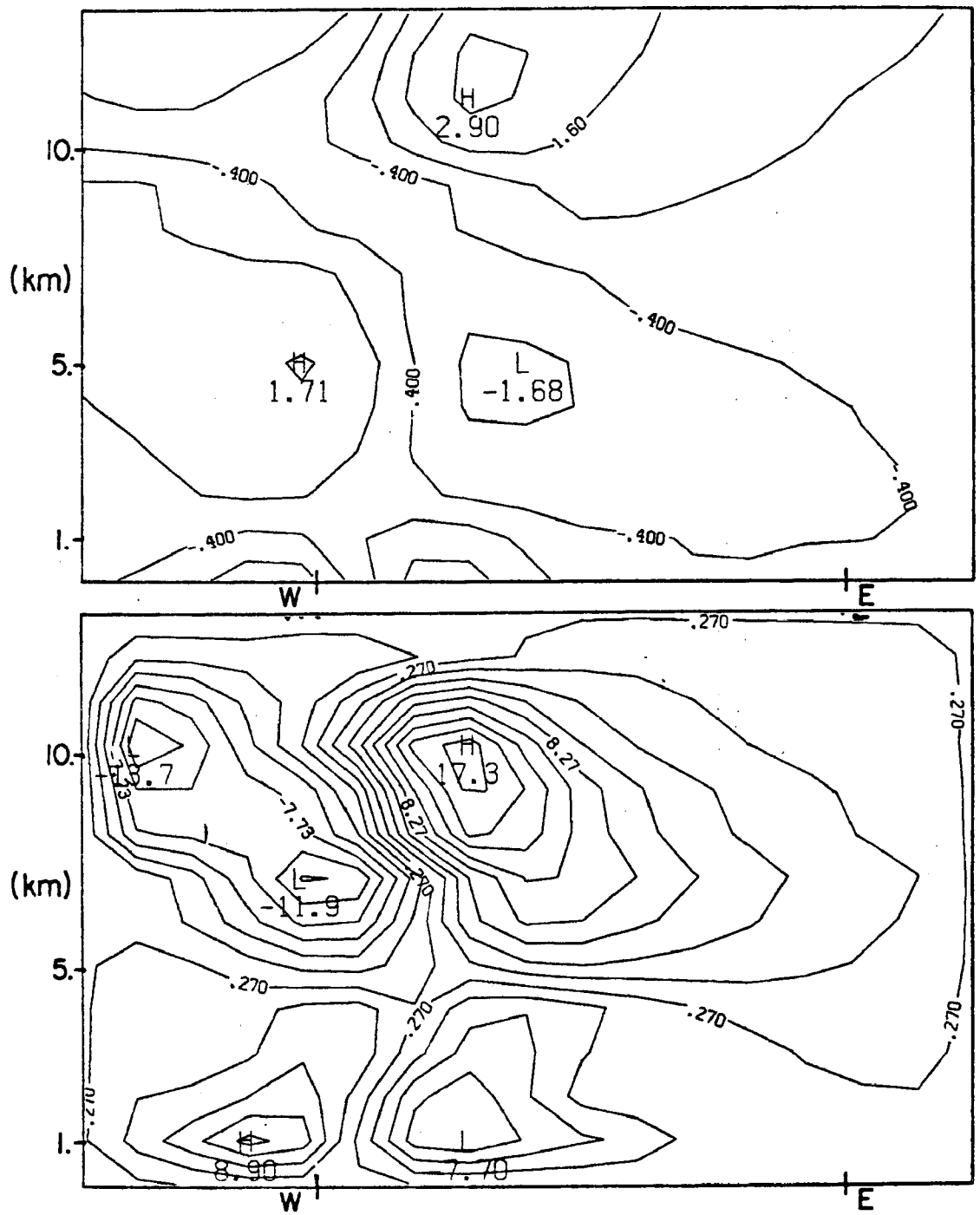


Figure 4-4-2. Same as Fig. 4-4-1 but for horizontal u-velocity (m/s, top) and Y-direction vorticity ($10^{-4}$ $s^{-1}$, bottom). For the latter, position values correspond to clockwise rotation on the XZ-plane.

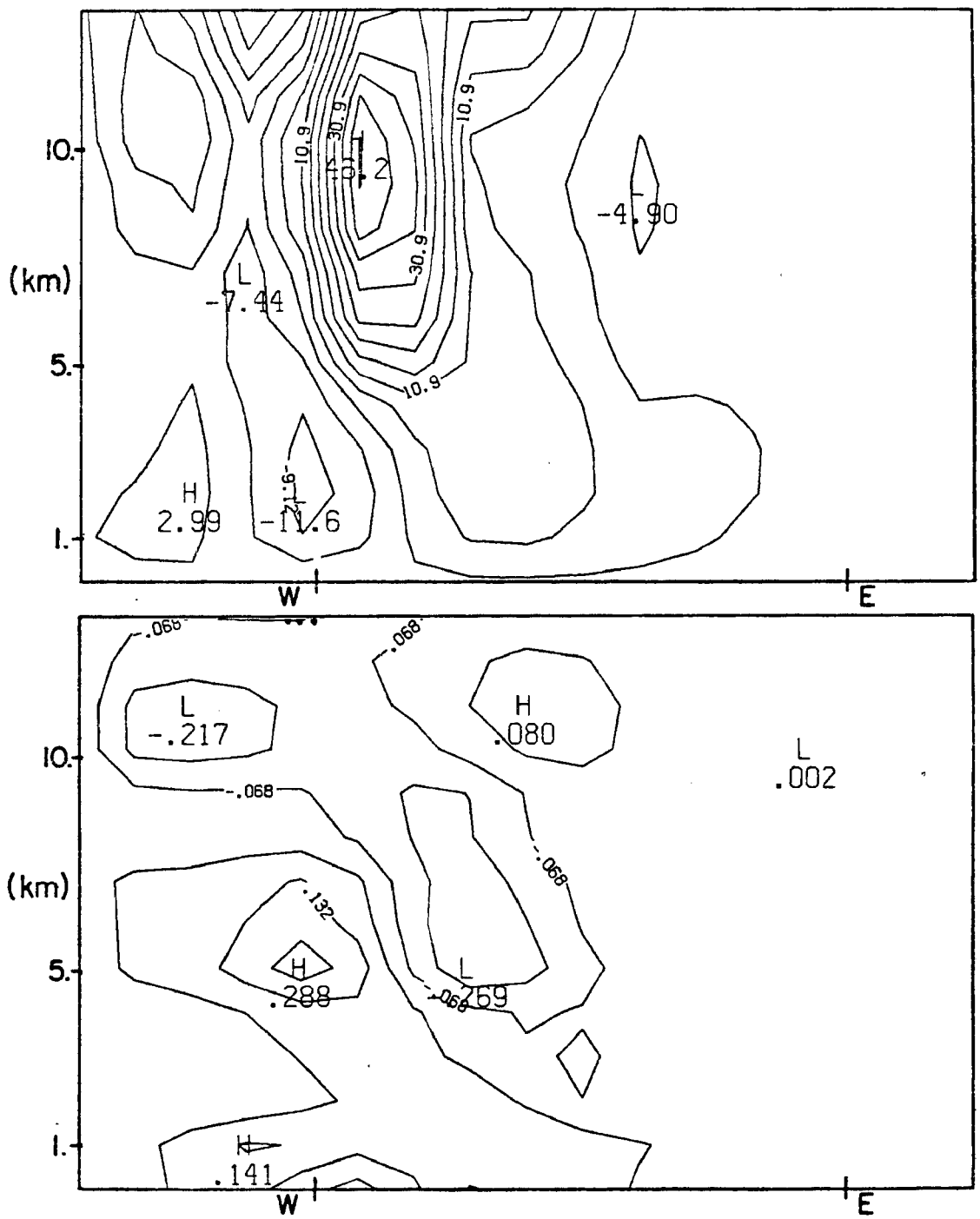


Figure 4-4-3. Same as Fig. 4-4-1 but for vertical velocity (cm/s, top) and vertical vorticity ($10^{-4}$ $s^{-1}$, bottom).

The mesoscale model used in the current study does not include latent heat release on the resolvable-scale field (i.e., all moist processes are produced in the convective parameterization). Therefore, this model does not generate the mesoscale updraft/downdraft introduced in Leary and Houze (1979), among others. In spite of this, however, the above results are very similar to an observed mid-latitude squall line documented in Ogura and Liou (1980), as shown in Figure 4-4-4 (reproduced from Ogura and Liou, 1980). Figure 4-4-4 contains quantities which are on a relative coordinate framework moving with the observed squall line. In this sense, the dynamic and thermodynamic structures shown in Fig. 4-4-4 should be comparable to the corresponding "total-dry" quantities illustrated in the current study. Comparing Fig. 4-4-1(b) with Fig. 4-4-4(b), we see that in both cases the surface convergence (in the lowest 1 km) is located ahead (i.e., upwind, with respect to the low-level environmental flow) of the mid-tropospheric convergence (around 500-600 mb, or 5 km). The result of these convergences are two upward motion centers (Fig. 4-4-3(a) and Fig. 4-4-4(c)): one near 700 mb and an upper one near 400 mb (or around 10 km); and a downward motion center near 700-800 mb (or around 2-3 km). Related to these are the vorticity fields (Fig. 4-4-3(b) and Fig. 4-4-4(d)) and the horizontal wind components which also are analogous between Fig. 4-4-2(a) and 4-4-4(a), for example, as seen by the easterly component whose maximum tilts with height.

The above described resemblance between the current study and Ogura and Liou (1980) must be interpreted realizing a difference existed in the background wind between the two cases. The background large-scale wind considered in the current study has its easterly

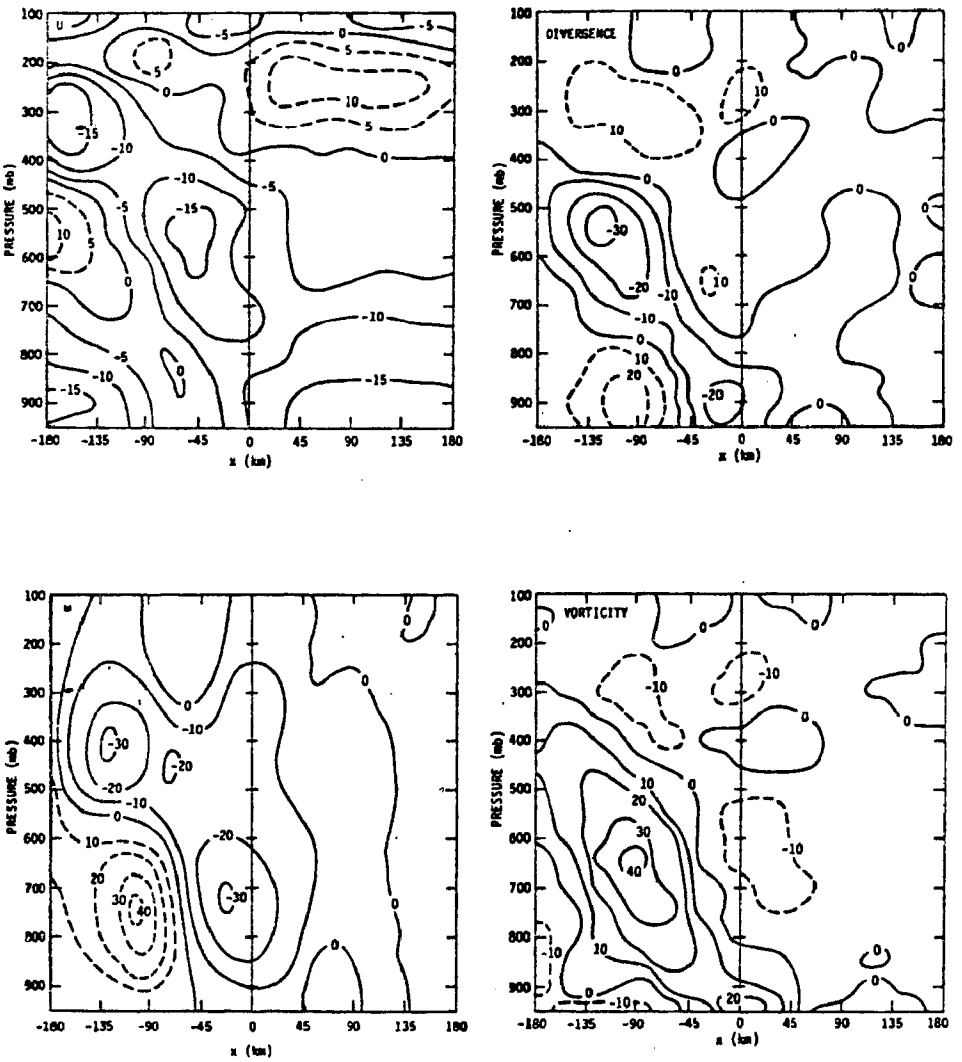


Figure 4-4-4. The XZ-cross sections of some of the observed mid-latitude squall line quantities: horizontal u-velocity (m/s, upper left); horizontal divergence ($10^{-5}$ $s^{-1}$, upper right); vertical p-velocity ($10^{-3}$ mb $s^{-1}$, lower left and vertical vorticity $10^{-5}$ $s^{-1}$, lower right) (from Ogura and Lious, 1980).

maximum in the upper troposphere with weaker easterly winds in the mid-and lower-troposphere. This wind structure is different from that in Ogura and Liou (1980) in which a westerly jet dominated the upper troposphere. In their study, it was stated that around the mid-troposphere (during the lifetime from mature stage to decaying stage), the westerly background momentum opposes the easterly momentum which is carried upward by the low-level inflow. The result of this is mid-tropospheric convergence. The mid-level inflow from the rear of the system was indicated to be primarily responsible for generating a mesoscale downdraft through evaporational cooling by providing an input of relatively dry air.

Recently, Small and Hauze (1986) have performed a more detailed radar analysis of the squall-line system which was previously analyzed by Ogura and Liou (1980). Among their results, they indicated that a "mid-level jet" originating from the front of the system is primarily responsible for the generation of the stable-type precipitation to the rear of the system, by providing the bulk of the condensate (ice particle in particular) transport from the deep convective region to the mesoscale anvil region. Downdrafts were active both in the lower troposphere (where they provide the displacement forcing as discussed in Raymond, 1986, and the current study) and in the upper troposphere. The mid-tropospheric convergence was pointed out by them to be associated with the downward-transported upper-level horizontal momentum due to the upper-tropospheric downdraft (which seems to be generated due to horizontal convergences around tropopause surrounding the convective region.)

In the current study, since the dry sea breeze circulation does not, in general, produce significant perturbations upon the mid- and

upper-troposphere, and because no explicit latent heating processes were represented on the grid-scale, the "total-dry" quantities should indicate the mesoscale responses due to pure cumulus convective forcing. Therefore, the mid-tropospheric convergence obtained in the current study, and the associated mesoscale upward and downward motions, are initiated and enhanced solely due to the convective heating in the upper troposphere and the convective-scale downdraft cooling in the lower troposphere. In their observational analysis of the Winter MONEX, Johnson and Kriete (1982) indicated that the convective-scale processes (melting and evaporation at low levels and condensation and freezing at upper levels) seemed to be able to drive a larger-than-cloud-scale circulation (mid-tropospheric convergence forced by vertically-divergence air streams) which, in turn, feeds back to enhance cloud growth (that is, a type of cooperative instability mechanism).

By 4 PM, Fig. 4-4-5(a) shows that the resolvable-scale warming/cooling pattern becomes somewhat more complicated. A newly formed cooling-warming center is found around the mid-low troposphere in the original convective area (the system has moved eastward). The general structure of the dynamic quantities basically is retained, however, as seen in the horizontal divergence (Fig. 4-4-5(b) and the horizontal flow (Fig. 4-4-6(a)). Comparing the vertical motion structure (Fig. 4-4-7(a)) with the temperature field (Fig. 4-4-5(a)), we see that the newly formed mid-tropospheric cooling/warming center is due to adiabatic cooling due to mesoscale vertical motion and mesoscale subsidence warming, respectively.

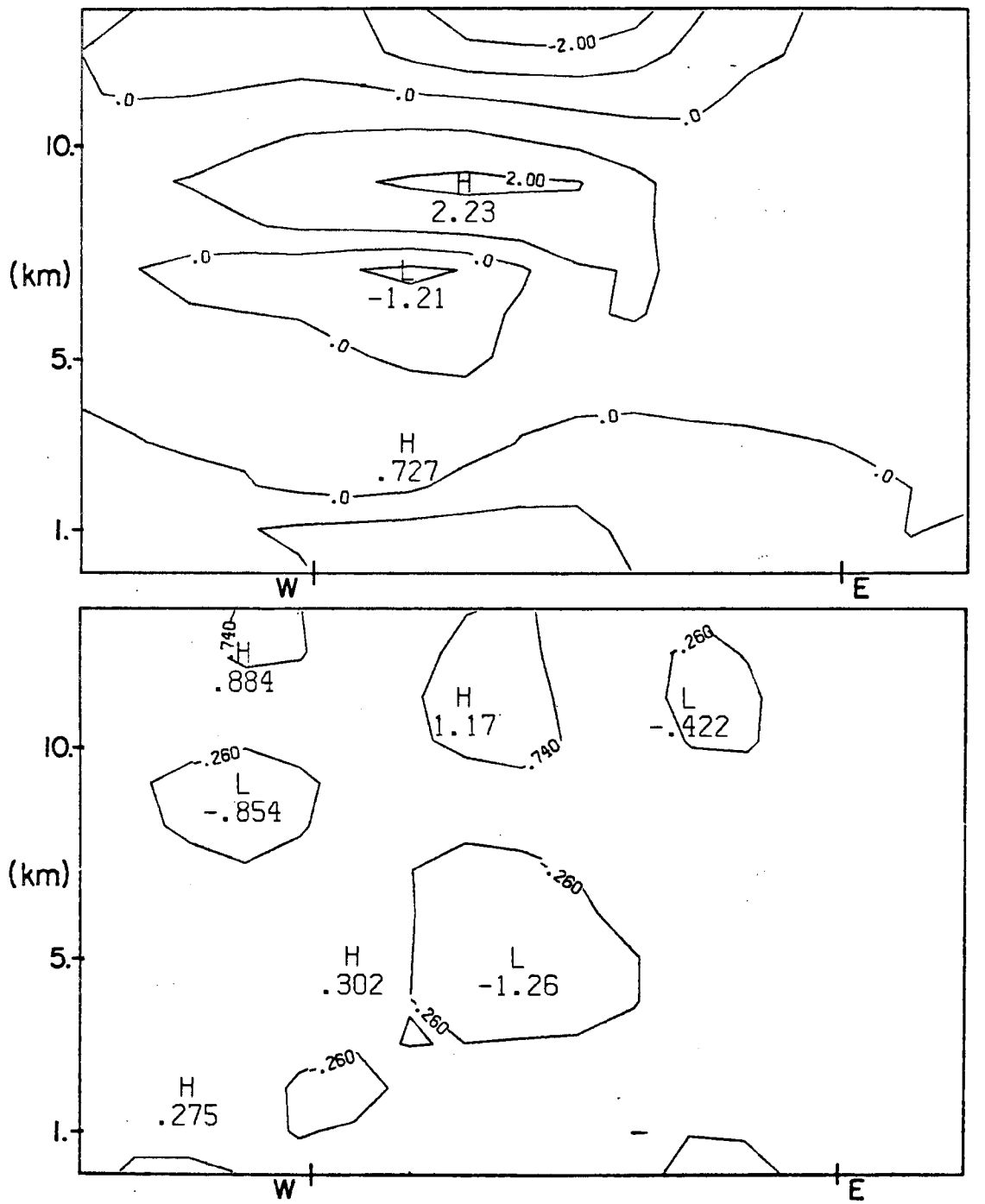


Figure 4-4-5. Same as Fig. 4-4-1 but for 4 PM.

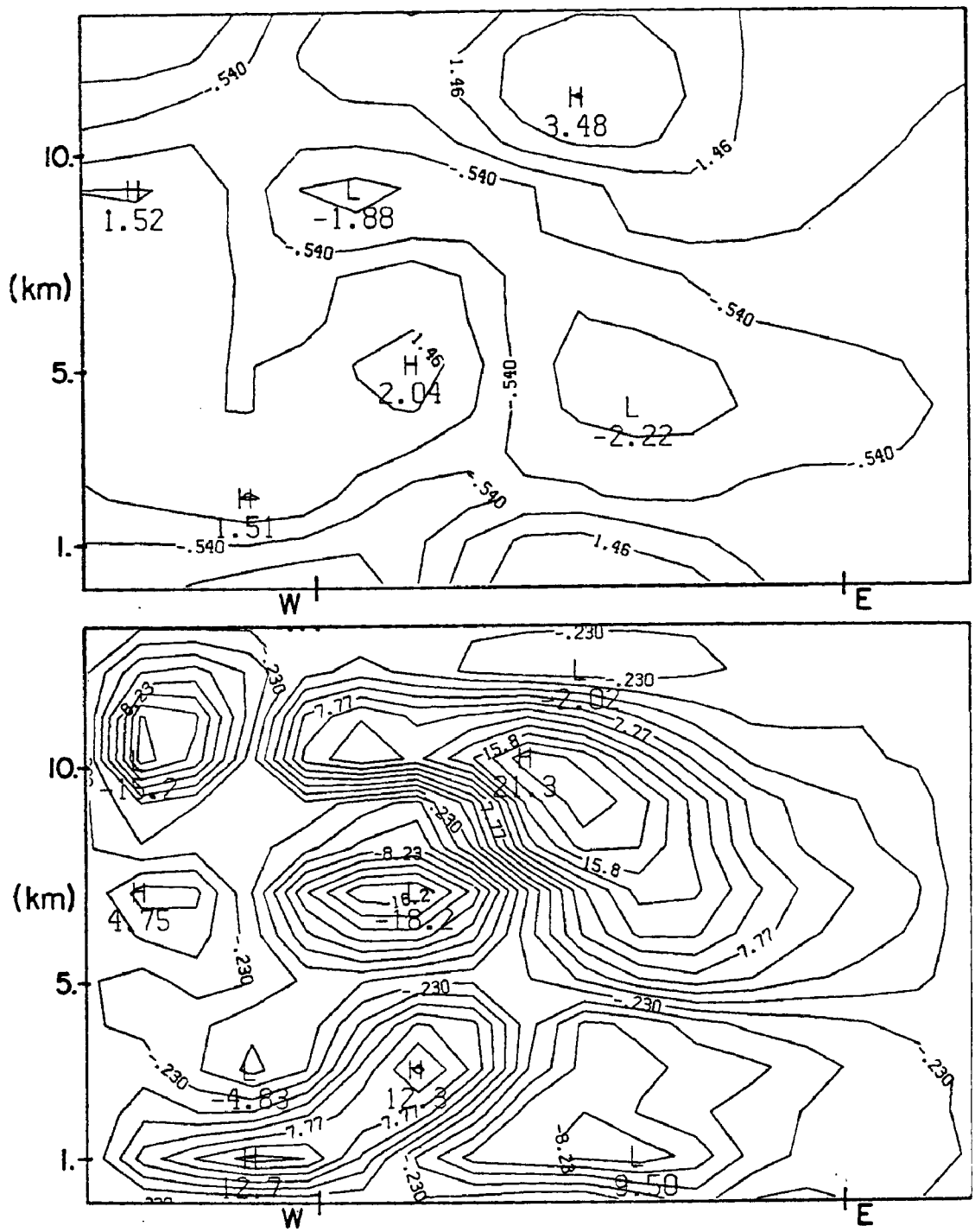


Figure 4-4-6. Same as Fig. 4-4-2 but for 4 PM.

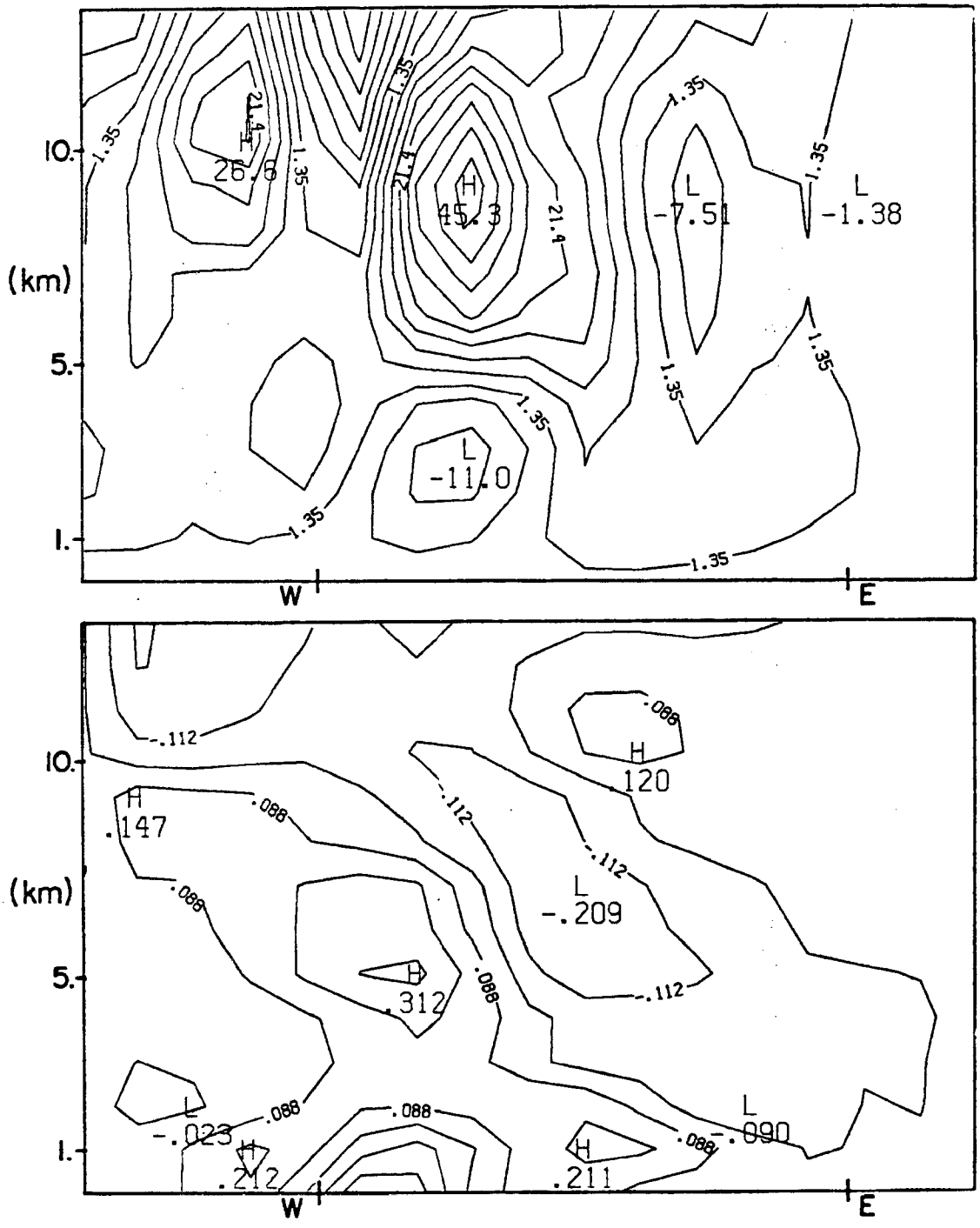


Figure 4-4-7. Same as Fig. 4-4-3 but for 4 PM.

Figure 4-4-8 and Fig. 4-4-9, respectively, show the horizontal maps of the upper tropospheric (near 12 km) horizontal divergence and (the vertical component of) vorticity, for the time period of 11 AM-4 PM. The vorticity is associated with the atmospheric adjustment processes (toward geostrophic balance) due to the horizontal convergent/divergent motions. Comparing Fig. 4-4-8(a) through (f) with Fig. 4-4-9(a) through (f), we see that positive vorticity (i.e., cyclonic rotation) is related to the convergent flow field and negative vorticity to the divergent flow field.

Summarizing various observational and numerical investigations of convective downdraft effects, we see that convective downdrafts typically have two distinct feedback effects upon the convective system from which the downdraft is initiated. The first is that surface stabilization by downdrafts such that convective development becomes weakened within the original convective area (Molinari and Corsetti, 1984). The second effect is that downdrafts are able to enhance subsequent convection through the surface outflow feedback mechanism (the "displacement instability" as described in Raymond, 1986).

Molinari and Coresetti (1984), using a modified Kuo-type cumulus parameterization, indicated that without convective downdrafts the simulated rainfall significantly exceeded the observed amounts. Without the downdraft stabilization, in their model, there is an unrealistic positive feedback between convective-generated upper-level warming and lower-level convergence, which lead to overestimations of rainfall generation, as compared to observations.

Among the several existing convective parameterizations used for simulating mesoscale convective weather systems, Raymond (1986) introduced one which pays particular attention to the downdraft displacement

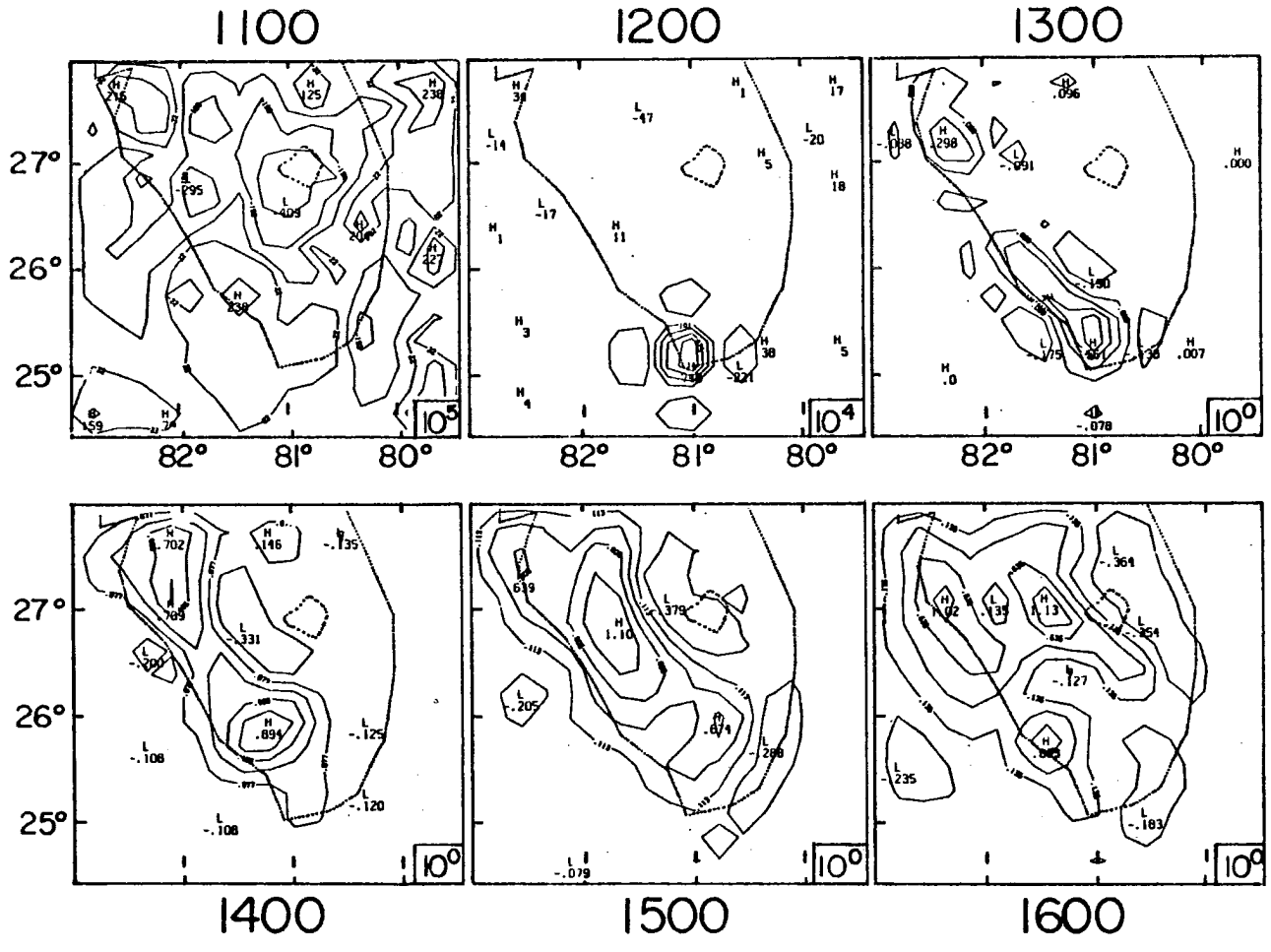


Figure 4-4-8. The model produced horizontal divergence ($10^{-4}$ $s^{-1}$) around tropopause (~12 km) between 1100 EST and 1600 EST at the interval of one hour. Scaling factors are included in each figure.

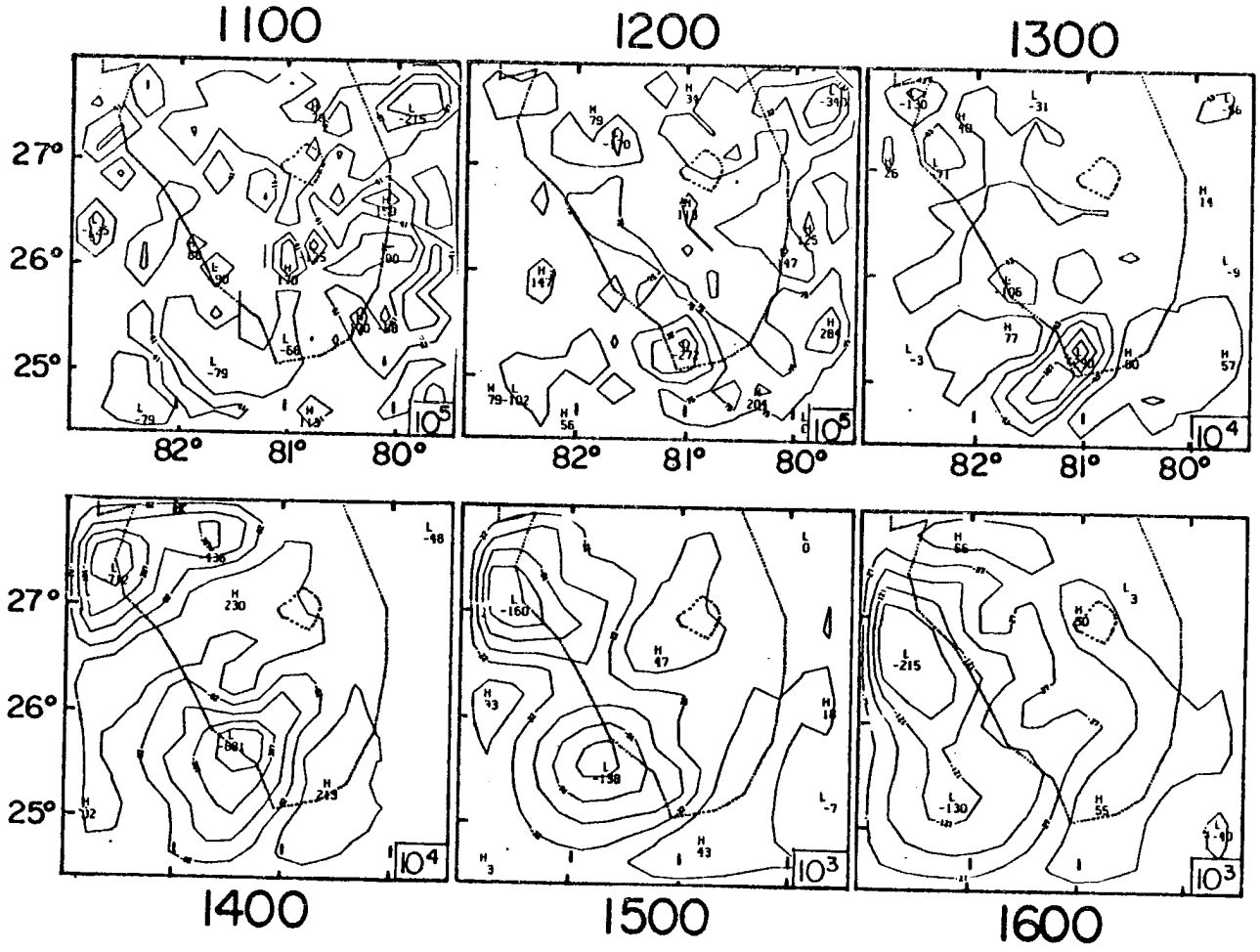


Figure 4-4-9. The model produced vertical vorticity ($10^{-4}$ $s^{-1}$) around tropopause (~12 km) between 1100 EST and 1600 EST at the interval of one hour. Scaling factors are included in each figure.

effect. By adding the downdraft effect into his simulation, Raymond (1984) found that, in addition to the "propagating mode" which was obtained before, a new mode was present (which advects with the steering flow, or is stationary if there is no background wind). Relatively strong convective development is found to be associated with this "advecting mode" before the system evolves into the propagating stage. In Raymond (1986), the downdraft effects associated with the advecting mode was defined as the "displacement instability".

In the current study, both of the above described downdraft feedback effects (stabilization and enhancement) have been simulated. For example, the downdraft stabilization effect produces downward motion in the lower troposphere during the latter stage of the convective system over the original convective area (Fig. 4-4-7). Meanwhile, as discussed throughout Chapter 4, downdraft cooling produces an outward surface pressure gradient force surrounding the convection which generates a new favorable environment for subsequent convective development (Fig. 4-4-9). It will be shown in Chapter 5 that without the downdraft effect the system develops with a much weaker intensity during the late afternoon.

Finally, to illustrate the convective effect upon the resolvable-scale field, a grid point near the west coast at the latitude of Lake Okeechobee is chosen as an example. During the time between 2:15 and 4:02 there are five "clouds" simulated by the parameterization, separated by about 21-22 min. In the following figures, at each cloud initiation time (indicated in the figures) the input grid-scale vertical velocity profile (Fig. 4-4-10), the parameterized convective heating profile (Fig. 4-4-11) and the convective moistening profile (Fig. 4-4-12) are shown.

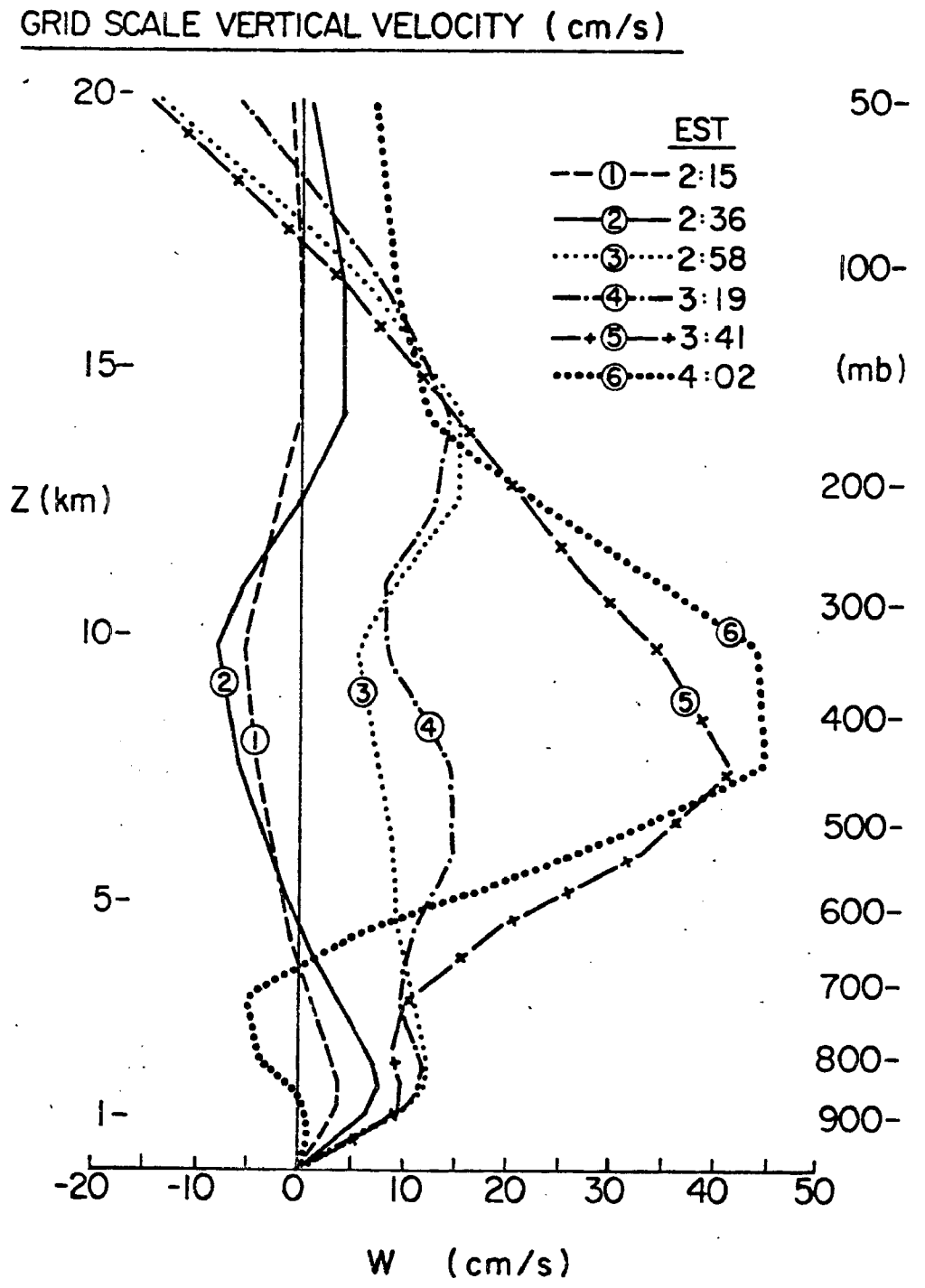


Figure 4-4-10. The time-variations of model's grid-scale vertical velocity (cm/s) as a result of the convective heating. Numbers of the curves indicate the sequential order of the vertical velocity profiles (with times of a day shown in the figure). At a grid point near the West Coast.

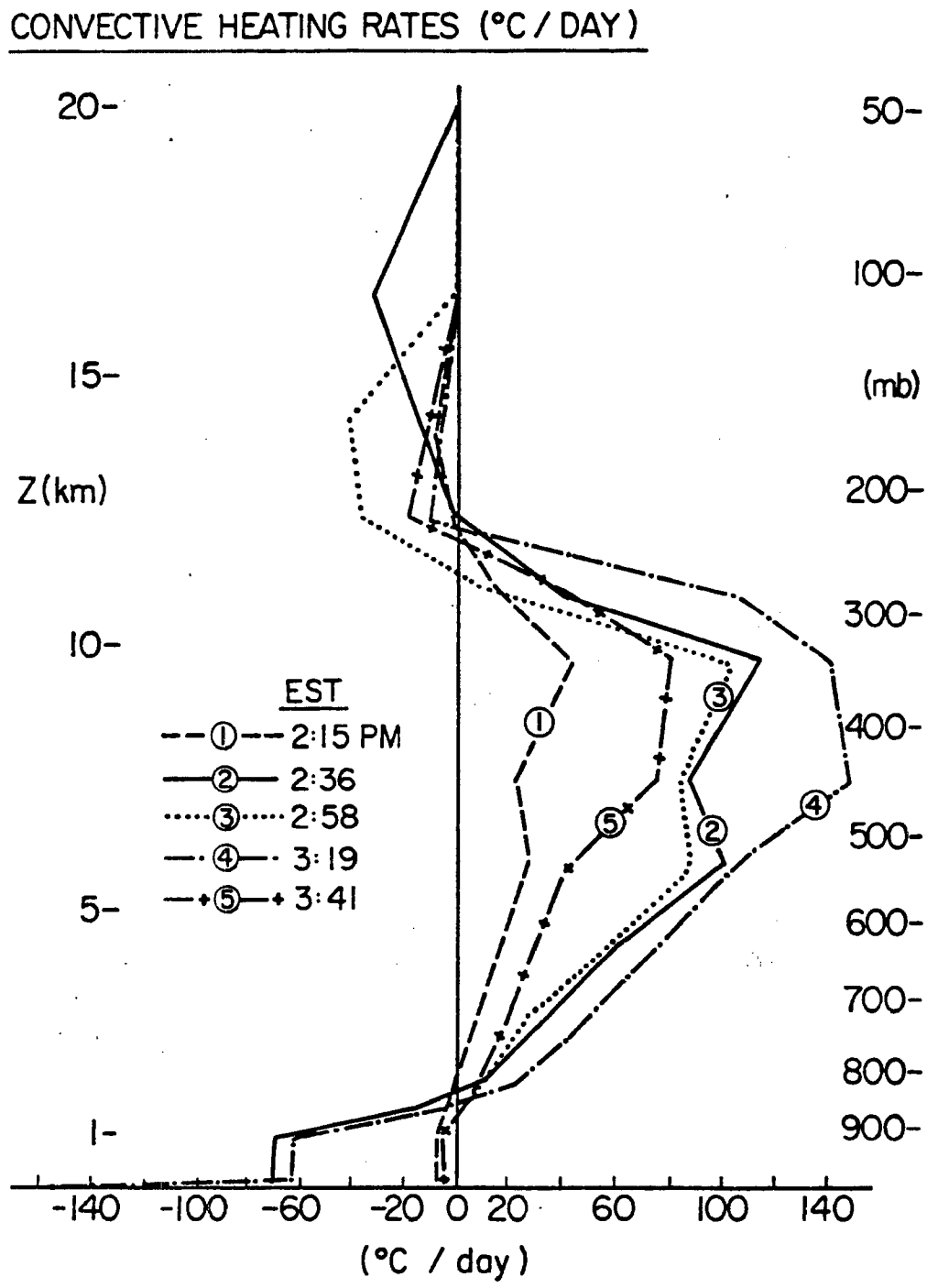


Figure 4-4-11. Same as Fig. 4-4-10 but for the convective neating (degree-C per day) profiles (results are from the convective parameterization at the time indicated).

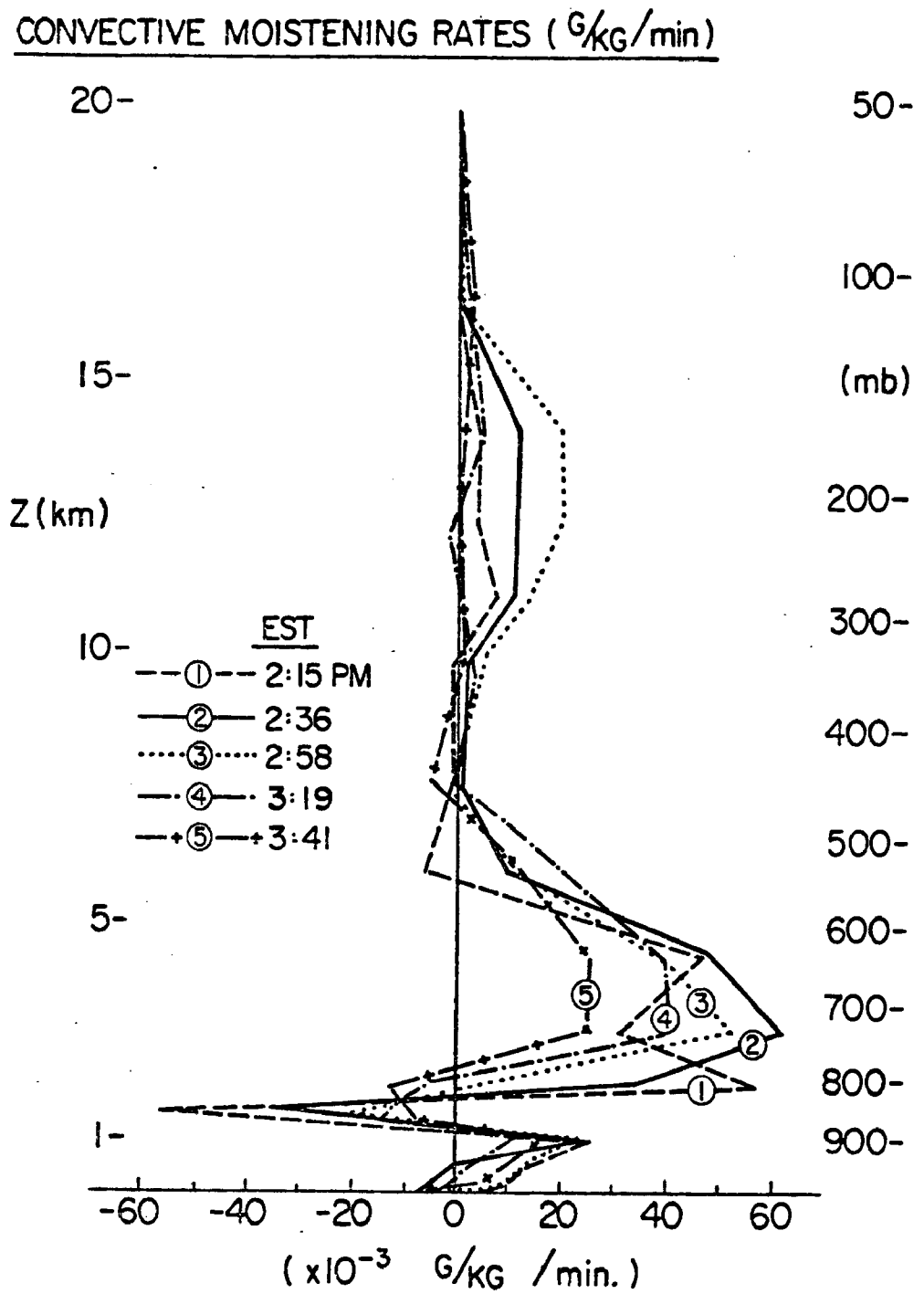


Figure 4-4-12. Same as Fig. 4-4-11 but for the convective moistening ($10^{-3}$ g/kg per minute) profiles.

Before 2:15, no cloud developed in this grid. Therefore, as seen in Fig. 4-4-10, curve (1) indicates there is weak downward motion throughout the mid and upper troposphere (presumably due to the compensating downward motion caused by neighboring convection) and weak upward motion in the lower troposphere due to sea breeze convergence. The first cloud is initiated at 2:15, which produces the convective heating profile shown as curve (1) in Fig. 4-4-11. We see there is relatively weak heating (a peak value of ~40°C/day) near 350 mb, and very weak cooling in the subcloud layer (~5°C/day). This cloud is in stage 1 as defined in Chapter 3, therefore no downdraft cooling is incorporated.

The above heating is then incorporated into the mesoscale model for the following 20 minutes (equally divided into each time step). The resultant grid-scale vertical velocity after the 20 min is shown as curve (2) in Fig. 4-4-10 (at time 2:36). It is seen that relatively very little change is made due to the weak heating. However, the next cloud (or the stage 2 convection) produces strong heating (a peak value 113°C/day, near 325 mb) and strong cooling (-70°C/day in the subcloud layer and ~-150°C/day at the surface; also a cooling of about -30°C/day around cloud top). The grid-scale response is shown as curve (3) in Fig. 4-4-10. We see that significantly increased upward motion has become established on the resolvable-scale.

The largest increase of the grid-scale vertical velocity is between 3:19 and 3:41 (i.e., from curve (4) to curve (5) in Fig. 4-4-10), which is the result of the mature stage convective heating shown as curve (4) in Fig. 4-4-11. After this development, the grid element is stablized (due to both the upper heating and the lower-level

downdraft cooling). Therefore, curve (6) in Fig. 4-4-10 already indicates downward motion in the lower troposphere (i.e., the system is in a decaying stage). Accordingly, there is no new cloud initiated at this grid.

Figure 4-4-12 shows that the deep convection provides important moistening over the layer between about 500 mb and 800 mb, and to a weaker degree around the tropopause (anvil evaporation). Subsidence motion produces drying between 800 mb and 900 mb, while downdraft evaporation acts as a moisture source in the subcloud layer.

The heating and moistening profiles obtained from the current scheme have been compared with various observational analyses both quantitatively and qualitatively - for mid-latitude: Ogura and Liou (1980); for Florida: Byers and Braham (1949), Simpson and Wiggert (1971); and for the tropics: Ogura et al. (1979), Song and Frank (1983). For similar spatial and time domains, the profiles obtained in this study are generally consistent with the observations.

# Chapter 5

# PHYSICAL SENSITIVITY EXPERIMENTS

## 5-1. Introduction

It was discussed in the last chapter that Florida's summertime deep cumulus convection is closely related to both the sea breeze circulation and mesoscale circulation caused in response to cooling of boundary layer air by deep cumulus-generated downdrafts. Boundary layer cooling produced by the downdrafts plays a major role in focusing subsequent deep convective development.

It is instructive to see how this mesoscale-convective interrelationship depends on various physical forcing mechanisms. In this chapter, four simulations are performed which are otherwise exactly the same as the control run except for the following changes:

(a) weak southeasterly run—a very weak ($\sim$1 m/s) southeasterly wind is used (for the whole vertical domain) for initiating the model;

(b) strong southeasterly run—as above but with a very strong ($\sim$14 m/s) southeasterly wind;

(c) drier sounding run—initial relative humidity between 800 mb and 500 mb is reduced by about 10 percent (the layer averaged relative humidity is reduced from 63 percent to 53 percent);

(d) no-downdraft run—convective downdraft effect is eliminated.

In the following sections, each of the sensitivity experiments will be briefly discussed using vertical cross sections of the vertical

velocity field at 3 PM and 4 PM, and horizontal maps of the vertical velocities at 10 km and 1 km (for 4 PM only). Attention is paid primarily to the results which differ significantly from the control runs.

5-2. Weak Southeasterly Experiment

In terms of the initial surface wind, this experiment resembles the light and variable category included in McQueen and Pielke (1985), since both have weak wind near the surface in the early morning. This experiment, however, is initiated with the thermodynamic stratification of the control run, which has an initial environment that is moister than that associated with the light and variable category discussed in McQueen and Pielke (1985). Nevertheless, it is seen that the model has simulated deep convective developments at 4 PM (Fig. 5-1) around the southwest coastal region and near the Lake Okeechobee. These two locations correspond well with the two deep convective regions of the light and variable category at 4 PM (see in Fig. 5-2, reproduced from McQueen and Pielke, 1985).

Figure 5-3(a), shows that at 3 PM the core upward velocity developed in the weak wind run is somewhat stronger than that of the control run (Fig. 4-4-3(a)). This suggests that for weaker upper-level wind, the convective-generated warming is less affected by the upper-tropospheric horizontal advective processes (which dilute the heating by advecting relatively cooler upwind air into the convective region), and therefore the net convective effect is stronger. By 4 PM, the convective system has propagated upwind by a rather significant distance (Fig. 5-3(b)). The peak upward velocity, however, becomes much weaker than the control run's (Fig. 4-4-7(a)) due to weaker

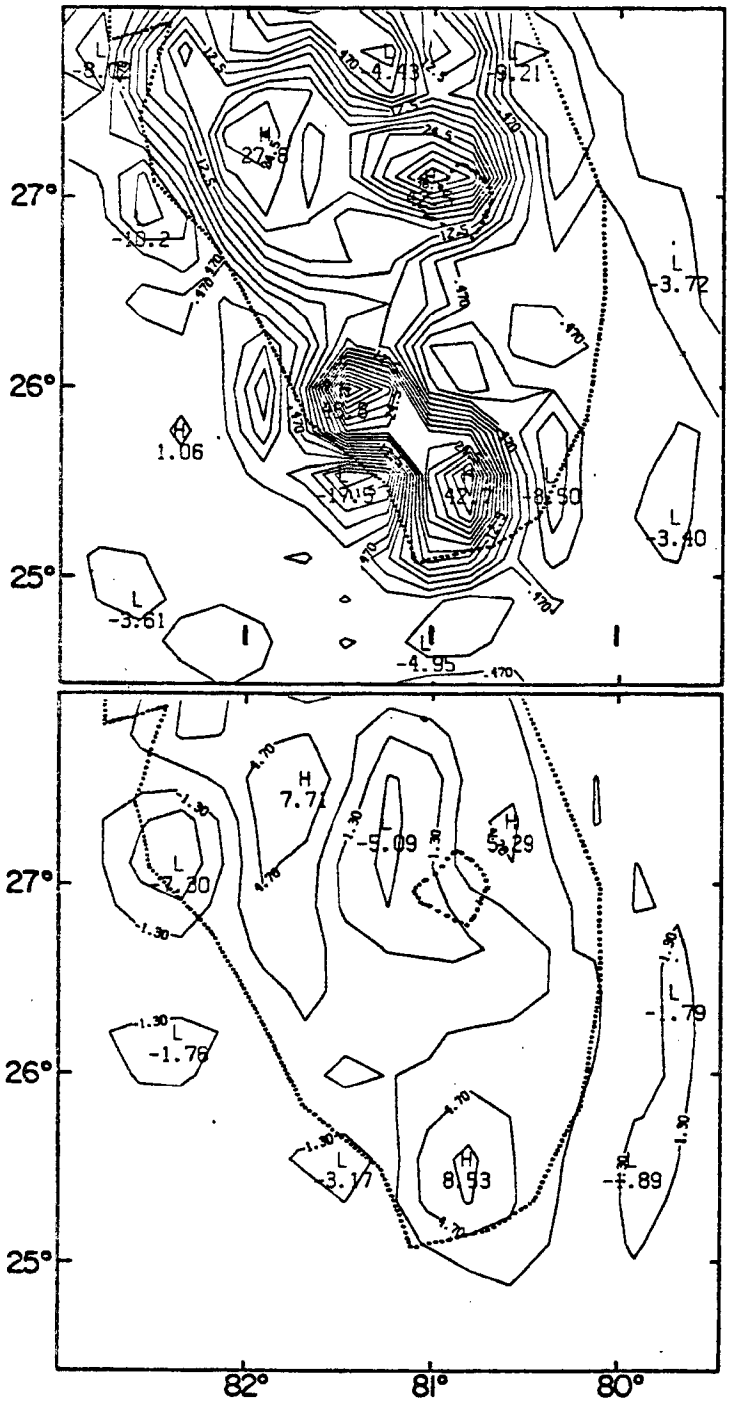


Figure 5-1. The model produced vertical velocities (cm/s) at 4 PM around 10 km (top) and 1 km (bottom) for the weak-southeasterly experiment.

Figure 5-2. Satellite image composites by synoptic flow for (a) strong east and (b) light and variable classes at 1600 EST (from McQueen and Pielke, 1985).

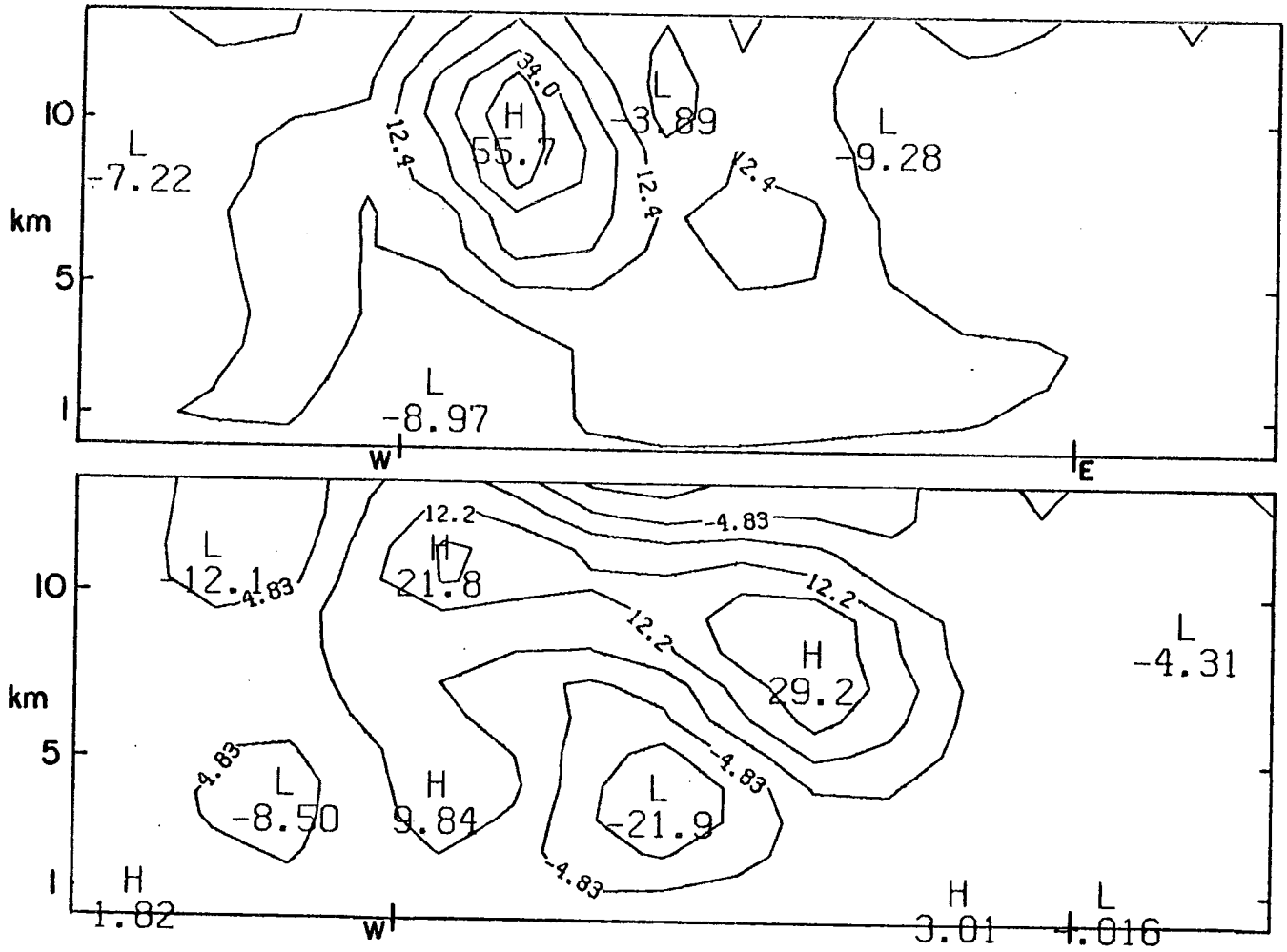


Figure 5-3. Vertical velocities (cm/s) at 3 PM (top) and 4 PM (bottom) on the XZ-cross section for the weak southeasterly experiment.

surface convergence in this experiment than in the control run. This weaker convergence occurs because the surface flow over the peninsula is weaker in this case (this also indicates that the convective development depends on the intensity of the sea breeze circulation).

5-3. Strong Southeasterly Experiment

This experiment differs from the control run in that it is initiated with very strong ($\sim$14 m/s) wind throughout the mid-lower troposphere, while the control run has the same initial wind speed only around the tropopause.

Figure 5-4 shows that at 4 PM the major deep convective developments are in the area to the northwest of Lake Okeechobee, and two other locations of somewhat less strength around Tampa and the west coast near Fort Myers. The main upward motion zone (Fig. 5-4(a)) covers a large area surrounding, and to the west of, the Lake Okeechobee.

Due to the much stronger synoptic wind in this experiment, as evident from Fig. 5-5 the west coast convective system has less inland propagation than in the control run. Furthermore, Fig. 5-5 shows that the surface divergence/convergence coupling is much weaker than in the control run, indicating that (for the XZ-plane) a very strong boundary layer horizontal background wind tends to inhibit the generation of the downdraft cooling effect discussed in Chapter 4.

5-4. Drier Sounding Experiment

This experiment differs from the control run only in that the relative humidity in the 800-500 mb layer is reduced by about 10 percent.

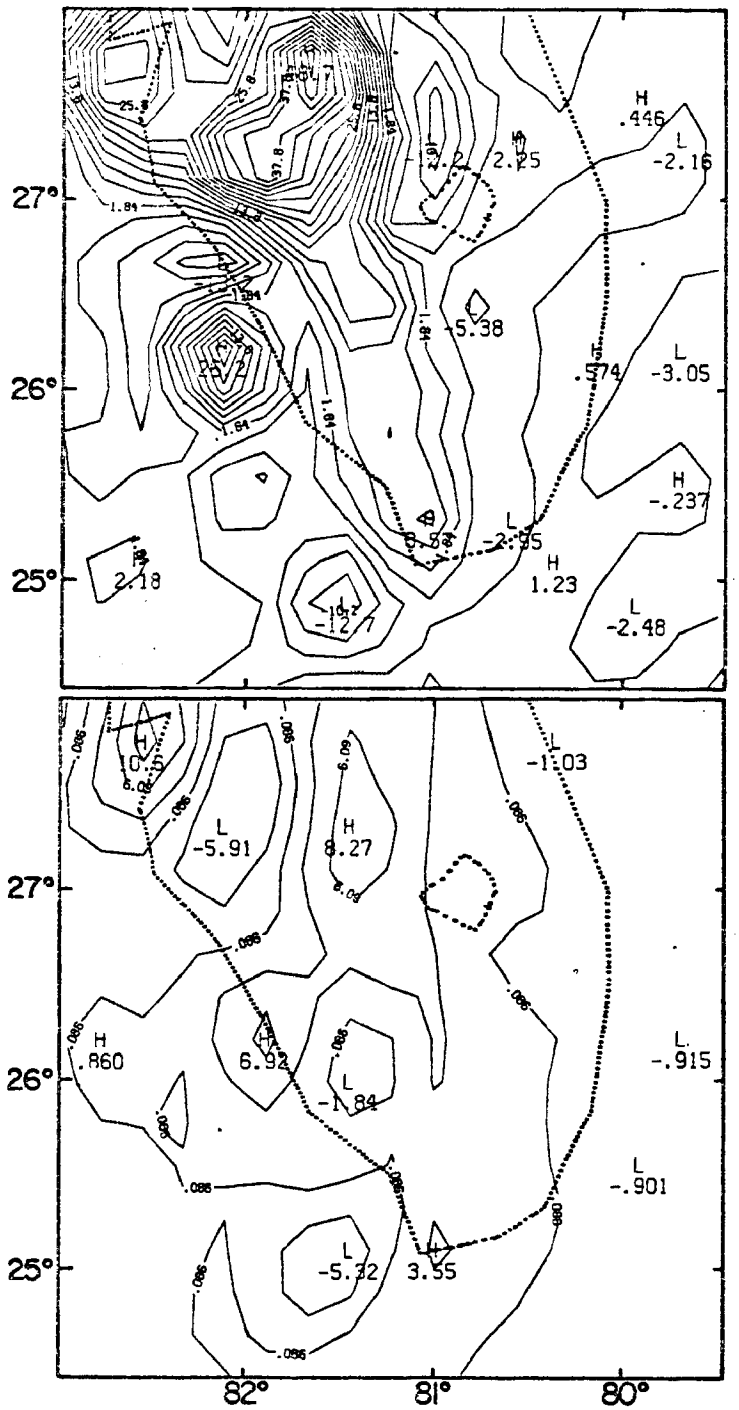


Figure 5-4. The model produced vertical velocities (cm/s) at 4 PM around 10 km (top) and 1 km (bottom) for the strong-southeasterly experiment.

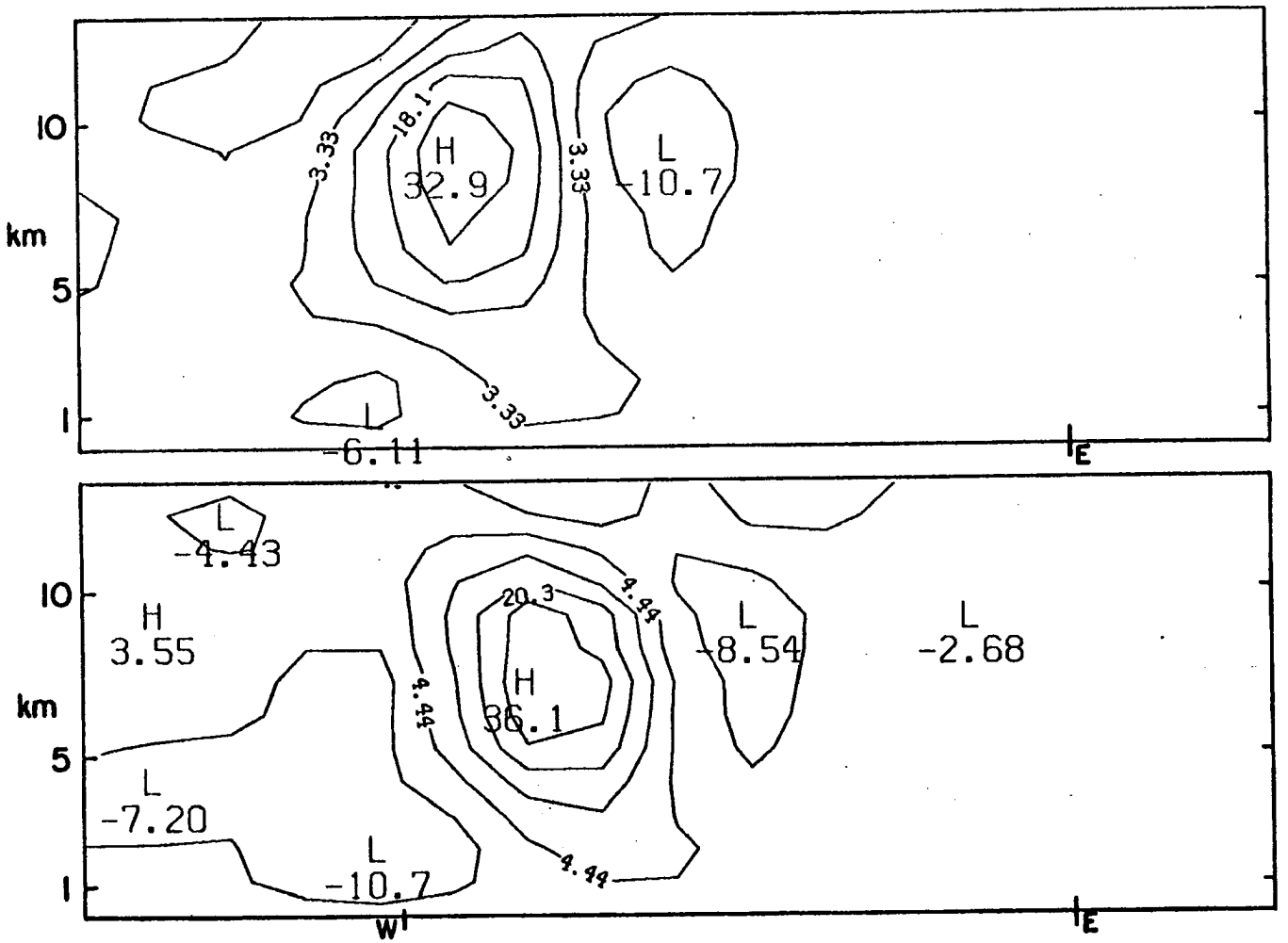


Figure 5-5. Vertical velocities (cm/s) at 3 PM (top) and 4 PM (bottom) on the XZ-cross section for the strong southeasterly experiment.

Due to the initial drier environment, the deep cumulus convective development is slower than the control run's during the earlier afternoon. However, during the late afternoon, convective downdraft cooling is generated which appears to be as strong, or in some occasions even stronger than, those of the control run. This implies that the drier environment is contributing, among other factors, to the generation of the strong downdrafts (Knupp, 1985). Therefore, we see from Fig. 5-6 that the maximum upward velocities at both 3 PM and 4 PM are comparable to the control runs. Also, Fig. 5-6 shows that the surface divergence-convergence coupling is clearly present in this experiment, indicating that the drier initial environment incorporated in this case is associated with producing relatively strong downdraft cooling during the late afternoon. Figure 5-7 shows the horizontal maps of the vertical velocities at 10 Km (top) and 1 Km (bottom) of the Drier Sounding Run.

## 5-5. No-Downdraft Experiment

This experiment is otherwise exactly the same as the control run except that convective downdraft effects are omitted in the parameterization. As discussed previously throughout this study, without the downdraft effect it is not expected that a surface pressure gradient force on the mesoscale due to downdraft cooling will develop as discussed in Chapter 4.

Figure 5-8 shows that there is much smaller inland propagation in this case than in the control run. More importantly, the maximum vertical velocity by 4 PM is already weaker than that at 3 PM, indicating that a decaying situation started as early as 3 PM. Also, we see that there is no surface divergence and convergence of the type produced in the control run in response to the downdraft cooling.

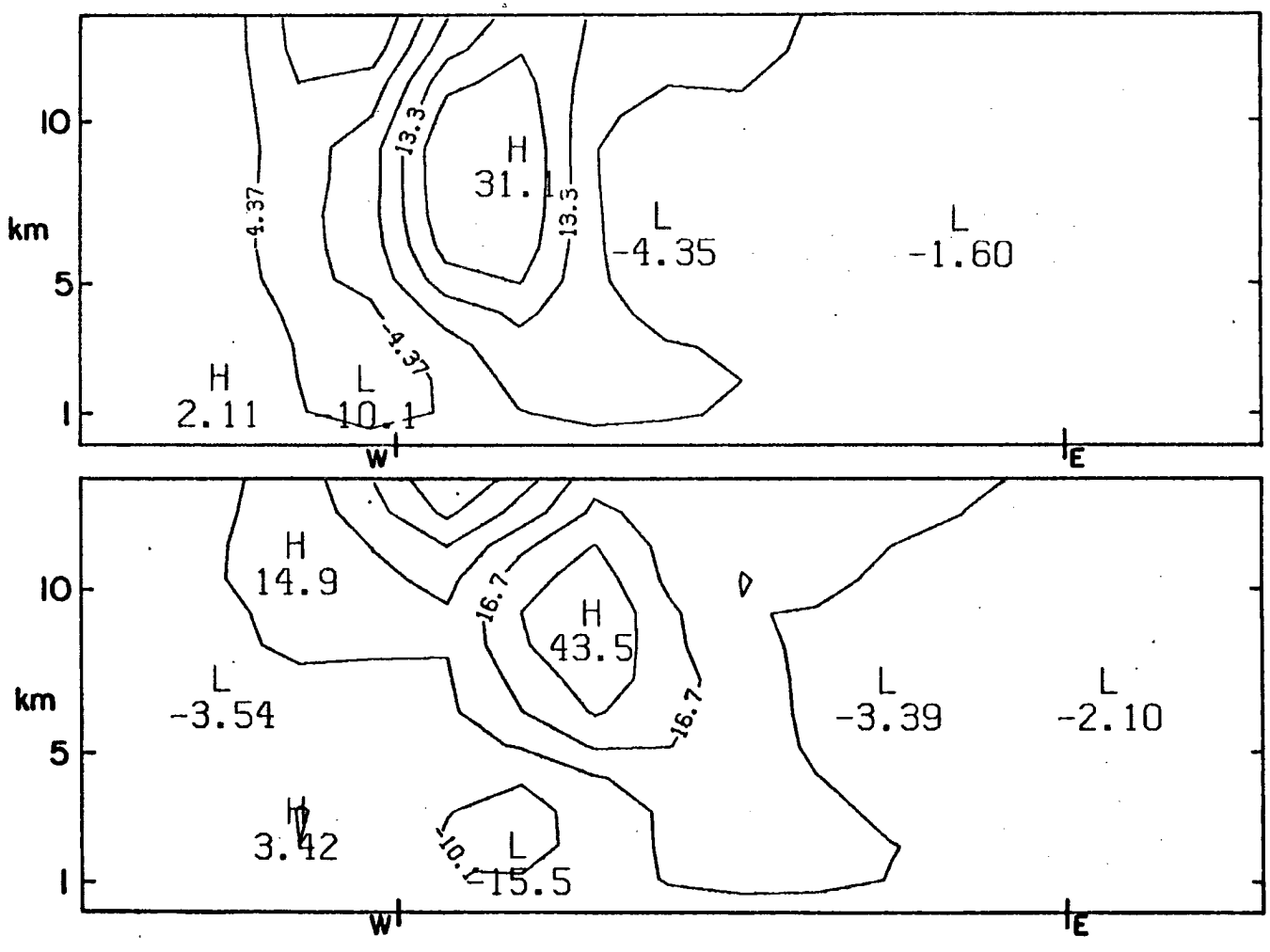


Figure 5-6. The model produced vertical velocities (cm/s) at 4 PM around 10 km (top) and 1 km (bottom) for the Drier-Sounding experiment.

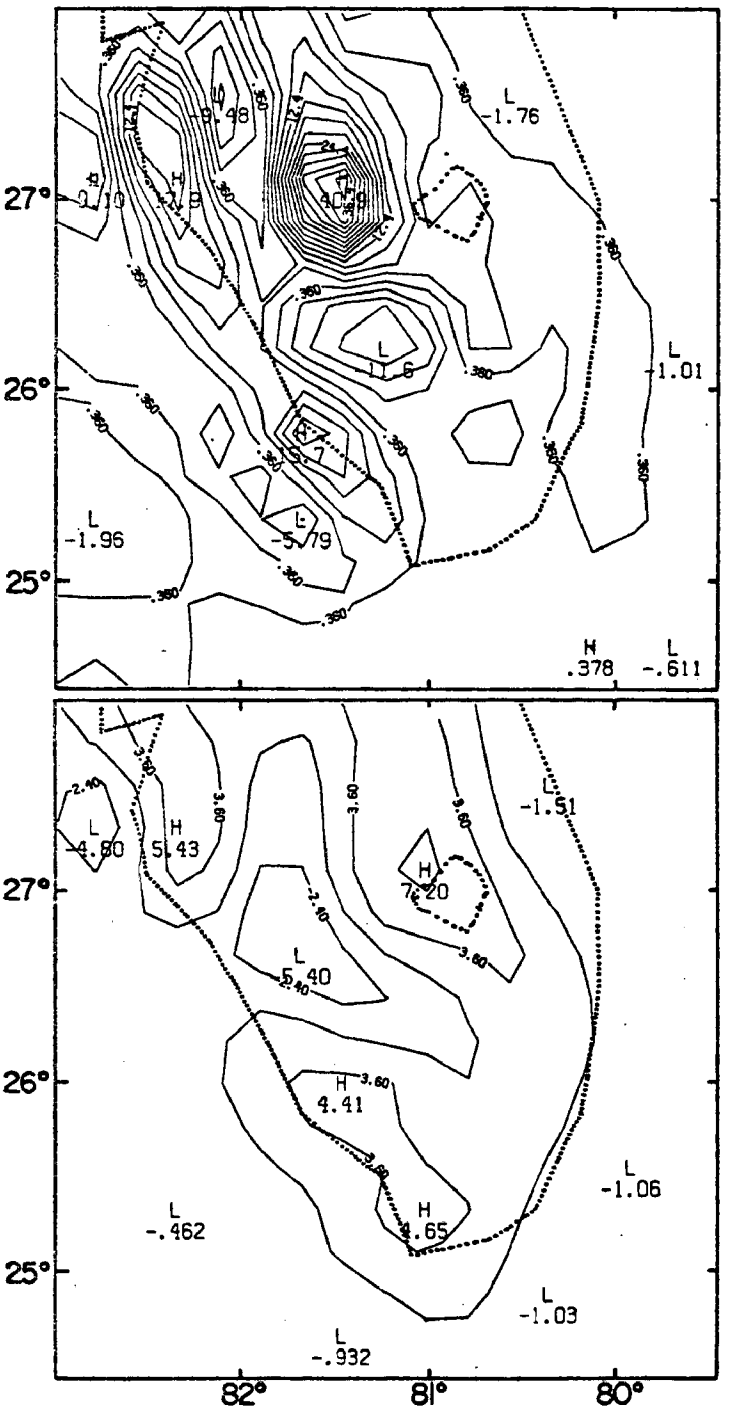


Figure 5-7. Vertical velocities (cm/s) at 3 PM (top) and 4 PM (bottom) on the XZ-cross section for the Drier-Sounding experiment.

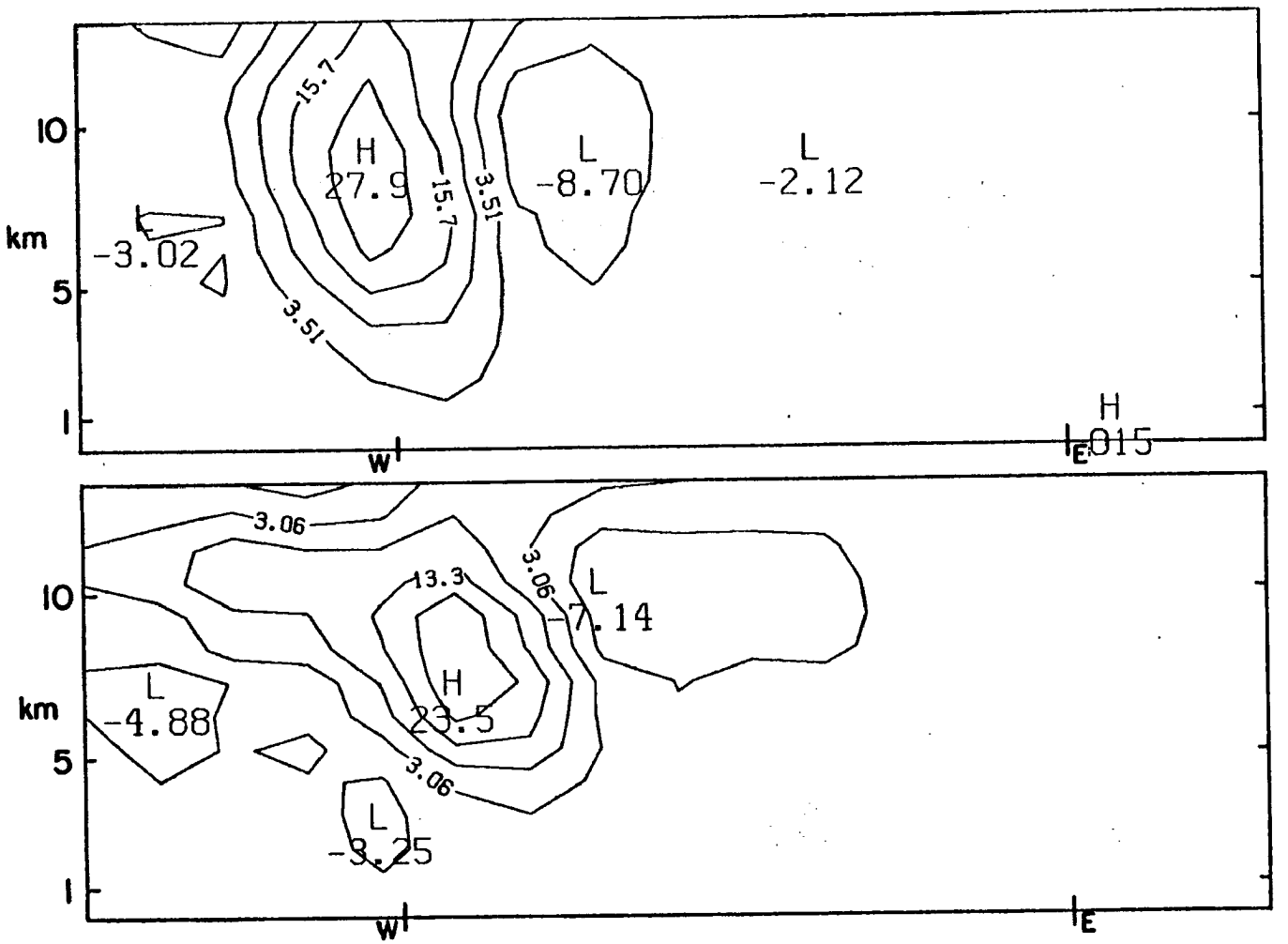


Figure 5-8. Vertical velocities (cm/s) at 3 PM (top) and 4 PM (bottom) on the XZ-cross section for the No-Downdraft experiment.

Figure 5-9 indicates that without the downdraft effect the convective development is primarily along the west coast (that is, within the original sea breeze convergence zone). Since surface cooling due to convective downdrafts is absent, the boundary layer heat fluxes within the sea breeze convergence zone remain relatively strong, thereby maintaining the deep cumulus convection within the sea breeze convergence zone rather than propagating away from this region as occurred in the control experiment.

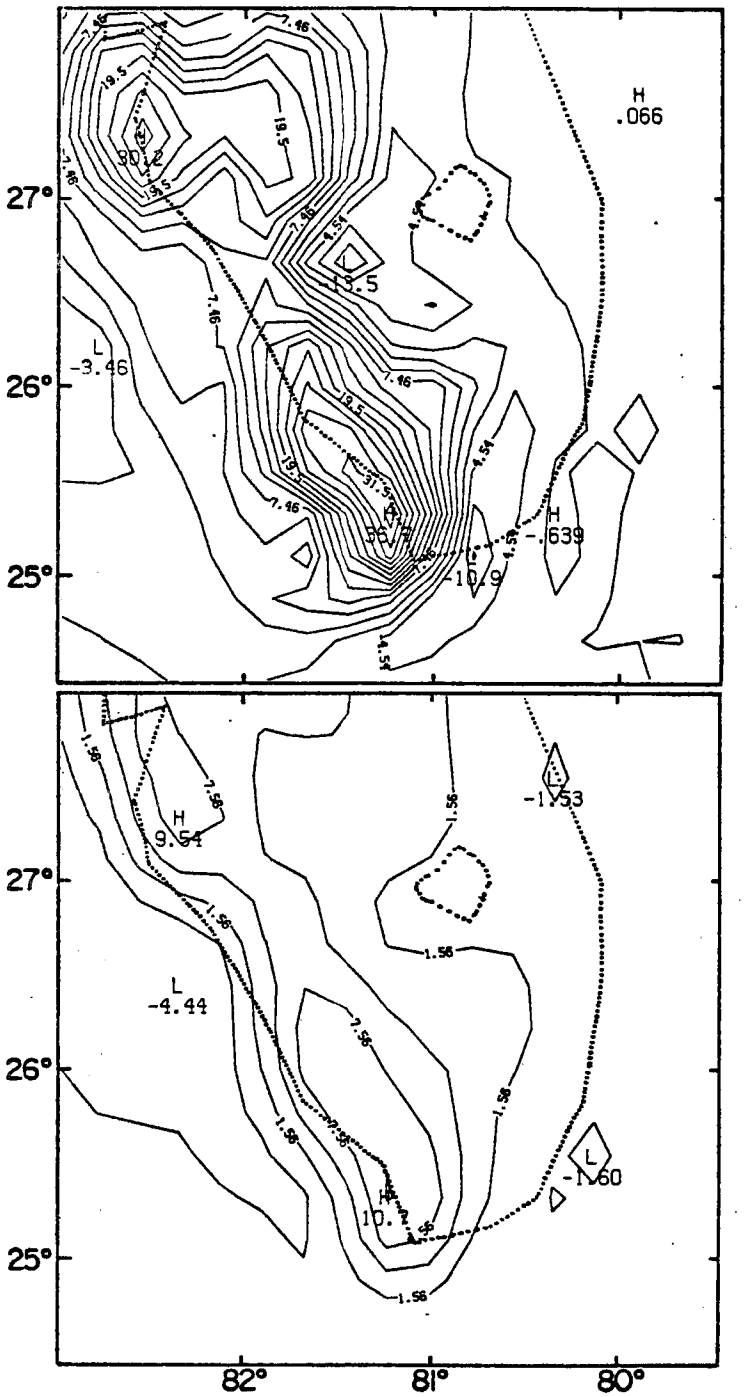


Figure 5-9. The model produced vertical velocities (cm/s) at 4 PM around 10 km (top) and 1 km (bottom) for the No-Downdraft experiment.

# Chapter 6

# CONCEPTUAL MODEL OF FLORIDA'S SEA BREEZE - CUMULONIMBUS INTERACTIONS

## 6-1. Introduction

The evolution of deep cumulus convection in Florida's sea breeze environment has been discussed in Chapter 4. It was indicated that two important processes are necessary conditions for Florida's summertime deep convection to develop: i) the ascent and preconditioning and continuous moisture enrichment of the boundary layer by the sea breeze; and ii) the moisture enrichment and vertical motion resulting from boundary layer pressure gradients generated due to the convective downdraft cooling. Since these two mechanisms typically have time lags between them, it is important to see how the deep convective activities interact with the sea breeze circulation at different stages of the convective lifetime.

From the illustrations shown in Chapter 4, we see that the downdraft produces boundary layer cooling which becomes relatively significant (i.e., covers a significant fraction of the original sea breeze convergence zone) by about 2 PM in the afternoon. The initial deep convection develops around 2 PM. After about 2 PM, the downdraft cooling generates substantial modulations upon the mesoscale environment as well as on subsequent deep convective development. Therefore, for the synoptic background chosen for this study, it seems that 2 PM

is a proper choice as the time separating the two stages: a sea breeze convergence stage; and a convective downdraft cooling stage.

As discussed previously throughout this study, during the mature stage of the convective lifetime the downdraft cooling effect is seen to provide a positive feedback mechanism which enhances the subsequent convection by generating low-level upwind-side upward motion; meanwhile the downdraft tends to stabilize the original convective area by replacing the original boundary layer air with colder air. As discussed in section 4-4, the mid-tropospheric convergence is related to the mesoscale upward and downward motion during the late afternoon. The downward motion acts to decrease the low-level moisture supply from the original warm and moist boundary layer to the upper tropospheric upward motion region (as seen in Fig. 4-4-7(a) during late afternoon). Meanwhile, the surface convergence produced by the downdraft cooling effect tends to propagate the convective system, thereby decreasing the connection between the surface convergence and the original main convective system. The result of these processes, in addition to the diurnal characteristics of the sea breeze circulation, is that the system enters into its decaying stage. In this chapter, 4 PM is chosen as the time separating the decaying stage from the convective downdraft cooling stage.

To obtain qualitatively representative circulation structures for each stage, the control run results are averaged in time over each of the following 2 hour periods:

- sea breeze convergence stage (stage 1): 1200-1400 EST
- convective downdraft cooling stage (stage 2): 1400-1600 EST
- decaying stage (stage 3): 1600-1800 EST.

After a brief discussion of each stage, conceptual models will be used for each of the three stages, which are derived from the control run result, for the purpose of showing the sea breeze-deep cumulus convective interactions for the summertime Florida environment.

## 6-2. Conceptual Models for the Three Stages

### 6-2-a. Sea Breeze Convergence Stage

Figure 6-1 shows the horizontal divergence on the XZ-cross section for stage 1. We see that the main feature at this stage is that the sea breeze circulation provides horizontal convergence near the west coast. Due to this mesoscale convergence, the induced moisture supply (seen in Fig. 6-2) provides a favorable environment for the embedded deep cumulus convection to develop. Figure 6-3 shows that the sea breeze induced convective effects generate upward motion primarily along the west coast (i.e., within the sea breeze convergence zone).

Figure 6-4 shows that in the sea breeze convergence stage, the maximum surface convergence region (along the west coast, as shown in Fig. 6-4(a)) coincides with the maximum surface vorticity region (Fig. 6-4(b)). As discussed in Orlanski and Ross (1984), this indicates that the feedback effect produced by the embedded deep convection is to enhance the mesoscale upward motion generated by the original sea breeze convergence.

Figure 6-5 shows the conceptual model for the sea breeze-convective interaction at stage 1. We see that the interrelationship at this stage is such that the embedded convection is supported by the direct heat and moisture supply provided by the sea breeze convergence. Along the west coast, the vertical motion associated with the original

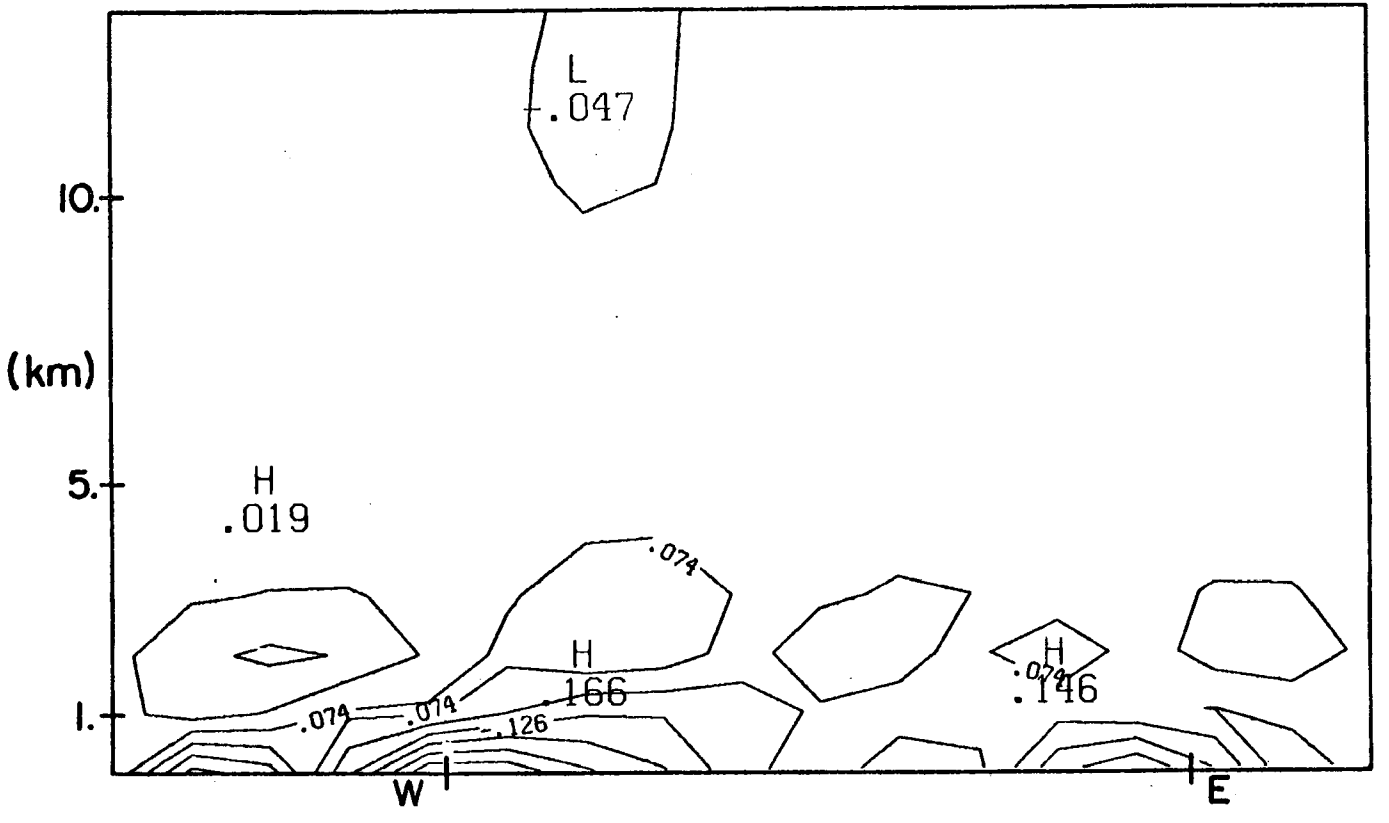


Figure 6-1. The time averaged horizontal divergence ($10^{-4}$ $s^{-1}$) on the XZ-cross section for the Stage-1 (over the time period of 1200-1400 EST).

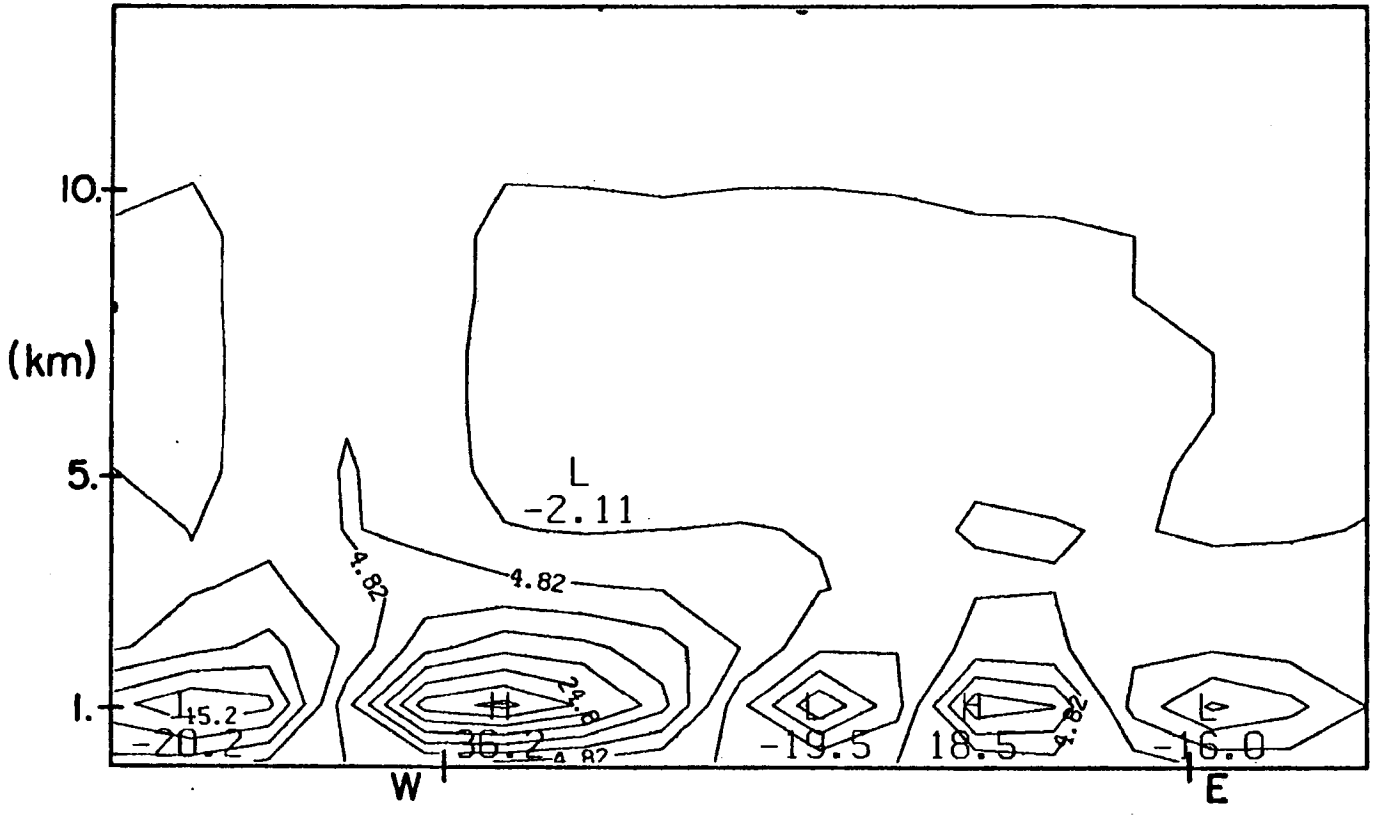


Figure 6-2. The time averaged moisture flux term (vertical velocity times specific humidity) on the XZ-cross section for the Stage-1 (over the time period of 1200-1400 EST).

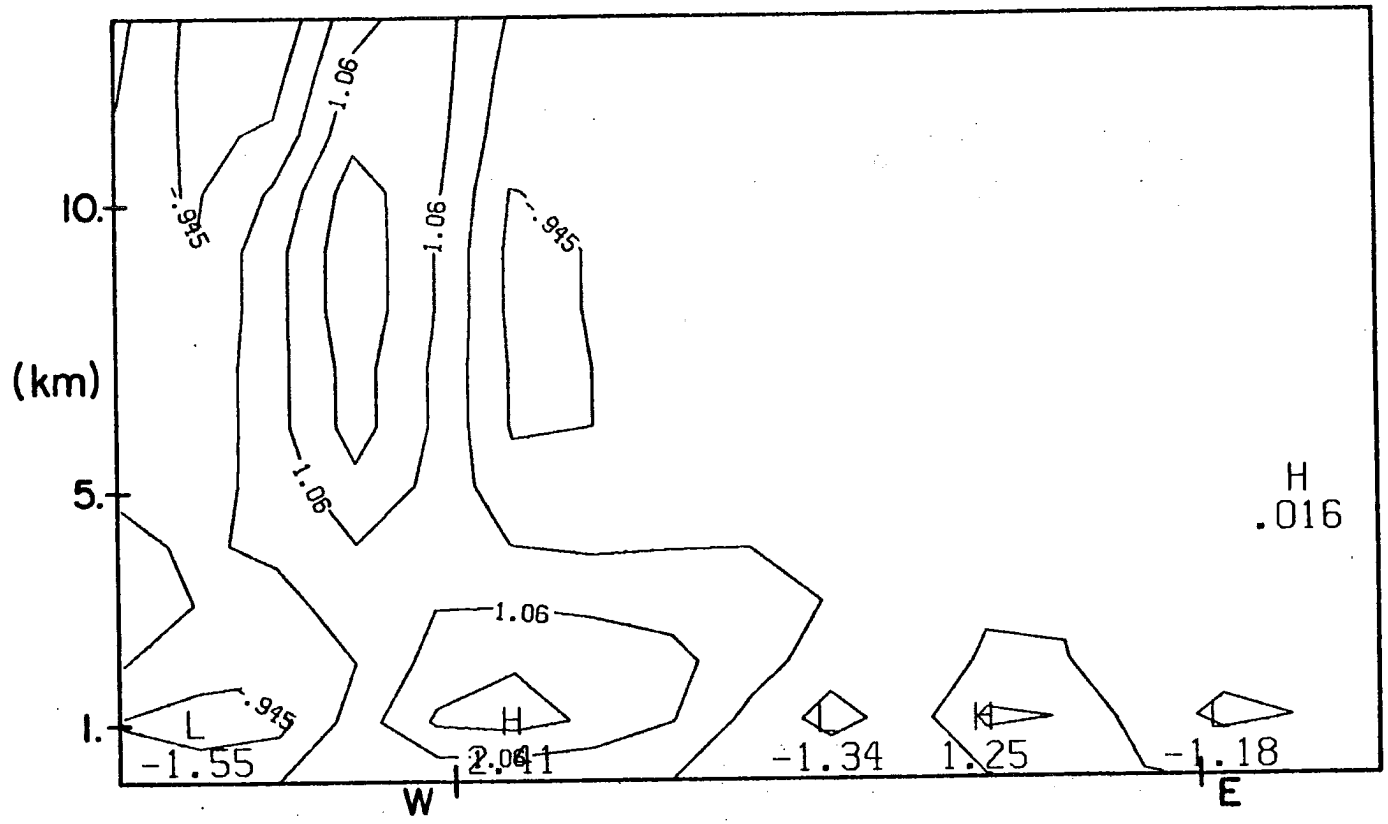


Figure 6-3. The time averaged vertical velocity (cm/s) on the XZ-cross section for the Stage-1 (over the time period of 1200-1400 EST).

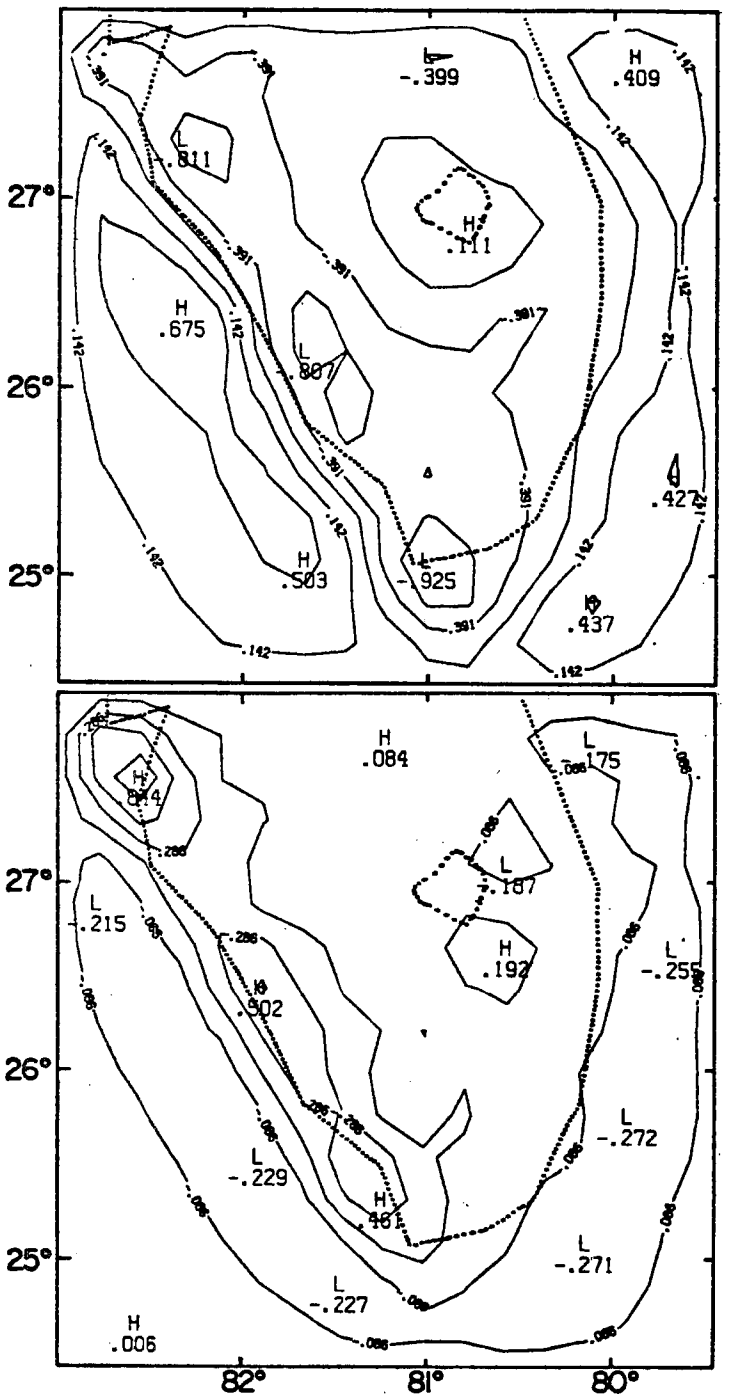


Figure 6-4. The Stage-1 horizontal divergence ($10^{-4}$ $s^{-1}$, top) and vertical vorticity ($10^{-4}$ $s^{-1}$, bottom) at 9 m.

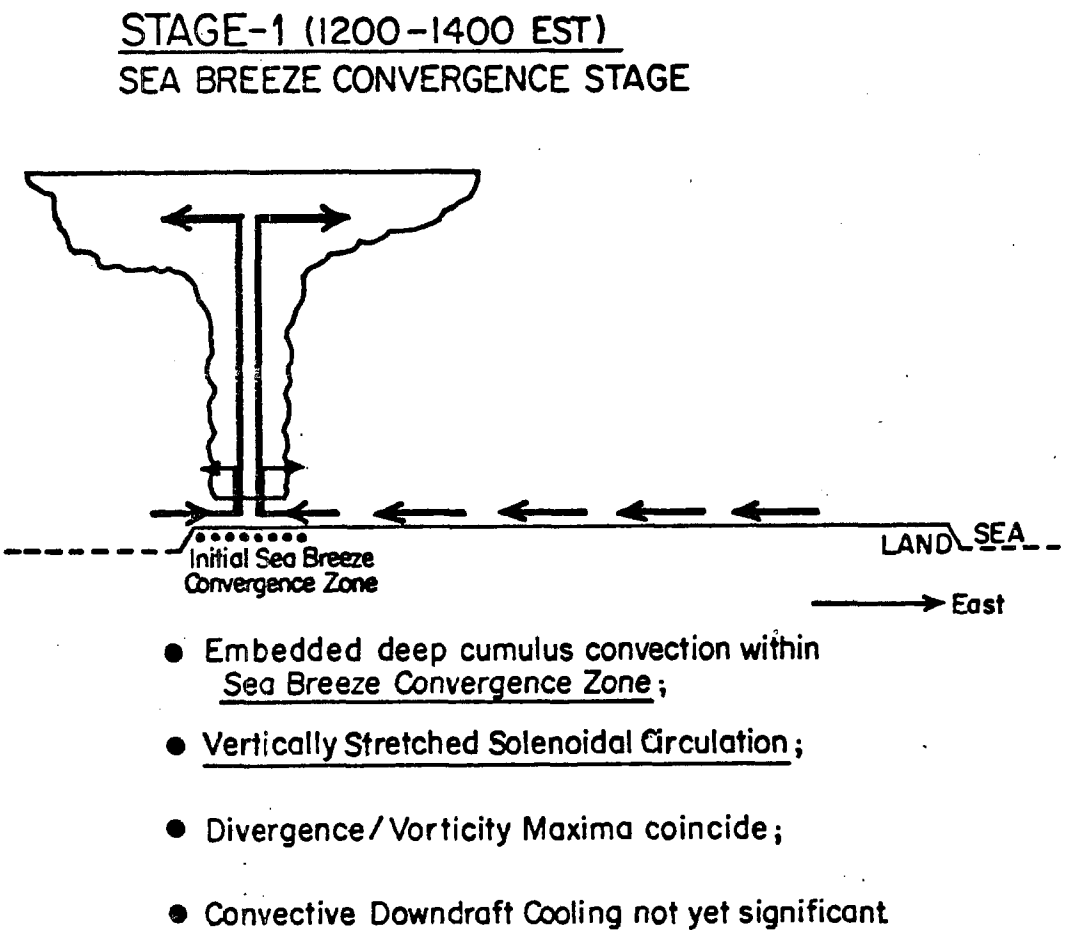


Figure 6-5. The conceptual model for the Stage-1's sea breeze-deep convective interactions over the southern Florida peninsula during synoptically undisturbed days.

sea breeze circulation is enhanced and extended over a much thicker layer throughout the troposphere due to the convective effect.

6-2-b. Convective Downdraft Cooling Stage

Figure 6-6 shows the two-hour averaged horizontal divergence on the XZ-plane for the time period of 1400-1600 EST (stage 2) during the control run. We see that this divergence structure differs from its previous state (Fig. 6-1) primarily in two aspects: i) the surface convergence advances to the surface upwind side; and ii) divergence and convergence are generated in the upper and middle troposphere, respectively. The mesoscale moisture supply (Fig. 6-7) has its peak in the low-level upwind-side upward motion region, indicating the importance of the surface convergence produced by the downdraft cooling effect. Figure 6-7 also shows that the original west coast convergence zone has stabilized, to some extent, due to the downdraft cooling. The vertical motion field at stage 2 is shown in Fig. 6-8. In this stage, the convective downdraft cooling plays an important role to accentuate the surface convergence, thereby enhancing the subsequent convective development, while stabilizing the original convective area.

Figure 6-9 shows that during the convective downdraft cooling stage, the maximum surface convergence region is not as regular as it is in stage 1. Rather, the locations of the surface convergence maxima are determined by the combined forcing of the surface sea breeze flow and the downdraft cooling effect (as discussed in Chapter 4). As seen in Fig. 6-9(a), one of the surface convergence maximum has propagated inland, which is on the low-level upwind-side of the corresponding surface vorticity maximum (Fig. 6-9(b)). As discussed in Orlanski and Ross (1984), such a phase shift between the surface convergence maximum

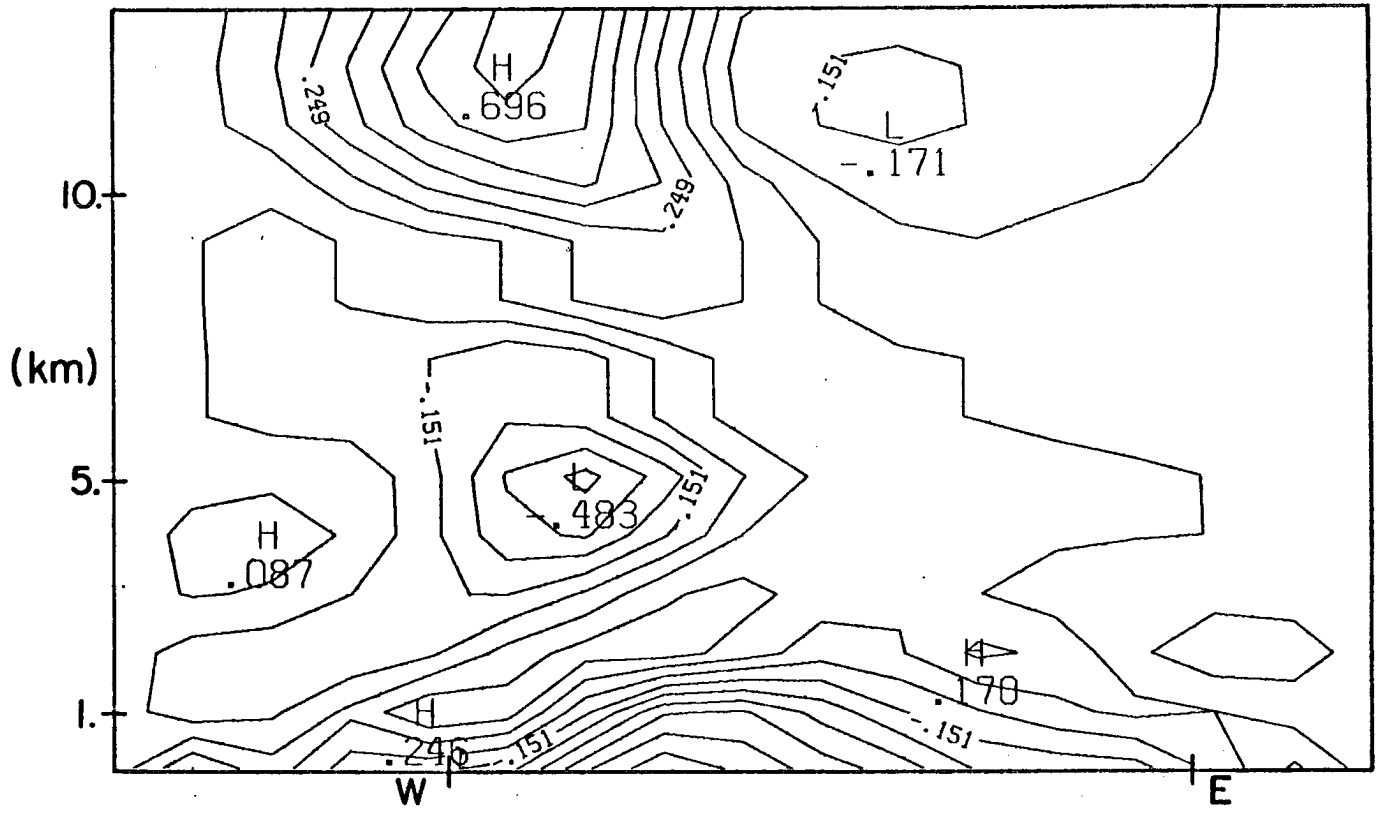


Figure 6-6. The time averaged horizontal divergence ($10^{-4}$ $s^{-1}$) on the XZ-cross section for the Stage-2 (over the time period of 1200-1400 EST).

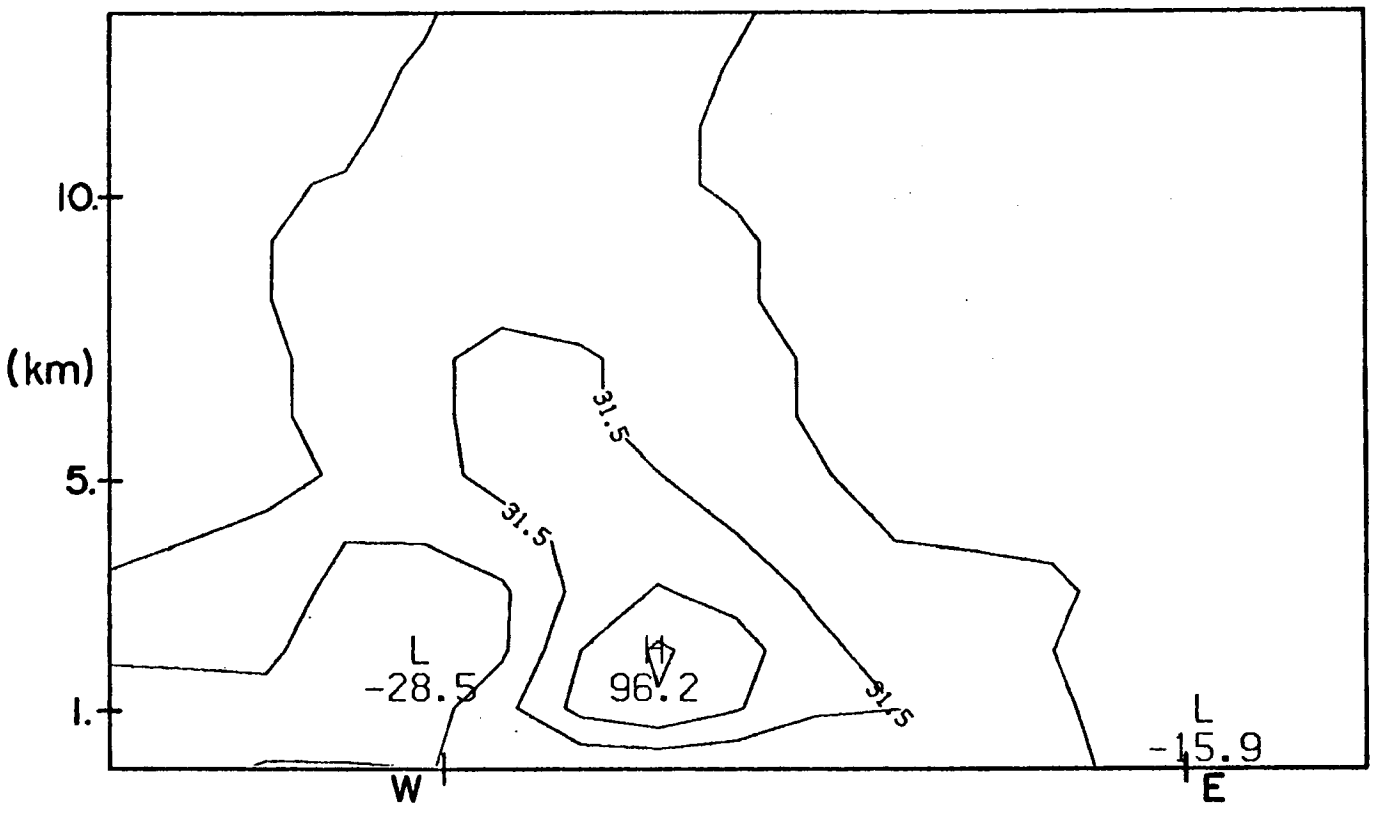


Figure 6-7. The time averaged moisture flux term (vertical velocity times specific humidity) on the XZ-cross section for the Stage-2 (over the time period of 1200-1400 EST).

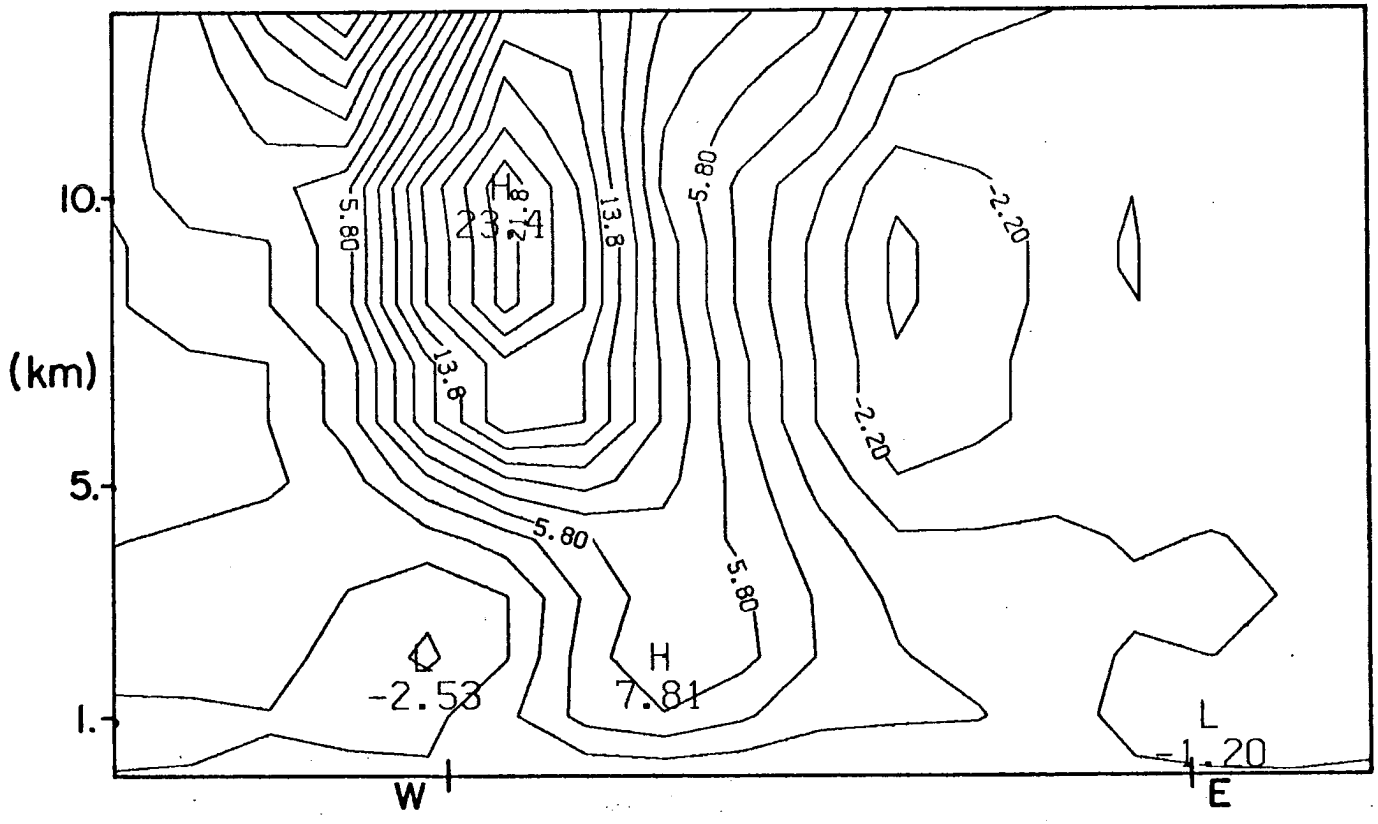


Figure 6-8. The time averaged vertical velocity (cm/s) on the XZ-cross section for the Stage-2 (over the time period of 1200-1400 EST).

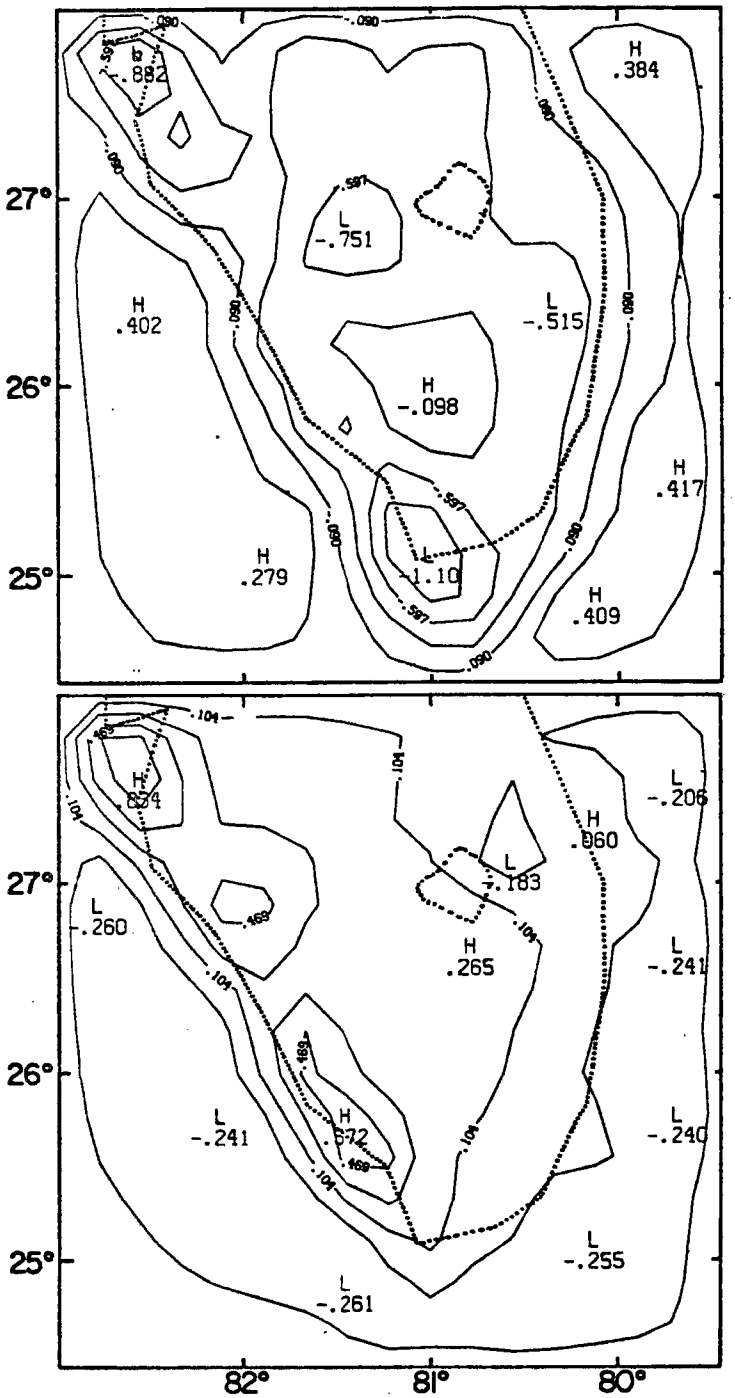


Figure 6-9. The Stage-2 horizontal divergence ($10^{-4}$ $s^{-1}$, top) and vertical vorticity ($10^{-4}$ $s^{-1}$, bottom) at 9 m.

and surface vorticity maximum indicate that the convergence no longer acts to strengthen the original convective zone (or frontal zone in their case). Instead, the original convective system is in a quasi-steady state during this stage.

Figure 6-10 shows the conceptual model for the sea breeze-convective interaction at stage 2. To illustrate the convective propagation, this stage is divided into two sub-stages as shown in Fig. 6-10. We see that the most important feature is that the convective system is supported by the boundary layer moisture provided by the low-level upwind-side upward motion which is generated due to the combination of the sea breeze flow and the downdraft cooling effect. Meanwhile, due to both the new convective growth on the low-level upwind-side and the stabilization underneath the old convection, the convective system propagates toward the upwind direction. The result of both the low-level downdraft cooling effect and the enhanced mid-tropospheric convergence is to produce a four-cell solenoidal circulation pattern, which differs from that in stage 1 because of the effect of the convective downdrafts.

6-2-c. Decaying Stage

The horizontal divergence structure on the XZ-plane for stage 3 is shown in Fig. 6-11. Comparing Fig. 6-11 with Fig. 6-6, we see that deep-convective systems have produced more complicated perturbations in the environmental horizontal divergence field at stage 3 than in stage 2. The most important feature is that the mid-tropospheric convergence has strengthened and produces a cooling and drying effect upon the lower tropospheric. The drying effect is clearly seen in Fig. 6-12, in which we see that the

STAGE-2 (1400-1600 EST) Part I

CONVECTIVE DOWNDRAFT COOLING STAGE (I)

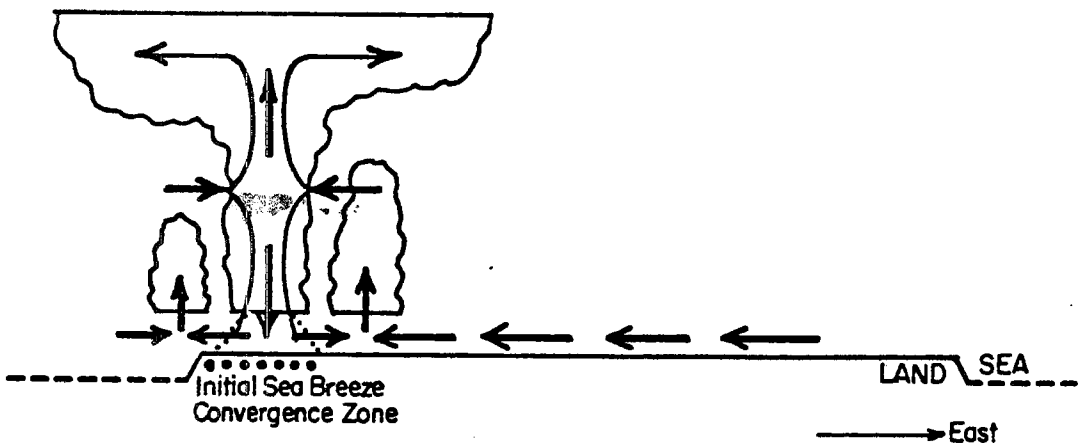


- Downdraft Cooling becomes significant;
- Outflow + Sea Breeze Flow—— CONVERGENCE;
- Stabilization;
- Mesoscale ascent on the upwind side;
- MOISTENING (Upwind Favorable Environment);
- "phase shift"

Figure 6-10(a). The conceptual model for the Stage-2's sea breeze-deep convective interactions over the southern Florida peninsula during synoptically undisturbed days.

STAGE-2 (1400-1600 EST) Part II

CONVECTIVE DOWNDRAFT COOLING STAGE (II)

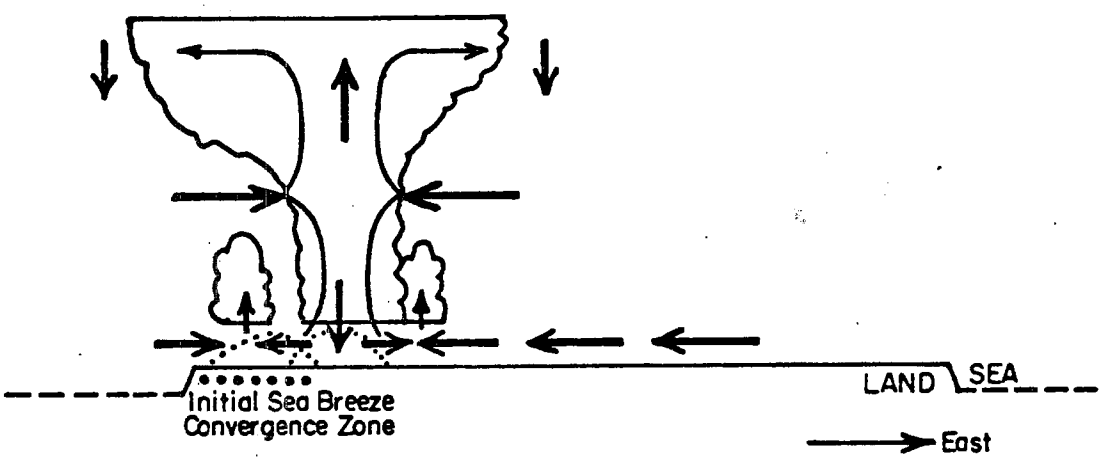


- Stabilization + New Favorable Environment Upwind —— Upwind Propagation;
- Mid-Tropospheric Convergence
- "Four-Cell" Vertical Circulation
- Mesoscale Upward/Downward Motions Initiated
- Divergence at Surface

Figure 6.10(b).

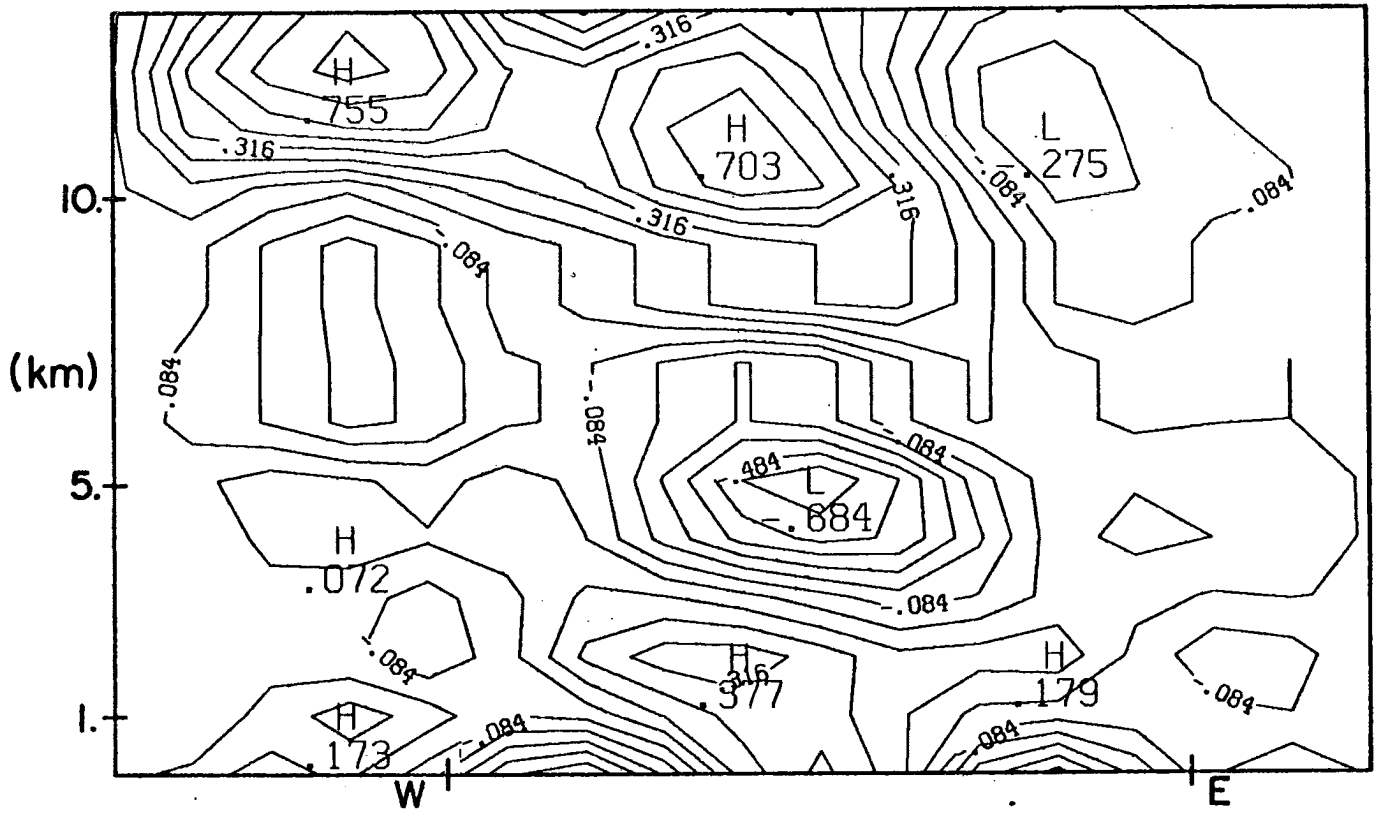


Figure 6-11. The time averaged horizontal divergence ($10^{-4}$ $s^{-1}$) on the XZ-cross section for the Stage-3 (over the time period of 1200-1400 EST).

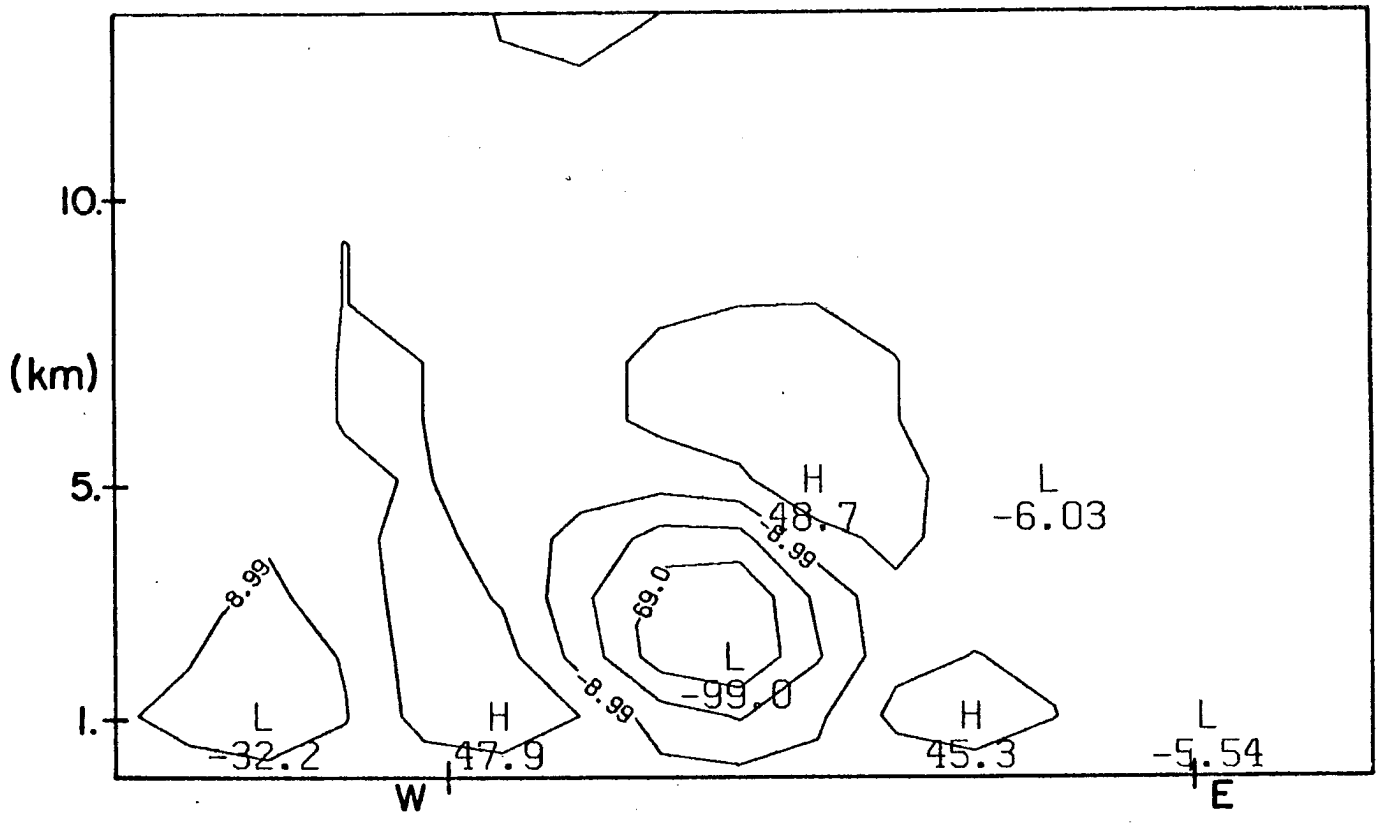


Figure 6-12. The time averaged moisture flux term (vertical velocity times specific humidity) on the XZ-cross section for the Stage-3 (over the time period of 1200-1400 EST).

stabilized old convection is associated with negative moisture fluxes in the lower troposphere. Meanwhile, new upward moisture fluxes occur over the regions surrounding the old convective system, but with significantly smaller values than that during stage 2 (shown in Fig. 6-7). This indicates that further deep cumulus convection is not expected. Figure 6-13 shows that relatively large upward velocities are only found in the upper troposphere.

Finally, Fig. 6-14 shows that during the decaying stage there are primarily mesoscale motions in response to the combination of the upper-tropospheric heating, mid-tropospheric convergence and the lower-tropospheric downdraft cooling effect. Weaker surface convergences are still generated surrounding the old convective system. However, since the sea breeze flow is controlled by the diurnal solar cycle and surface solar heating has diminished, further deep cumulus convective development is not expected during stage 3.

## 6-3. A Comparison between Moist and Dry Sea Breeze Energetics

The kinetic energy budget (KEB) components (introduced in Chapter 2) are computed for the dry sea breeze simulation and the moist sea breeze simulation (control run). Figure 6-15 shows that at 3 PM, the moist sea breeze kinetic energy budget differs from the dry sea breeze budget primarily in two aspects:

- for the dry case, in the surface kinetic energy budget, the pressure gradient term and the turbulence dissipation term are close in magnitude but with a net KE generation at surface. A similar pattern is seen for the moist case, however with smaller magnitudes of the two components (about 25

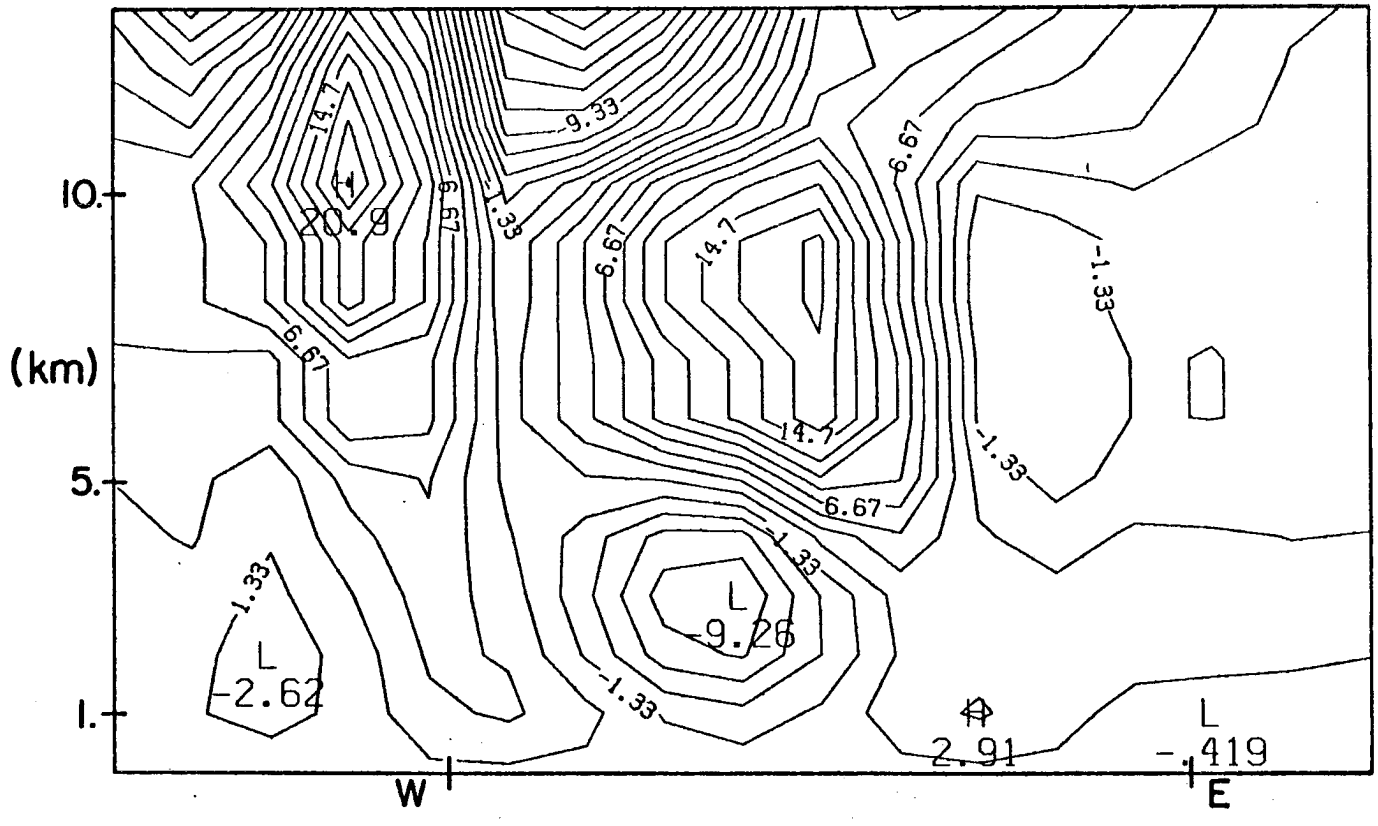


Figure 6-13. The time averaged vertical velocity (cm/s) on the XZ-cross section for the Stage-3 (over the time period of 1200-1400 EST).

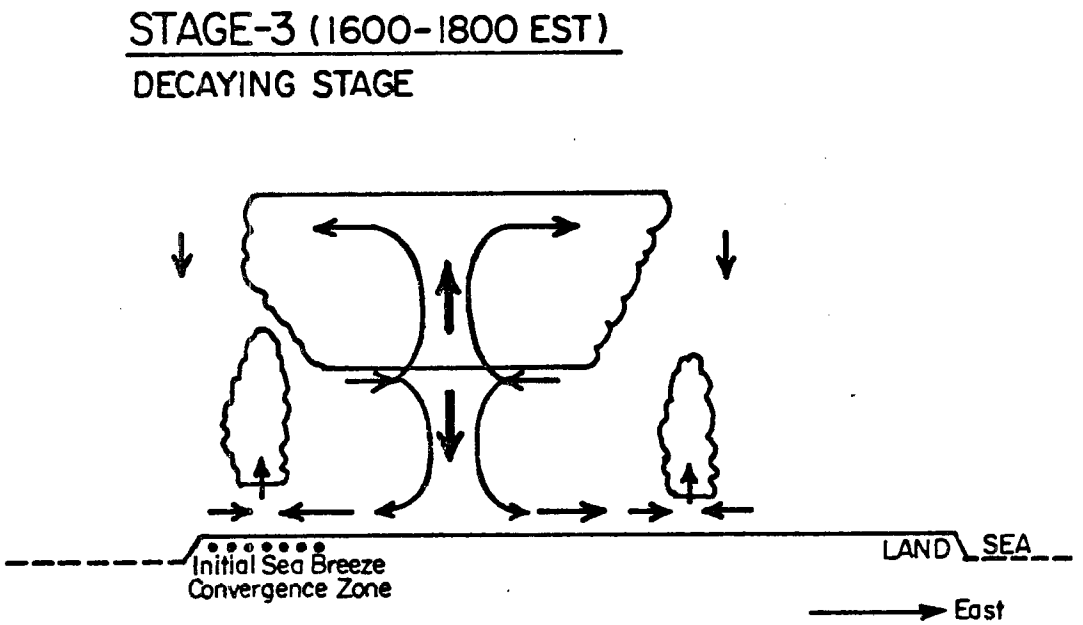


Figure 6-14. The conceptual model for the Stage-3's sea breeze-deep convective interactions over the southern Florida peninsula during synoptically undisturbed days.

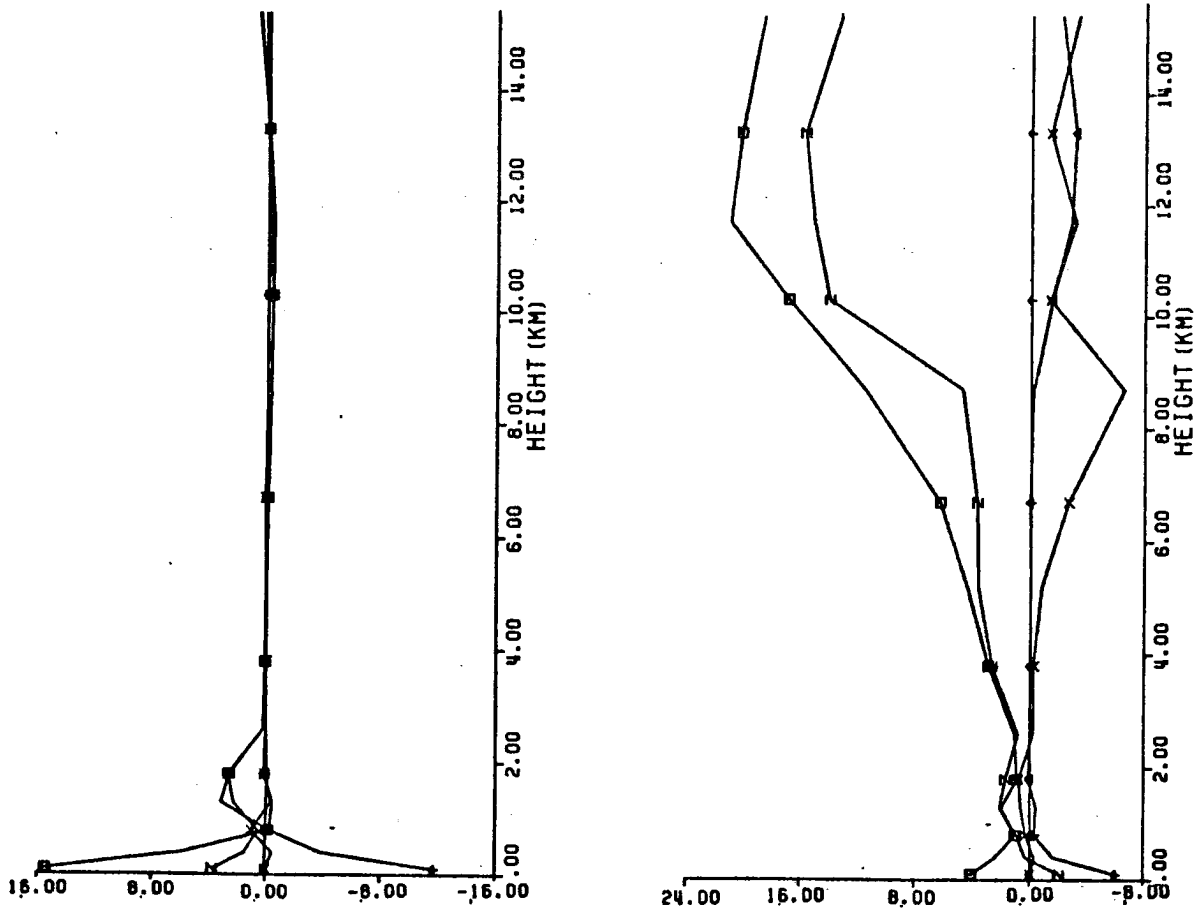


Figure 6-15. Vertical profiles of the horizontally-integrated kinetic energy budget components (watt/$m^2$/km) at 3 PM for the dry sea breeze run (left) and the moist sea breeze run (right). The different curves are explained in the figure.

percent of the corresponding dry components' values) and a net KE sink at surface.

- The dry KEB components are negligible in the upper troposphere, while those of the moist case have relatively large values in the layer between about 8 km and 14 km (i.e., upper-level wind perturbations generated in response to the deep cumulus convection, around 12 km).

The direct contribution of deep cumulus convection upon the grid-scale horizontal kinetic energy budget is calculated using the procedure described in Section 3-6. The resultant vertical profile of this term is shown in Table 3-12, which can be directly compared with other hydrostatic KEB components. Due to the area-weighted averaging (Section 3-6), we see that this term is much smaller than the pressure gradient term (since the updraft areas are generally much smaller than the grid areas throughout the cloud layer; which is between about 1 km and 13 km). The only exception is the subcloud layer (when downdrafts are well developed). Since downdrafts have been observed to replace boundary layer air over much larger areas than the area covered by deep cumulus clouds, it can produce KE variabilities as large as those of the grid-scale pressure gradient term.

The major KEB generation component in both the dry and moist budgets is the pressure gradient term. For this reason, and because this term has been related to the surface downdraft cooling effect, this term is further examined by comparing its vertical structures in the dry and the moist simulations. Rather than using results at individual times, time averaged values (i.e., the two-hour averages of the three stages introduced in the last section) are used.

Comparing Fig. 6-16 (dry sea breeze run) with Fig. 6-17 (moist sea breeze run), we see that the major difference between the dry and moist sea breeze energetics is that the deep convective effects produce significant horizontal pressure perturbations in the upper troposphere. That is, the shallow solenoidal circulation associated with the dry sea breeze flow (without cumulus convection) is extended upward to a much thicker layer due to the deep cumulus convective effects. For the dry case, the windward (east) coast remains to be the major KE source region throughout the afternoon. This indicates that the dry sea breeze circulation obtains its kinetic energy primarily from the pressure gradients generated along the coastal area due to the surface heating contrast (i.e., a flow toward lower pressure of the heated land is associated with a net KE generation).

For the sea breeze circulation when the deep cumulus convection is included, we see from Fig. 6-17 that the major KE source region is around the upper tropospheric mesohigh associated with the vertically stretched solenoidal circulation caused by the deep convective effect. The down-gradient flow away from the mesohigh region produces horizontal accelerations, while a KE sink is found on the upwind side of the convective region. The surface KE generation and dissipation are reduced in their relative contributions to the net KE balance over the domain in this moist simulation.

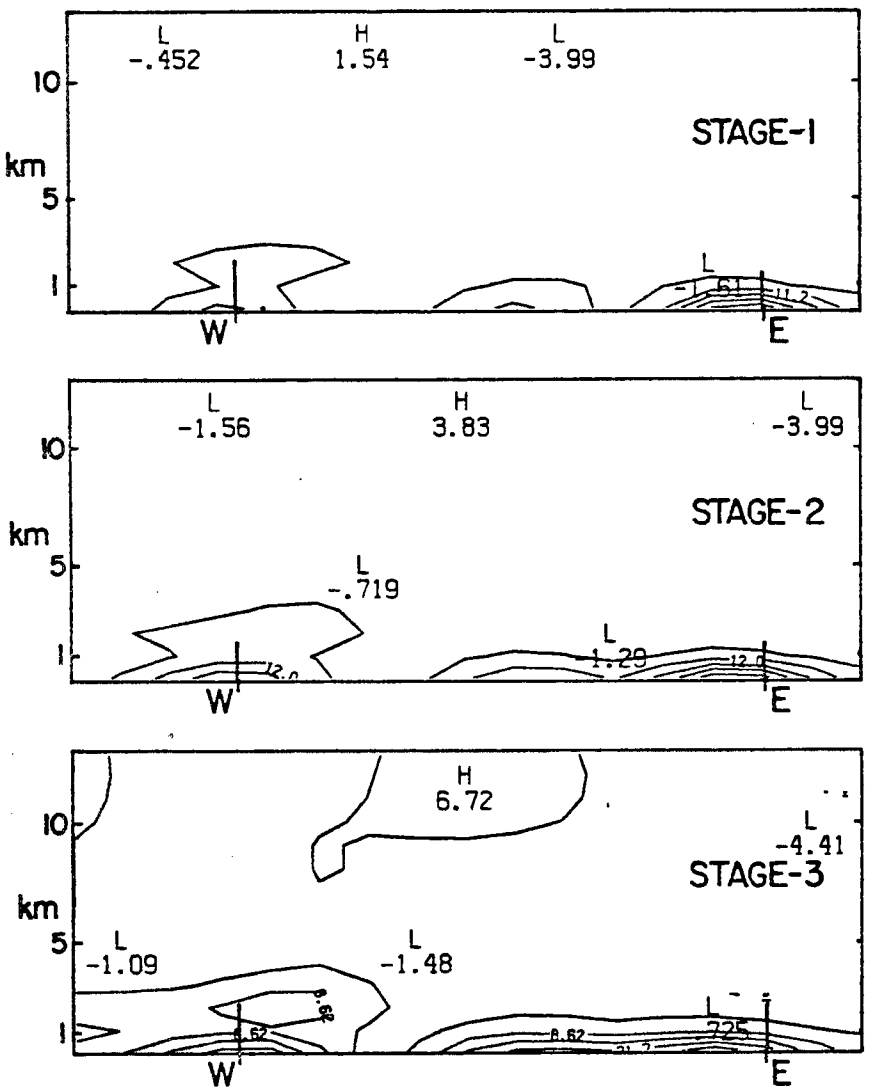


Figure 6-16. The horizontal pressure gradient term in the kinetic energy budget equation on the XZ-cross section for the three stages of the dry sea breeze simulation.

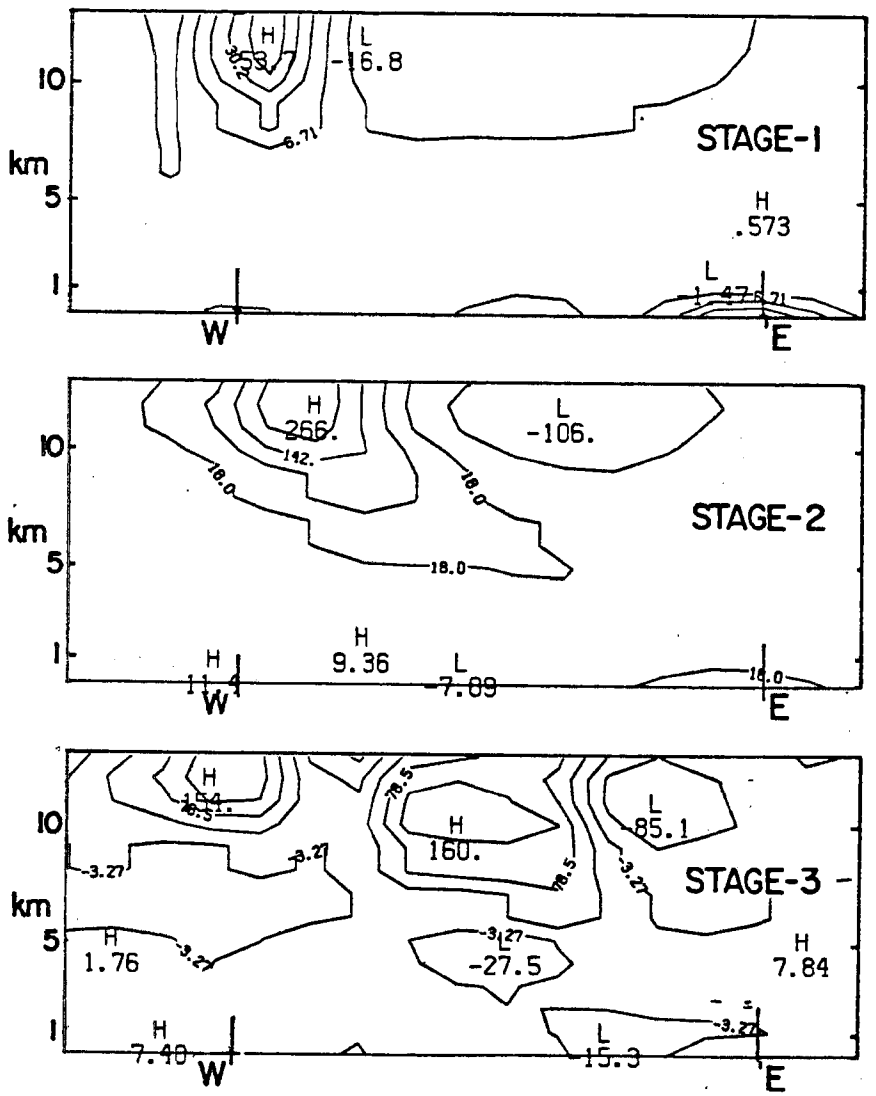


Figure 6-17. The horizontal pressure gradient term in the kinetic energy budget equation on the XZ-cross section for the three stages of the moist sea breeze simulation.

# Chapter 7

## SUMMARY AND CONCLUSIONS

Florida's deep cumulus convective effects upon the mesoscale sea breeze environment are investigated using a numerical approach validated by observations. The mesoscale hydrostatic primitive-equation model, originally developed by Pielke (1974) for simulating the Florida dry sea breeze circulation, is utilized together with a cumulus parameterization modified from that of Fritsch and Chappell (1980) for investigating the Florida sea breeze-deep convective interactions.

The original Fritsch and Chappell parameterization is tested and modified so as to incorporate the observed Florida convective characteristics as documented in Byers and Braham (1949), Simpson et al. (1980), among others. The obtained parameterization is examined with respect to its conservation properties and sensitivities to some of the inherent assumptions in the parameterization. Modifications upon a dry boundary layer due to deep cumulus convection are included. The effect of parameterized subgrid-scale deep cumulus actual effect on the hydrostatic kinetic energy budget equation is analyzed.

The sea breeze simulation incorporating the deep cumulus convective effects is validated by being compared with observations. The observational data used for this purpose includes long period, high resolution manually digitized radar (MDR) composite analyses; radar echo frequency statistics; satellite image composites binned according

to synoptic categories; and surface radar rainfall hourly maps, for the southern Florida environment on a specific day.

The simulation results are found to be able to produce in general the climatologically observed patterning of deep cumulonimbus over the Florida environment. For the particular day chosen for initiating the simulations, the surface hourly radar rainfall pattern is not simulated in detail, although the statistically most favored time and location of the deep convective developments are generally within the model predicted convective regions. The reason for not simulating the surface rainfall distributions is due in part to the fact that using 22 km as the horizontal grid spacing, the effect of Lake Okeechobee is not well simulated. The effect of Lake Okeechobee is associated primarily with the surface divergence surrounding the lake, such that convergences can be generated to the east or southeast of the lake as a result of the east coast sea breeze over the Florida peninsula. During afternoons of typical sea breeze days with large scale easterly or southeasterly winds, however, it is often observed that the majority of the deep convective developments are along the southwest and west coastal regions. Therefore, the absence of sufficient resolution of the lake effect does not significantly degrade the simulation results nor the physical interpretation since the model is able to produce the west coast deep convective activities (as shown in the validation in Chapter 4).

Based on the three-dimensional simulations of the sea breeze-deep cumulus convective interactions during the afternoon, it is concluded that boundary layer cooling caused by deep cumulus convective-downdrafts plays an important role in the convective-environmental interrelationships.

It is well known that deep convective downdrafts produce surface outflow, thereby inducing and enhancing low-level convergence in the immediate mesoscale environment (Byers and Braham, 1949; among others). The downdraft induced merging process has been recognized as one of the most important mechanisms for generating the observed Florida mesoscale organizations of convection (Simpson et al., 1980; Lopez et al., 1984). Intersecting surface flows generated by the downdrafts have been observationally associated with subsequent deep convection (Purdom, 1986).

However, thus far in the literature, it has not been documented as to the downdraft effects upon the diurnally varying sea breeze circulation and the peninsula-scale responses throughout the troposphere.

This is presumably due, in part, to the difficulties involved in conducting a peninsula-scale observation which include simultaneously the convective downdraft cooling effect as well as the sea breeze forcing. A convective parameterization approach, such as that utilized in this study, is considered as an acceptable tool for investigating the Florida convective-environmental interactions. This is because the mid/upper troposphere (above about 5-6 km), under synoptically undisturbed situations, is generally not perturbed by the dry sea breeze circulation, therefore the net convective effects can be more easily separated from the background environmental flow.

The main convective-environmental interactions in the Florida peninsula include:

(a) During the early afternoon, cooling by downdrafts has not yet been sufficient to substantially modify the patterning of deep convection. Thus the deep cumulus convection which is

initiated by sea breeze convergence, remains located within the sea breeze convergence zone. The cumulonimbus effect during this stage is primarily to stretch vertically the original shallow solenoidal circulation (generated by the dry sea breeze flow) into a much greater depth through the troposphere, thereby further enhancing the sea breeze convergence.

(b) Following the onset of more extensive downdraft cooling, the convective-environmental interrelationship becomes more involved. The downdraft-induced surface cooling is found to generate a horizontal pressure gradient near the surface such that a low-level upward velocity maximum on the upwind side (with respect to low-level inflow) of the deep convective system occurs. At the same time an upper tropospheric upward motion maximum and a lower tropospheric downward motion maximum occurs in the area of the initial deep convection. Such a structure is similar to that of a mid-latitude squall line system observed by Ogura and Liou (1980).

This "four-cell" vertical circulation pattern is found as a result of both the convective heating and the downdraft cooling. The low-level upwind-side upward motion is important to the subsequent convective developments in that it provides the mid and lower tropospheric moistening, as well as provides a continuous moisture supply for the convection particularly on the upwind side where sea breeze inflow is present. The combination of the surface sea breeze flow and the downdraft cooling effect is found necessary for the continuous development and inland propagation of the deep convective system.

(c) The decaying stage of the sea breeze-deep convective interaction is associated with both relatively significant mesoscale downward motion caused by the mid-tropospheric convergence and the surface divergence (associated with the deep cumulus convection) and the diurnal nature of the sea breeze circulation. Significant upward motions are found only in the upper troposphere in this stage, although convective precipitation is still existing which is related to the remnant of the surface convergences surrounding the main convective system.

Sensitivity experiments have been performed considering the intensity of the prevailing synoptic-scale wind, the degree of the mid-tropospheric moistening, as well as the effect of neglecting convective downdrafts. Results of these experiments show that the sea breeze-deep convective interrelationship is retained only as long as the convective downdraft is included. This indicates that deep convective-generated downdrafts play a crucial role in the Florida convective-environmental interactions as well as in producing convective upscale feedback effects upon the mesoscale environment.

Summarizing the moist sea breeze simulations performed in this study, the main conclusions are:

(1) The Florida lower-tropospheric storm-generated downdraft substantially modifies the sea breeze circulation through the generation of mesoscale surface pressure gradients as a result of the downdraft cooling.

(2) Three stages can be identified for the sea breeze-convective interrelationships. Stage 1 (sea breeze convergence stage)

is associated with the establishment of coastal sea breeze convergence zones and embedded deep convection which vertically stretches the shallow solenoidal circulation (generated by the dry sea breeze) to much greater depths, thereby further enhancing the sea breeze convergence. Stage 2 (convective downdraft cooling stage) follows the onset of the relatively significant downdraft effects upon the peninsular-scale environment. The combination of the downdraft cooling effect and the sea breeze circulation provides new favorable environments for initiating deep convection. A "four-cell" vertical circulation pattern is formed as a result of the upper-tropospheric divergence, mid-tropospheric convergence, and surface divergence. Stage 3 (decaying stage) is associated with mainly mesoscale weaker upward and downward motions without new deep cumulus convective developments.

## REFERENCES


Anthes, R. A., 1985: Cumulus Parameterization.[1]

Anthes, R. A., and T. T. Warner, 1978: Development of hydrodynamic models suitable for air pollution and other mesometeorological studies. MWR, 106, 1045-1078.

Anthes, R. A., 1977: A cumulus parameterization utilizing a one-dimensional cloud model. Mon. Weather Rev., 105, 270-286.

Arakawa, A., and W. H. Schubert, 1974: Interaction of a cumulus cloud ensemble with the large scale environment. Part I., J. Atmos. Sci., 31, 674-701.

Atwater, M. A., and Brown, P., Jr., 1974: Numerical calculation of the latitudinal variation of solar radiation for an atmosphere of varying capacity. JAM, 13, 289-297.

Barnes, G. M., and M. Garstang, 1982: Subcloud layer energetics of precipitating convection. MWR, 110, 102-117.

Blanchard, D. O., and R. E. Lopez, 1984: Variability of the convective field pattern in South Florida and its relationship to the synoptic flow. NOAA Tech. Mem. ERL ESG-4.

Bolton, D., 1980: The computation of equivalent potential temperature. Mon. Wea. Rev., 108, 1046-1053.

Briere, S., 1985: On the energetics of land-sea breeze circulation as determined from a two-dimensional, third-order turbulence closure model. Centre National de Recherches Meteorologiques.

Brown, J. M., 1979: Mesoscale unsaturated downdrafts driven by rainfall evaporation: A numerical study. J. Atmos. Sci., 36, 313-338.

Burpee, R. W., 1979: Peninsula-scale convergence in the South Florida sea breeze. MWR, 107, 852-860.

Burpee, R. W., and L. N. Lahiff, 1984: Area averaged rainfall variations on sea-breeze days in south Florida. Mon. Wea. Rev., 112, 520-534.


---

[1]Draft of contribution to The Dynamics of Clouds and Mesoscale Meteorological Systems. Volume I. The Dynamics of Clouds by W. R. Cotton and R. A. Anthes, Academic Press (to appear).

Businger, J. A., 1973: Turbulent transfer in the atmosphere surface layer. Workshop in Micrometeorology, Ch. 2. Am. Met. Soc., Boston, Mass.

Byers, H. R., and R. R. Braham, Jr., 1949: The Thunderstorm. U.S. Govt. Printing Office, Washington, D.C., 287 pp. [NTIS PB-234515].

Chang, C. B., D. J. Perkey, and C. W. Kreitzberg, 1982: A numerical case study of the effects of latent heating on a developing wave cyclone. JAS, 39, 1555-1570.

Cooper, H. J., M. Garstang, and J. Simpson, 1982: The diurnal interaction between convection and peninsular-scale forcing over South Florida. MWR, 110, 486-503.

Cotton, W. R., 1975: Theoretical cumulus dynamics. Rev. Geophys. Space Phys., 13, 419-448.

Cotton, W. R., R. A. Pielke, and P. T. Gannon, 1976: Numerical experiments on the influence of the mesoscale circulation on the cumulus scale. JAS, 33, 252-261.

Cotton, W. R., M. A. Stephens, T. Nehrkorn and G. J. Tripoli, 1982: The Colorado State University three-dimensional cloud/mesoscale model-1982. Part II: An ice phase parameterization. J. de Rech. Atmos., 16, 295-320.

Cotton, W. R., and G. J. Tripoli, 1978: Cumulus convection in shear flow three-dimension numerical experiments. JAS, 35, 1503-1521.

Cotton, W. R., P. J. Wetzel, and R. L. McAnelly, 1983: A long-lived mesoscale convective complex. Part II: Evolution and structure of the mature complex. MWR, 111, 1919-1937.

Cunning, J. B. and M. DeMaria, 1986: An investigation of the development of cumulonimbus systems over south Florida. Part I: Boundary Layer Interactions. Mon. Wea. Rev., 114, 5-24.

Cunning, J. B., R. L. Holle, P. T. Gannon, and A. I. Watson, 1982: Convective evolution and merger in the FACE experimental area: mesoscale convergence and boundary layer interaction. JAM, 21, 953-977.

Dalu, G. A. and J. S. A. Green, 1980: Energetics of diabatic mesoscale circulation: a numerical study. Quart. J. R. Met. Soc., 196, 727-734.

Deardorff, J. W., 1974: Three-dimensional numerical study of the height and mean structure of a heated planetary boundary layer. Bound. Lay. Met., 7, 81-106.

Emmitt, G. D., 1978: Tropical cumulus interaction with and modification of the subcloud layer. JAS, 35, 1485-1502.

Frank, W. M., 1983: A review of the cumulus parameterization problem. Mon. Wea. Rev., 111 (to appear).

Frank, W. M., and C. Cohen, 1983: A cumulus paramaterization scheme incorporating subgrid-scale convective forcing. Submitted to the First Conference on Mesoscale Meteorology, May 31-June 3, 1983. Norman, Oklahoma.

Frank, N. L., P. L. Moore, and G. E. Fisher, 1967: Summer shower distribution over the Florida peninsula as deduced from digitized radar data. J. Appl. Meteor., 6, 309-319.

Fritsch, J. M., 1975: Synoptic-mesoscale budget relationships for a tornado producing squall line. Proceedings, 9th AMS Conference on Severe Local Storms, Oct. 21-23, 1975, Norman, Oklahoma, 165-172.

Fritsch, J. M., and C. F. Chappell, 1980: Numerical prediction of convectively driven mesoscale pressure systems. Part I. Convective parameterization. JAS, 37, 1722-1733.

Fritsch, J. M., and R. A. Maddox, 1981: Convectively driven mesoscale weather systems aloft. Part II: Numerical simulation. J. Appl. Meteorol., 20, 20-26.

Fuelberg, H. E., and J. R. Scoggins, 1978: Kinetic energy budgets during the life cycle of intense convective activity. MWR, 106, 637-653.

Fuelberg, H. E., and G. J. Jedlovec, 1982: A synoptic-scale kinetic energy analysis of the Red River Valley Tornado Outbreak (AVESESAME I). MWR, 110, 2005-2024.

Fujita, T. T., 1980: In search of mesoscale wind fields in landfalling hurricanes. Presented at the 13th Am. Meteorol. Soc. Conference on Hurricanes and Tropical Meteorology. Miami Beach, Florida, December 1-5, 1980.

Gannon, P. T., Sr., 1978: Influence of earth surface and cloud properties on the South Florida sea breeze. NOAA Tech. Tep. ERL 402-NHEML-2.

Green, J. S. A. and G. A. Dalu, 1980: Mesoscale energy generated in the boundary layer. Quart. J. R. Met. Soc., 106, 721-726.

Gross, G., 1986: A numerical study of the land and sea breeze including cloud formation. Beitr. Phys. Atmosph., Vol. 59, No. 1, pp. 97-113.

Hack, J. J., and W. H. Schubert, 1976: Design of an axisymmetric primitive equation tropical cyclone model. Atmospheric Science Paper, #263, Colorado State University, Fort Collins, CO, 70 pp.

Houze, R. A., Jr., and Betts, A. K., 1981: Convection in GATE. Rev. of Geophys. and Space Phys., 19, 541-576.

Hoxit, L. R., C. F. Chappell and J. M. Fritsch, 1976: Formation of mesolows or pressure troughs in advance of cumulonimbus clouds. Mon. Wea. Rev., 104, 1419-1428.

Johnson, R. H., 1976: The role of convective-scale precipitation downdrafts in cumulus and synoptic-scale interactions. J. Atmos. Sci., 33, 1890-1910.

Johnson, R. H., 1981: Large-scale effects of deep convection on the GATE tropical boundary layer. JAS, 38, 2399-2413.

Johnson, R. H. and D. C. Kriete, 1982: Thermodynamic and circulation characteristics of winter monsoon typical mesoscale convection. Mon. Wea. Rev., 110, 1898-1911.

Keyser, D. A., and D. R. Johnson, 1982: Effects of diabatic heating on the ageostrophic circulation of an upper tropospheric jet streak. NASA Contractor Report 3497. NASA Marshall Space Flight Center, 121 pp.

Klemp, J. B., and R. B. Wilhelmson, 1978: The simulation of three-dimensional convective storm dynamics. JAS, 35, 1070-1076.

Knupp, K. R., 1985: Precipitating convective cloud downdraft structure: A synthesis of observations and modeling. Ph.D. dissertation, Dept. of Atmospheric Science, Colorado State University, Fort Collins, Colorado.

Kreitzberg, C. W., and D. J. Perkey, 1976: Release of potential instability. Part I. A sequential plume model within a hydrostatic primitive equation model. JAS, 33, 456-475.

Kung, E. C., and W. E. Baker, 1975: Energy transformation in middle latitude disturbances. Quart. J. R. Met. Soc., 101, 793-815.

Kung, E. C., and T. L. Tsui, 1975: Subsynoptic-scale kinetic energy balance in the storm area. J. Atmos. Sci., 32, 729-740.

Kuo, H. L., 1965: On formation and intensification of tropical cyclones through latent heat release by cumulus convection. J., Atmos. Sci., 22, 40-63.

Kuo, H. L., 1974: Further studies of the parameterization of the influence of cumulus convection on large-scale flow. J. Atmos. Sci., 31, 1232-1240.

Kuo, H. L. and W. H. Raymond, 1980: A quasi-one-dimensional cumulus cloud model and parameretization of cumulus heating and mixing effects. Mon. Wea. Rev., 108, 991-1009.

Leary, C. A., and R. A. Houze, Jr., 1979: The structure and evolution of convection in a tropical cloud cluster. J. Atmos. Sci., 36, 437-457.

Lopez, P. E., D. O. Blanchard, R. Daniel, W. L. Hiscox, and M. J. Casey, 1984a: Population characteristics, development processes and structure of radar echoes in south Florida. Mon. Wea. Rev., 112, 56-75.

Lopez, P. E., P. T. Gannon, D. O. Blanchard, and C. C. Balch, 1984b: Synoptic and regional circulation parameters associated with the degree of convective shower activity in south Florida. Mon. Wea. Rev., 112, 686-703.

Maddox, R. A., 1980: Mesoscale Convective Complexes. Bull. Am. Met. Soc., 61, 1374-1387.

Mahrer, Y., and R. A. Pielke, 1976: Numerical simulation of the air flow over Barbados. MWR, 104, 1392-1402.

Mahrer, Y., and R. A. Pielke, 1977: A numerical study of the air flow over irregular terrain. Contrib. Atmos. Phys., 50, 98-113.

Mahrer, Y., and R. A. Pielke, 1978: A test of an upstream spline interpolation technique for the advective terms in a numerical mesoscale model. MWR, 106, 1758.

McCumber, M. C. and R. A. Pielke, 1981: Simulation of the effects of surface fluxes of heat and moisture in a mesoscale numerical model, 1. Soil layer. J. of Geophy. Res., Vol. 86, 9929-9938.

McInnis, D. H., and E. C. Kung, 1972: A study of subsynoptic-scale energy transformation. Mon. Wea. Rev., 100, 126-132.

McQueen, J. T., 1984: The study and forecast of sea breeze induced mesoscale systems by combining the results of a mesoscale numerical model with climatology. M.S. thesis, Dept. of Atmospheric Science, Colorado State University, June.

McQueen, J. T., and R. A. Pielke, 1985: A numerical and climatological investigation of deep convective cloud patterns in south Florida. Atmos. Sci. Paper #389, Department of Atmospheric Science, Colorado State University, Fort Collins, Colorado 80523. 177 pp.

Michaels, P. J., R. A. Pielke, J. T. McQueen, and D. E. Sappington, 1986: Composite climatology of Florida summer thunderstorms: 1. Descriptive and statistical analyses. Mon. Wea. Rev. (submitted).

Miller, M. J., and R. P. Pearce, 1974: A three-dimensional primitive equation model of cumulonimbus convection. Quart. J. R. Met. Soc., 100, 133-154.

Molinari, J., and T. Corsetti, 1985: Incorporation of cloud-scale and mesoscale downdrafts into a cumulus parameterization: Results of one- and three-dimensional integrations. Mon. Wea. Rev., 113, 485-501.

O'Brien, J. J., 1970: A note on the vertical structure of the eddy exchange coefficient in the planetary boundary layer. JAS, 27, 1213-1215.

Ogura, Y., and M. T. Liou, 1980: The structure of a mid-latitude squall line: A case study. J. of Atmos. Sci., Vol. 37, 553-567.

Ogura, Y., Y.L. Chen, J. Russell and S. T. Soong, 1979: On the formation of organized convective systems observed over the eastern Atlantic. Mon. Wea. Rev., 107, 426-441.

Orlanski, I., and B. B. Ross, 1984: The evolution of an observed cold front. Part II: Mesoscale dynamics. J. Atmos. Sci., 41, 1669-1703.

Paegle, J., W. G. Zdunkowski, and R. M. Welch, 1976: Implicit differencing of predictive equations of the boundary layer. MWR, 104, 1321-1324.

Pearson, R. A., 1975: On the asymmetry of the land-breeze sea-breeze circulation. Quart. J. R. Met. Soc., 101, 529-536.

Pepper, D. W., C. D. Keen, and Long, P. E., Jr., 1979: Modeling the dispersion of atmospheric pollution using cubic splines and chapeau functions. Atm. Environ., 13, 223-237.

Perkey, D. J., and R. A. Maddox, 1985: A numerical investigation of a mesoscale convective system. Mon. Wea. Rev., 113, 553-566.

Pielke, R. A., 1974: A three-dimensional numerical model of the sea breeze over South Florida. MWR, 102, 115-139.

Pielke, R. A., 1984: Mesoscale Meteorological Modeling. Academic Press (in press).

Pielke, R. A., and W. R. Cotton, 1977: A mesoscale analysis over south Florida for a high rainfall event. MWR, 105, 343-362.

Pielke, R. A., and Y. Mahrer, 1975: Techniques to represent the heated planetary boundary layer in mesoscale models with coarse vertical resolution. JAS, 32, 2288-2308.

Pielke, R. A., and Y. Mahrer, 1978: Verification analysis of the University of Virginia three-dimensional mesoscale model prediction over South Florida for July 1, 1973. MWR, 106, 1568-1569.

Purnell, D. K., 1976: Solution of the advective equation by upstream interpolation with a cubic spline. MWR, 104, 42-48.

Raymond, D. J., 1984: A wave-CISK model of squall line. J. Atm. Sci., 41, 1946-1958.

Reap, R. M., and D. S. Foster, 1979: Automated 12-36 hour probability forecasts of thunderstorms and severe local storms. J. Appl. Meteor., 18, 1304-1315.

Richiardone, R. and R. A. Pearson, 1983: Inland convection and energy transfers in a sea breeze model. Quart. J. R. Met. Soc., 104, 325-338.

Robertson, F. R., and P. J. Smith, 1980: The kinetic energy budgets of two severe storm producing extratropical cyclones. Mon. Wea. Rev., 108, 127-143.

Schlesinger, R. E., 1978: A three-dimensional numerical model of an isolated thunderstorm: Part I. Comparative experiments for variable ambient wind shear. JAS, 35, 690-713.

Schlesinger, R. E., 1980: A three-dimensional numerical model of an isolated thunderstorm. Part II: Dynamics of updraft splitting and mesovortex couplet evolution. J. Atmos. Sci., 37, 395-420.

Schlesinger, R. E., 1984: Effects of the pressure perturbation field in numerical models of unidirectionally sheared thunderstorm convection: two versus three dimensions. J. Atmos. Sci., 41, 1571-1587.

Simpson, J., 1980: Downdrafts as linkages in dynamic cumulus seeding effects. JAM, 19, 477-487.

Simpson, J., G. Van Helvoirt, and M. McCumber, 1982: Three-dimensional simulation of cumulus congestus clouds on GATE day 261. JAS, 39, 126-145.

Simpson, J., and V. Wiggert, 1969: Models of precipitating cumulus towers. Mon. Wea. Rev., 97, 471-489.

Smith, P. J., 1980: The energetics of extratropical cyclones. Rev. Geophys. Space Phys., 18, 378-386.

Smith, P. J. and L. H. Horn, 1969: A computational study of the energetics of a limited region of the atmosphere. Tellus, 21(2), 193-201.

Smith, P. J., D. G. Vincent, and H. J. Edmon, Jr., 1977: The time dependence of reference pressure in limited region available potential energy budget equations. Tellus, 29, 476-480.

Smull, B. F. and R. Houze, 1986: Dual-Doppler radar analysis of a mid-latitude squall line with a trailing region of stratiform rain. Submitted to J. of Atmos. Sci.

Song, J. L., and W. M. Frank, 1983: Relationships between deep convection and large-scale processes during GATE. MWR, 111, 2145-2160.

Song, J. L., R. A. Pielke, and M. Segal, 1985: Vectorizing a mesoscale meteorological model on the CYBER 205. Environmental Software, Jan. 1986.

Tao, W. K., and J. Simpson, 1984: Cloud interactions and merging: Numerical simulations. J. Atmos. Sci., 41, 2901-2917.

Thorpe, A. J., M. J. Miller, and M. W. Moncreiff, 1979: Dynamical models of two-dimensional downdrafts. Quart. J. Roy. Meteor. Soc., 196, 463-484.

Tripoli, G. J., and W. R. Cotton, 1980: A numerical investigation of several factors contributing to the observed variable intensity of deep convection over South Florida. JAM, 19, 1037-1063.

Tripoli, G. J., and W. R. Cotton, 1982: The Colorado State University three-dimensional cloud/mesoscale model - 1982. Part I: General theoretical framework and sensitivity experiments. J. de Rech. Atmos., 16, 185-200.

Tsui, T. L., and E. C. Kung, 1977: Subsynoptic-scale energy transformation in various severe storm situations. J. Atmos. Sci., 34, 98-110.

Ulanski, S. L., and M. Garstang, 1978: The role of surface divergence and vorticity in the lifecycle of convective rainfall, Part I: Observation and analysis. JAS, 35, 1047-1062.

Van De Berg, L. C. and J. Oerlemans, 1985: Simulation of the sea-breeze front with a model of moist convection. Tellus (1985), 37A, 30-40.

Vincent, D. G., and L. N. Chang, 1975: Kinetic energy budgets of moving system case studies for an extra-tropical cyclone and hurricane Celia, 1970. Tellus, 27, 215-233.

Vincent, D. G., and T. W. Schlatter, 1979: Evidence of deep convection as a source of synoptic-scale kinetic energy. Tellus, 31, 493-504.

Ward, J. H., and P. J. Smith, 1976: A kinetic energy budget over North America during a period of short synoptic wave development. MWR, 104, 836-848.

Weisman, M. L., and J. B. Klemp, 1984: The structure and classification of numerically simulated convective storms in directionally varying wind shears. Mon. Wea. Rev., 112, 2479-2498.

Woodley, W. L., J. A. Jordan, J. S. Simpson, R. Biondini, J. A. Flueck, and A. G. Barnes, 1982: Rainfall results of the Florida Area Cumulus Experiment. JAM, 21, 139-164.

Zhang, D. L., 1985: Nested-grid simulation of the meso-β scale structure and evolution of the Johnstown flood of July 1977. Ph.D. dissertation, The Pennsylvania State University, 270 pp.

Zipser, E. J., 1969: The role of organized unsaturated downdrafts in the structure and decay of an equatorial disturbance. JAM, 8, 799-814.

Zipser, E. J., 1977: Mesoscale and convective scale downdrafts as distinct components of squall line structure. MWR, 105, 1568-1589.

## APPENDIX A

### (A) BOUNDARY LAYER

The vertical exchange coefficients in the surface layer are given by

$$K_z^m(z^*) = k_o u_* z^*/\phi_m(\xi)$$
$$K_z^\theta(z^*) = K_z^q(z^*) = k_o u_* z^*/\phi_H(\xi)$$

where $\xi = z^*/L_*$, with $L_* = \dfrac{\theta\, U_*^2}{k_o g \theta_*}$ .

The expression for the nondimensional wind and potential temperature profiles according to Businger (1973) are given below

$$\phi_m = \begin{cases} (1 - 15\xi)^{-1/4}, & \xi \leq 0. \\ 1 + 4.7\xi, & \xi > 0. \end{cases}$$

$$\phi_H = \begin{cases} .74(1 - 9\xi)^{-1/2}, & \xi \leq 0 \\ .74 + 4.7\xi, & \xi > 0 \end{cases}$$

where $\phi_m = \dfrac{k_o z^*}{u_*} \dfrac{\partial u}{\partial z^*}$ and $\phi_H = \dfrac{k_o z^*}{\theta_*} \dfrac{\partial \theta}{\partial z^*}$ .

The integrated version of the profiles are given by

$$u_* = k_o(u^2 + v^2)^{1/2}/(\ln(z/z_o) - \psi_1),$$

$$\theta_* = k_o(\theta - \theta(z_o))/(.74(\ln(z/z_o) - \psi_2)).$$

$$q_* = k_o(q - g(z_o))/(.74(\ln z/z_o) - \psi_2))$$

with $\psi_1 = \begin{cases} 2\ln[(1 + \phi_m^{-1})/2] + \ln[(1 + \phi_m^{-2})/2] - 2\tan^{-1}\phi_m^{-1} + \pi/2 & \xi \leq 0 \\ -4.7\xi & \xi > 0 \end{cases}$

$$\text{and} \quad \psi_2 = \begin{cases} 2\ln[(1 + .74\,\phi_H^{-1})/2] & \xi \leqq 0 \\ -6.35\,\xi & \xi > 0 \end{cases}$$

The functional form of the exchange coefficient above the surface layer suggested by O'Brien (1970) is:

$$K_z(z^*) = \begin{cases} K_z\Big|_{z_i} + (z_i - z^*)^2/(z_i - h)^2 \{K_z\Big|_h - K_z\Big|_{z_i} + (z^* - h)[\frac{\partial}{\partial z^*} K_z\Big|_h + 2((K_z\Big|_h - K_z\Big|_{z_i})/(z_i - h))]\} & z_i \geqq z^* \geqq h \\ K_z\Big|_{z_i} & z^* > z_i \\ (z^*/h)K_z\Big|_h & z^* < h \end{cases}$$

where $K_z(z^*)$ refers to $K_z^m(z^*)$, $K_z^q(z^*)$ and $K_z^\theta(z^*)$, $K_z\Big|_{z_i} = 1\ \text{cm}^2\ \text{sec}^{-1}$; and $K_z\Big|_h$ is the exchange coefficient at the top of the surface layer, h, which is defined as

$$h = z_i/25.$$

The depth of the planetary boundary layer, $z_i$, is predicted by a prognostic equation based on Deardoff's (1974) work. Its form is

$$\frac{\partial z_i}{\partial t} + u\frac{\partial z_i}{\partial x} + v\frac{\partial z_i}{\partial y} = w_i^* + \frac{1.8(W_*^3 + 1.1\,u_*^3 - 3.3\,u_*^2\,f\,z_i)}{g\frac{z_1^2}{\theta}\frac{\partial\theta^+}{\partial z^*} + 9\,W_*^2 + 7.2\,u_*^2} \qquad (1)$$

with the value of $W_*$ given as

$$W_* = \begin{cases} ((-g/\theta)u_*\theta_* z_i)^{1/3} & \theta_* \leqq 0 \\ 0 & \theta_* > 0. \end{cases}$$

Over the land surface a roughness length of $z_o = 4$ cm is used, while over water $z_o$ is defined according to Clarke (1970) as

$$z_o = 0.032\,u_*^2/g$$

with the condition that

$$z_o \geqq 0.0015 \text{ cm.}$$

(B) SURFACE ENERGY BALANCE

The land surface temperature is computed by a Newton-Raphson iteration solution to the heat balance equation

$$R_S + R_L + \rho L u_* q_* + \rho c_p u_* \theta_* - \rho_s c_s K_s \frac{\partial T}{\partial z}_G - \sigma T_G^4 = 0 \qquad (2)$$

where

$R_S$ is the incoming solar radiation,

$R_L$ is the incoming long wave radiation.

The third, fourth and fith terms are the latent, sensible and soil heat fluxes, respectively. The sixth term is the outgoing long wave radiation from the surface. We will describe here, as briefly as possible, the various steps of the solution to equation (2). Let $F(T_G)$ be equal to the sum of the terms on the left side of (2) (in practice usually $F(T_G) \neq 0$). If $F(T_G)$ is not less than $\varepsilon$ (we have chosen $\varepsilon = 10^{-5}$) we apply the Newton-Raphson iteration process in the form

$$T_G^{m+1} = T_G^m - F(T_G)/F'(T_G).$$

Here $F'(T_G)$ is the derivative of $F(T_G)$ with respect to $T_G$ with the assumption that $u_*$, $q_*$, $\psi_1$ and $\psi_{2y}$ are constants. $\theta_*$ is written in the following way,

$$\theta_* = k_o(\theta(1) - T_G(\frac{P_{oo}}{P_G})^{R/c_p})/[.74(\ln z/z_o - \psi_2) + .0962(\frac{u_* z_o}{\nu})^{.45}] .$$

The right term in the denominator is added to Businger's (1973) surface layer equation since his formulas require temperature and specify

humidity at $z_o$ rather than at the surface. The expression for $\theta(z_o)$ and $q(z_o)$ as a function of $u_*$ and $\theta_*$, based on Zilitinkevich (1970) are

$$\theta(z_o) = \theta_G + .0962 \frac{\theta_*}{k_o} \left(\frac{u_* z_o}{\nu}\right)^{.45}$$

and

$$q(z_o) = q_G + .0962 \frac{q_*}{k_o} \left(\frac{u_* z_o}{\nu}\right)^{.45}$$

so that for $F'(T_G)$ we have

$$F'(T_G) = \left(\rho c_p u_* k_o / \left[.74(\ln z/z_o - \psi_2) + .0962 \left(\frac{u_* z_o}{\nu}\right)^{.45}\right]\right) \times \left(\frac{P_{oo}}{P_G}\right)^{R/c_p} - \frac{\rho_s c_s K_s}{\Delta z_G} - 4 \sigma T_G^3 .$$

After the desired accuracy of $F(T_G)$ has been reached we stop the iteration and check the absolute change in $\theta_*$. In the case where the absolute change in $\theta_*$ is greater than 0.01 we recalculate the boundary layer equation with the new values of $T_G$ and $q_G$ and repeat the above procedure.

The short and long-wave radiation parameterizations in the model were adapted from the work of Jacobs, Pandolfo and Atwater (1974), and are described below.

(C) SHORTWAVE RADIATION

The diurnal variation of the solar flux on a horizontal surface at the top of the atmosphere is computed from

$$S = S_o \cos Z$$

with

$$\cos Z = \sin\phi \sin\delta + \cos\phi \cos\delta \cos\psi$$

where $\phi$ is the latitude, $\delta$ is the solar declination and $\psi$ is the solar hour angle. At the surface the solar radiation is obtained by using two empirical functions. The first empirical transmission

function includes molecular scattering and absorption by permanent gases such as oxygen, ozone, and carbon dioxide. This function, originally presented by Kondrat'yev (1969) and modified by Atwater and Brown (1974) to account for the forward Rayleigh scattering is given by

$$G = .485 + .515\ [1.041 - .16\ (\frac{.000949p + .051}{\cos Z})^{1/2}]$$

where $p$ is pressure in mb.

The second empirical function is from McDonald (1960) and accounts for the absorptivity of water vapor

$$a_w = .077\ [\frac{r(z)}{\cos Z}]^{.3}$$

where $r$ is the optical path length of water vapor above the layer z. It is given as

$$r(z) = \int_z^{top} \rho\, q\, dz.$$

The net short wave radiative flux at the surface is

$$R_S = \begin{cases} S_o \cos Z(1 - A)(G - a_w) & \cos Z > 0 \\ 0 & \cos Z \leqq 0 \end{cases}$$

Where $A$ is the albedo.

The solar radiative heating rates are computed for the absorption of short wave energy by the water vapor only and are given by

$$(\frac{\partial T}{\partial t})_s = .0231\ \frac{S_o \cos Z}{\rho c_p}\ [\frac{r(z)}{\cos Z}]^{-0.7}\ \frac{dr}{dz}\ .$$

(D) LONGWAVE RADIATION

Longwave radiation and atmospheric heating due to its flux divergence are calculated for each time step. Considered as emitters of log wave radiation are carbon dioxide and water vapor. The path

length for water vapor ($\Delta r_j$) is computed for each layer from the surface to the top of the model by

$$\Delta r_j = - \frac{(P_{j+1} - P_j)}{g} q_j .$$

The path length for $CO_2$($\Delta c_j$) is

$$\Delta c_j = - .4148239 \ (p_{j+1} - p_j).$$

After these increments are obtained they are summed up from the first level to the ith level to give the total path length, given as

$$r_i = \sum_{j=1}^{i} \Delta r_j, \qquad c_i = \sum_{j=1}^{i} \Delta c_j.$$

The emissivity for water vapor was derived from data of Kuhn (1963) and are given in Jacobs, et al. (1974).

$$\varepsilon_r(ij) = \begin{cases} 0.11288 \log_{10}(1 + 12.68 \bar{r}) & \text{for } \log_{10} \bar{r} < -4 \\ 0.104 \log_{10} \bar{r} + 0.440 & \text{for } \log_{10} \bar{r} < -3 \\ 0.121 \log_{10} \bar{r} + 0.491 & \text{for } \log_{10} \bar{r} < -1.5 \\ 0.146 \log_{10} \bar{r} + 0.527 & \text{for } \log_{10} \bar{r} < -1 \\ 0.161 \log_{10} \bar{r} + 0.542 & \text{for } \log_{10} \bar{r} < 0 \\ 0.136 \log_{10} \bar{r} + 0.542 & \text{for } \log_{10} \bar{r} > 0 \end{cases}$$

where $\bar{r} = |r_i - r_j|$ is the optical path length between the ith and jth levels.

Kondrat'yev's (1969) emissivity function for carbon dioxide in the form

$$\varepsilon_{co2}(i,j) = .185[1 - \exp(- .3919 \ |c_i - c_j|^{0.4})]$$

is used, and finally the emissivity at each level is given by

$$\varepsilon(i,j) = \varepsilon_r(i,j) + \varepsilon_{co2}(i,j).$$

Using the above emissivity functions we have for the downward and upward fluxes at a level N

$$R_d(N) = \sum_{j=N}^{top-1} \frac{\sigma}{2} (T_{j+1}^4 + T_j^4)[\varepsilon(N,j+1) - \varepsilon(N,j)]$$

$$+ \sigma T_{top}^4 (1 - \varepsilon(n,top))$$

and

$$R_u(N) = \sum_{j=1}^{N-1} \frac{\sigma}{2} (T_{j+1}^4 + T_j^4)[\varepsilon(N,j) - \varepsilon(n,j+1)]$$

$$+ \sigma T_G^4(1 - \varepsilon(N,0)).$$

The radiative cooling at each layer is computed from

$$\left(\frac{\partial T}{\partial t}\right)_N = \frac{1}{\rho c_p} \frac{(R_u(N+1) - R_u(N) + R_d(N) - R_d(N+1))}{z(N+1) - z(N)} .$$

Since the above procedure consumes a large amount of computation time we adopted Sasamori's (1972) technique which assumes that the whole atmosphere has a temperature of the level at which flux divergence is calculated. In this way the radiative cooling is approximated by:

$$\left(\frac{\partial T}{\partial t}\right)_N = \frac{1}{\rho c_p (z(N+1) - z(N)} [(\sigma T_N^4 - \sigma T_G^4)(\varepsilon(N+1,0) - \varepsilon(N,0))$$

$$+ (\sigma T_{top}^4 - \sigma T_N^4)(\varepsilon(N+1,top) - \varepsilon(N,top))$$

(E) SURFACE LAYER VERTICAL ADVECTION

Whenever the vertical velocity at the first layer is positive we evaluate the vertical derivatives of temperature, humidity and velocities from surface layer similarity theory. The corrected advection terms are given by:

$$w_i^* \frac{\partial u}{\partial z^*} = w_i^* \frac{u_* |_x \phi_m}{k_o z^*}, \quad w_i^* \frac{\partial v}{\partial z^*} = w_i^* \frac{u_* |_y \phi_m}{k_o z^*}$$

$$w_i^* \frac{\partial \theta}{\partial z^*} = w_i^* \frac{\theta_* \phi_H}{k_o z^*}, \quad w_i^* \frac{\partial q}{\partial z^*} = w_i^* \frac{q_* \phi_H}{k_o z^*} \; .$$

This technique will result in a better estimate of the vertical advection terms near the ground since the standard finite difference assumes that a linear gradient exists there.

## APPENDIX B

## PROCEDURES OF THE CONVECTIVE PARAMETERIZATION

The step-by-step computational procedures of evaluating the convective updraft, downdraft, and grid-environmental effects are briefly described in this Appendix. When coupled with the modifications made to the Fritsch-Chappell scheme (as illustrated in Chapter 3), the mathematical expressions included in Fritsch and Chappell (1980) can be directly applied to the current scheme. Therefore, the equations for the individual computational steps are not included in the current study. All the convective quantities are evaluated at vertical grids with a constant interval of about 700 m. The lowest level is the lowest model level (i.e., 9 m), while the highest level is at the model top (20 km). Thus the total number of vertical levels in the parameterization is 30. Interpolations are performed between the model and the parameterization (linear interpolation is used).

### B-1. Updraft Calculation

The computational steps of updraft effects are:

(1) Determine updraft source air as the mixture of the most unstable layer air within the lowest 2 km. This layer is 500 m-1000 m thick.

(2) Determine cloud base by the lifting condensation level following the formulation of Bolton (1980).

(3) Check if deep convection occur (as shown in the Steps (1)-(3) in Fig. 3-2). The parameterization proceeds only when the conditions are satisfied.

(4) Determine updraft massflux profile. The maximum updraft massflux is located at the height of the maximum temperature-excess term (for an undilute ascent of the source air). The initial updraft massflux at cloud base is determined by the grid-scale massflux. The vertical profile of massflux is determined by specifying the entrainment rate. As in Fritsch and Chappell (1980), the updraft massflux is assumed to double its magnitude from cloud base to its maximum level.

(5) Updraft velocity is calculated by using the buoyancy equation with a constant parameter (0.5) which simulates the compensating effect of neglecting nonhydrostatic pressure (Kreitzberg and Perkey, 1976).

(6) Updraft thermodynamic quantities are obtained by considering entrainment mixing (as done in Fritsch and Chappell, 1980). Condensate is produced assuming the updraft is always saturated with respect to liquid. Extra heating is added when freezing occurs.

(7) Updraft area is determined by considering its massflux, velocity, and density (in which density is diagnosed from temperature and the ambient pressure using the ideal gas law).

(8) Total rainfall is determined by multiplying the total moisture supply (i.e., the total moisture flux at cloud base) by a precipitation efficiency. A value of 70 percent is used

for the Florida summertime deep convection investigated in this study.

(9) The freezing process of the updraft includes two parts. A specified fraction (FRACI) of the total accumulated liquid condensate produced below the -5°C level is assumed to freeze, up to the -20°C level (uniformly in the vertical). The "in situ" produced condensate above the -5°C level is assumed to contain ice by percentages from 0 percent (at the -5°C level) to 100 percent (at the -20°C level).

B-2. Downdraft Calculation

(1) Downdraft is initiated at the level of minimum environmental equilibrium potential temperature (see a detailed discussion of convective downdrafts in Knupp, 1985). The initial downdraft massflux is assumed to be 50 percent of the initial updraft massflux at cloud base.

(2) The entrainment rate for the downdraft is the same as that for updraft. Accordingly, the downdraft massflux, vertical velocity, and area are determined in the same way as for updraft.

(3) Entrainment mixing of the downdraft includes updraft and environmental properties for the cloud-layer, while only the environmental properties are used in the subcloud layer. The condensate consumption is calculated based on the entrainment mixing and a specified downdraft relative humidity (90 percent is used for the Florida moist sea breeze simulation).

(4) The ice produced by updraft is assumed to primarily melt in the lower troposphere by the downdraft. A melting layer of

not thicker than 2 km is assumed to be immediately beneath the 0°C level. A small portion of the total ice (about 10 percent, as in Fritsch and Chappell, 1980) is assumed to go into anvil cloud and evaporate.

B-3. Grid-Environment Calculation

The grid-environment is the space of the model grid volume excluding the updraft and the downdraft. Processes occurring in the grid-environment include detrainment, anvil evaporation, subsidence, and surface-layer stabilization. The computational steps are:

(1) Updraft detrainment is determined by the massflux divergence between the maximum-massflux level and cloud top (the cloud top is defined as where updraft velocity becomes zero). Detrained air from the updraft mixes with the environmental air at the same heights.

(2) Detrained condensate from the updraft is assumed to evaporate, thereby producing cooling and moistening in the anvil layer (the anvil layer is defined as the layer where updraft experiences horizontal mass divergence).

(3) The grid-environmental vertical motion is determined by the compensating motion associated with the net massflux in the grid volume (Fritsch and Chappell, 1980). Adiabatic warming due to compensating downward motion is accounted for in the grid-environment.

(4) Above the temperature equilibrium level, nonzero updraft velocity produces overshooting, resulting in colder air for the upper levels of the grid element.

(5) Near the surface, the downdraft replaces the unmodified air, thereby stabilizing the surface layer. The fractional area in which surface air is assumed to be completely replaced by downdraft air is determined by the relative contribution of downdraft massflux entering subcloud layer (That is, the ratio of downdraft massflux at cloud base to the sum of the downdraft massflux and grid-scale massflux in the subcloud layer determines the fraction of grid area in which subcloud air is replaced by the downdraft air.)

# APPENDIX C

## DOMAIN-INTEGRATED KINETIC ENERGY BUDGET COMPONENTS OF THE MOIST SEA BREEZE SIMULATION

The domain-integrated kinetic energy budget components (introduced in Chapter 2) for the moist sea breeze simulation (i.e., the control run, as introduced in Chapter 4) are calculated and listed in Table C-1. The unit for all the quantities is watt/$m^2$. As discussed in Chapter 3, deep cumulus convective effects are incorporated into the mesoscale prognostic model through the convective heating and moistening terms. Therefore, the changes on the mesoscale horizontal velocities and kinetic energy are created primarily through the cross-contour term (or the pressure gradient term, which is discussed in Chapter 6).

Theoretically, the domain-integrated model kinetic energy tendency obtained from summing up the budget components must equal that obtained by directly calculating the kinetic energy tendency using model's horizontal velocity components. Anthes and Warner (1978) indicated that such a comparison provides a method to examine the model coding. From Table C-1 we see that these two terms, denoted as $\delta K/\delta t$ (Budget) and $\delta K/\delta t$ (model), respectively, are nearly identical to each other for up to 3 digital points even during late afternoon when deep convective effects are typically significant. As shown in Table C-1, the budget components include the cross-contour term, turbulence term, horizontal net flux term and the filter term (introduced in Chapter 2).

## APPENDIX C

### DOMAIN-INTEGRATED KINETIC ENERGY BUDGET COMPONENTS OF THE MOIST SEA BREEZE SIMULATION

| Model Time (sec) from 6 AM | Local Time | $\frac{\delta K}{\delta t}$ Model | $\frac{\delta K}{\delta t}$ Budget | Cross-Contour Term | Turbulence Term | Horizontal Net Flux Term | Filter Term |
|---|---|---|---|---|---|---|---|
| 3600. | ~7 AM | -.1350E-02 | -.1334E-02 | .1848E-01 | -.2130E-01 | .1572E-02 | -.8192E-04 |
| 7200. | 8 AM | -.6295E-01 | -.6294E-01 | .2317E-03 | -.3205E-01 | -.3061E-01 | -.3090E-03 |
| 10800. | 9 AM | -.7450E-01 | -.7449E-01 | .8778E-02 | -.4227E-01 | -.4026E-01 | -.7458E-03 |
| 14400. | 10 AM | -.9853E-02 | -.9825E-02 | .6691E-01 | -.6111E-01 | -.1306E-01 | -.2542E-02 |
| 18000. | 11 AM | .3597E-01 | .3602E-01 | .1212E+00 | -.6612E-01 | .1134E-01 | -.1035E-01 |
| 21600. | 12 | .9877E-01 | .9886E-01 | .1704E+00 | -.1006E+00 | .5479E-01 | -.2574E-01 |
| 25200. | 1 PM | -.1661E+00 | -.1659E+00 | .8055E-01 | -.1250E+00 | -.6469E-01 | -.5678E-01 |
| 28800. | 2 PM | -.3517E-01 | -.3502E-01 | .2792E+00 | -.1514E+00 | -.5912E-01 | -.1037E+00 |
| 30600. | | .3249E+00 | .3252E+00 | .5927E+00 | -.1594E+00 | .2756E-01 | -.1357E+00 |
| 32400. | 3 PM | .8291E+00 | .8296E+00 | .1005E+01 | -.1636E+00 | .1550E+00 | -.1669E+00 |
| 34200. | | .5576E+00 | .5586E+00 | .9525E+00 | -.1512E+00 | -.4899E-01 | -.1938E+00 |
| 36000. | 4 PM | .1140E+01 | .1141E+01 | .1322E+01 | -.1396E+00 | .1932E+00 | -.2340E+00 |